



This is to certify that the
thesis entitled
Multipole Moments of ^{232}Th , ^{234}U , ^{236}U , ^{238}U
Using Proton Inelastic Scattering

presented by

Robert Clare Melin

has been accepted towards fulfillment
of the requirements for

Ph.D. degree in Physics


Major professor

Date 6 April 1981



OVERDUE FINES:
25¢ per day per item

RETURNING LIBRARY MATERIALS:
Place in book return to remove
charge from circulation records

MULTIPOLE MOMENTS OF ^{232}Th , $^{234,236,238}\text{U}$
USING PROTON INELASTIC SCATTERING

By

Robert Clare Melin

A DISSERTATION

Submitted to

Michigan State University

in partial fulfillment of the requirements

for the degree of

DOCTOR OF PHILOSOPHY

Department of Physics

1981

ABSTRACT

MULTIPOLE MOMENTS OF ^{232}Th , $^{234,236,238}\text{U}$
USING PROTON INELASTIC SCATTERING

By

Robert Clare Melin

The multipole moments of ^{232}Th , $^{234,236,238}\text{U}$ have been determined using proton scattering at 35.3 MeV. The angular distributions of scattered protons for the elastic ($J^\pi = 0^+$) and ground state rotational band states ($J^\pi = 2^+, 4^+, 6^+, 8^+$) were extracted for laboratory angles from 20 to 144.5 degrees. The targets were UF_4 and ThF_4 and isotopically separated for $^{234,236}\text{U}$. The scattered protons were detected using a position sensitive detector in the focal plane of an Enge split-pole spectrograph. The typical energy resolution of 15 keV is made possible by using dispersion matching for the entire range of scattering angles.

The data were analyzed using coupled channels calculations for scattering from a rigid rotor via a deformed optical model potential. Automatic searches were made on

6/1/58

a number of model parameters, including the deformation parameters β_2 , β_4 , β_6 for both spherical and deformed spin-orbit potentials. The quadrupole hexadecapole and hexakontatetarapole moments were calculated from the parameter values and compared with the results of Coulomb excitation, electron scattering, inelastic alpha scattering and with predictions of microscopic calculations. Improved fits to the data were obtained by including the higher order deformations. Comparisons were made for a full deformed spin-orbit potential and a spherical spin-orbit potential, with the deformed spin-orbit yielding improved fits. The resultant quadrupole moments increase in magnitude with increasing nuclear mass in agreement with Coulomb excitation results but systematically 3% to 5% lower. The present results are 3% to 6% higher than those predicted by microscopic calculations. The hexadecapole moment from this study is largest for $A = 234$ in agreement with the trend predicted by the microscopic calculations and from the Coulomb excitation results, although the magnitudes of the latter exceed the present results by as much as 25%.

In general, the quadrupole and hexadecapole moments deduced in this work disagree in trend and magnitude with the inelastic alpha scattering results. The hexakontatetarapole moments of these nuclei are extracted for the first time and reach a maximum for $A = 236$ and approach zero for $A = 238$, a trend which can be explained by a

simple model which also predicts the quadrupole and hexadecapole behavior.

ACKNOWLEDGMENTS

During my years at Michigan State University I received assistance from many friends and colleagues. My thanks go out to all of them with special acknowledgments to the following.

To Dr. J. A. Nolen, Jr. who advised me and assisted in choosing and completing this project. By working with Jerry, I gained an immeasurable wealth of knowledge about experimental methods, techniques and equipment.

To Drs. R. G. Markham and R. G. H. Robertson with whom I worked throughout my graduate career. Roger taught me much of what I know about particle detectors as we designed and developed new detectors. The experiments I worked on with Hamish provided exciting challenges and an excellent opportunity to broaden my education.

Without the timely guidance of Dr. R. M. Ronningen this project would have been difficult. Reg was extremely helpful in understanding and completing the calculations leading to the experimental results. For his assistance in writing this thesis, for his constructive comments on presentations of this work, and for his friendship, I am forever indebted.

To the National Science Foundation which supplied operating funds to the Cyclotron Laboratory and to Dr. H. Blosser, the staff and faculty of the Cyclotron Laboratory,

for making it an excellent facility in which to work and learn. A special thanks to Peter Miller, Jones Chein, Harold Hilbert, Dan Magistro, Bill Harder and their helpers who maintained and kept the cyclotron and experimental equipment running and to Dick Au and Tim Glynn who worked diligently to keep the computer running.

To Mr. Norval Mercer and his machine shop crew who fabricated much of the experimental equipment I used. Besides teaching me the art of working in the machine shop and giving guidance on my mechanical projects, Merce is a good friend with whom I shared countless stories and discussed innumerable football and basketball contests.

For my undergraduate education which carried me so far, I thank the members of the Physics Department at the University of Wisconsin-River Falls. Special thanks go to Dr. Neal Prochnow who helped open a number of doors which led to my graduate education.

To my parents, Clare and Dorothy Melin a special appreciation for allowing me to choose my own paths and for instilling in me the value of hard work, knowledge and experience. To Jan and Zophia Porzuczek for their continued encouragement.

To Paul, Jim, Joe, Steve, Wayne and all my friends and members of the Nuclear Beer Group whose companionship will always be remembered. So much of an education comes outside the classroom and laboratories and it is with these people that I have enjoyed this facet of my education.

To my wife, Teresa Porzuczek, for her constant support and help, I dedicate this thesis, for it is she who sacrificed the most and worked the hardest in order that I could complete this work. She kept me going when the work was the hardest and supplied the motivation to continue.

TABLE OF CONTENTS

Chapter	Page
LIST OF TABLES	vii
LIST OF FIGURES	ix
CHAPTER I	
INTRODUCTION	1
MOTIVATION	6
ORGANIZATION	14
CHAPTER II	15
THEORETICAL METHODS	15
Optical Model Potential	15
Deformed Optical Model Potential (DOMP)	19
Multipole Moments	23
COUPLED CHANNELS CALCULATION	27
CHAPTER III	41
EXPERIMENTAL METHOD	41
Introduction	41
Dispersion Matching	42
Particle Detection	51
Target Thickness Monitor	62
Beam Current	65
Targets	65

Chapter	Page
CHAPTER IV.	71
DATA REDUCTION.	71
Optical Model Search.	78
²³⁸ U Analysis	78
²³² Th Data Reduction.	94
²³⁴ U and ²³⁶ U Data Reduction.	104
CHAPTER V	115
RESULTS AND DISCUSSION.	115
APPENDICES	
APPENDIX A.	125
INTRODUCTION.	125
CONSTRUCTION AND PERFORMANCE.	128
ELECTRONICS	136
RESULTS	144
APPENDIX B.	146
POSITION READOUT.	148
DESIGN.	154
TIMING CALCULATIONS	155
ELECTRIC FIELD DISTRIBUTIONS.	157
ELECTRONICS	169
CONSTRUCTION.	182
RESULTS AND DISCUSSION.	189
APPENDIX C.	200
REFERENCES	218

LIST OF TABLES

Table		Page
IV-1	Results of fitting scaled 'data' with DSO calculation and actual 'data' with SSO calculation. The 'data' are calculated values for ^{238}U using 0-2-4-6-8 couplings with deformed spin-orbit in a calculation using the parameters of King, et al. [K179].	84
IV-2	Best fit parameters resulting from fits to ^{238}U data with deformed spin orbit (DSO) and spherical spin orbit (SSO) calculations.	87
IV-3	Values of optical model parameters, deformation parameters, chi square values and moments corresponding to the extreme values of β_2	91
IV-4	Best fit parameters resulting from fits to ^{232}Th data with deformed spin orbit (DSO) and spherical spin orbit (SSO) calculations	105

Table	Page
IV-5	Best fit parameters resulting from fits to ^{236}U data with deformed spin orbit (DSO) and spherical spin orbit (SSO) calculations 113
IV-6	Best fit parameters resulting from fits to ^{234}U data with deformed spin orbit (DSO) and spherical spin orbit (SSO) calculations 114
A-1	Estimation of contributions to line width for thin proportional counters. All contributions in μm are added in quadrature. 127
B-1	Time and spatial resolution for leading edge and constant fraction timing 160
B-2	Calculated active wire operating voltages, gain ratios, and transparencies for various active and guard wire diameters. 181

LIST OF FIGURES

Figure	Page
I-1	Angular distribution for ground state rotational band of ^{238}U for proton scattering at 35 MeV 4
I-2	a) Quadrupole moments of rare earth nuclei. From Reference [Ro77]. b) Hexadecapole moments of rare earth nuclei. From Reference [Ro77]. c) Prediction of trends in quadrupole and hexadecapole moments using formulation of Bertsch 88
I-3	a) Quadrupole moments of actinide nuclei. b) Hexadecapole moments of actinide nuclei. See text for references. 9
I-4	a) Prediction of the trends of the quadrupole, hexadecapole, and hexakontattetarapole moments using formulation of Bertsch. b) The predicted β_6 values [Ni69] for the rare earth nuclei. 13

Figure	Page
II-1	Calculation of Woods-Saxon term and its derivative for a number of diffuseness values. The radius used is $R_0 = 1.17 A^{1/3}$, where $A = 238$ 18
II-2	Comparison of lowest 0^+ , 2^+ , and 4^+ angular distributions for ^{238}U and ^{208}Pb . The lead data is from reference [Wa73]. 22
II-3	Calculated surface shapes illustrating the contributions of the β_2 , β_4 , and β_6 deformation parameters. The symmetry axis is the horizontal axis 25
II-4	Schematic illustrating various coupling routes included in the coupled channels method. The energy level spacing corresponds to that of a deformed rotor. 36
III-1	Schematic illustration of Enge split-pole spectrograph and scattering chamber. 44
III-2	Experimental layout showing the beam transport system used with the spectrograph 47
III-3	Illustration of the two modes used for dispersion matching. For forward angles ($\theta < 90^\circ$), the transmission geometry a) is used. For back angles

Figure	Page
	(θ > 90°), the reflection geometry
	b) is used. 50
III-4	Spectra resulting from 35 MeV protons scattered from a ¹⁷⁶ Yb target for the two modes of dispersion matching; a) transmission, b) reflection, and c) target rotated for reflection mode with the beam transport system set up for transmission mode. Figure III-4c represents the worst possible case where the beam energy spread is enhanced rather than cancelled 53
III-5	Schematic cross section of the inclined cathode delay-line counter. Labeled parts are: a) window frames, b) anode support, c) separator foil, d) anode wires - five active and 4 guards, e) anode wire for ΔE counter, f) pickup stripe board, g) frame for delay line and board, and h) delay line. From Reference [Mk75]. 57
III-6	Schematic (plan view) of counter. From Reference [Mk75] 58
III-7	Schematic of electronics used to acquire the proton scattering data. 61

Figure	Page	
III-8	Comparison of wing and data (good) energy loss bands	64
III-9	Spectra for 35 MeV protons scattered from a ^{234}U target for a number of lab angles showing kinematic shift of target contaminant peaks.	68
IV-1	Spectra and fit line to the 0^+ , 2^+ , and 4^+ states of $^{238}\text{U}(p,p')$ at 57.5° . . .	73
IV-2	Calculated cross sections showing the best fits to the data with and without the β_6 parameter. The best fit for $\beta_6 = 0.0$ is calculated using the parameters of King et al. [Ki79]. . .	77
IV-3	Illustration of the result of adding additional excited states to the coupled channels calculation.	81
IV-4	Illustration of the ratios of a 0-2-4-6 calculation to a 0-2-4-6-8 calculation for each state in ^{238}U . The ratios were used to scale the experimental data to compensate for the omission of the 8^+ state in further calcula- tions	83

Figure	Page
IV-5	Comparison of the best fits to ^{238}U using the deformed spin orbit (DSO) and spherical spin orbit (SSO) cal- culations 89
IV-6	The χ^2 values for the 0^+ , 2^+ , and 4^+ angular distribution data for two ranges of β_2 with corresponding optical model parameters. 93
IV-7	Illustration of the fit to the data resulting from the use of the β_2 parameter which yields a minimum χ^2 value for the 2^+ data in Figure IV-6. 96
IV-8	Illustration of the ratio of a 0-2- 4-6 calculation to a 0-2-4-6-8 cal- culation for each state in ^{232}Th . The ratios were used to scale the experimental data to compensate for the omission of the 8^+ state in further calculations. 99
IV-9	The χ^2 values for a 0^+ , 2^+ , and 4^+ angular distribution data for two ranges of β_2 with corresponding optical model parameters. 101

Figure	Page	
IV-10	Illustration of the fit to the data resulting from the use of the β_2 parameter which yields a minimum χ^2 value for the 2^+ data in Figure IV-9.	103
IV-11	Best fits to the ^{232}Th data for the deformed spin orbit (DSO) and spherical spin orbit (SSO) calculations	107
IV-12	Best fits to the ^{236}U data for the DSO and SSO calculations.	110
IV-13	Best fits to the ^{234}U data for the DSO and SSO calculations.	112
V-1	Calculated moments for this work using the parameters which give a best fit to the data for DSO and SSO calculations.	116
V-2	Comparison of the moments resulting from this work with previous experimental results and microscopic calculations. See text for references . . .	119
V-3	Comparison of the moments obtained using α -particle scattering at 50 MeV	121
A-1	Exploded view of 1 mm thick resistive division counter.	129

Figure	Page
A-2	Position spectrum for 35 MeV elastically scattered protons 132
A-3	Photographs of 2 mm thick resistive division counter. Lower (close-up) photograph is about twice the actual size. 133
A-4	Photographs of 2 mm thick delay line counter. Lower (close-up) photograph is about twice the actual size. 135
A-5	Position spectra using 2 mm thick resistive division counter. 138
A-6	Position spectra using 2 mm thick delay line counter. 140
A-7	Schematic of electronics used with a) resistive division and b) delay line position encoding. 143
B-1	Schematic view of wire plane for MWPC. 147
B-2	Schematic of active and guard wire connections. 147
B-3	Illustration of the times measured to derive position. 152
B-4	Geometry of the counter showing dimensions important to the electrical characteristics of the counter. 152

Figure	Page
B-5	Illustration of the calculated field lines for the counter wire plane. 154
B-6	Fraction of the particle track length arriving within a time segment. 154
B-7	Results of the pulse modeling calculation illustrating the effect of the integration and differentiation time constants on the resolution and pulse height. 159
B-8	Potentials resulting from the preliminary relaxation calculation. 164
B-9	Potentials resulting from the relaxation calculation with the addition of field shaping planes. 166
B-10	Parallel plate capacitor, a) without and b) with the dielectric material inserted. The electric field in the air-gap increases with the dielectric slab 168
B-11	Schematic of preamplifier used in the MWPC. 168
B-12	Photograph of a) bobbin and b) pot-core used to make an isolation pulse transformer 172

Figure	Page
B-13	Frequency and phase response for pot-core transformer. 173
B-14	Photograph of toroidal pulse trans- former used in high voltage isola- tion. 173
B-15	Frequency response curve for a toroidal pulse transformer for various trans- former turn ratios. 174
B-16	Frequency and phase response curve showing the effect of additional cable 174
B-17	Schematic of high voltage supply network 178
B-18	Schematic cross section of MWPC. Labeled parts are: A) gas windows, B) ground foil, C) wire plane, D) wire support insulation, E) covers, F) active wire matrix circuit board, G) energy loss counter, H) separator foil, I) delay line circuit board, and J) field shaping planes 183
B-19	Photograph showing a portion of the wire plane and the electronics housed in the vacuum box 185

Figure	Page
B-20	Schematic of electronics used with MWPC. The time digitizer and ADC's are part of a CAMAC system connected to a PDP 11/45 computer 188
B-21	Comparison spectra for MWPC and delay line counter. Spectrum is of protons scattered from a UF ₄ target 191
B-22	Thick gas cell and spectrograph showing relationship between locus of the scattering and the angle of incidence on the detector 194
B-23	Spectra whose abscissa is angle of incidence on the detector 196
B-24	Position spectra contrasting the result of gating with angle of incidence on the detector 199

CHAPTER I

INTRODUCTION

The shape of the nucleus is one of its most fundamental properties, although precise determination of shape properties remains an outstanding problem. In this thesis, the nuclear shape will mean the radial and angular distribution of nucleons, the nuclear matter distribution. The distribution of protons makes up the charge distribution. These distributions are parameterized; nuclear shape determination means the measurement of parameter values within the framework of the model, some given parameterization.

One of the basic influences the nuclear shape can have is on the stability of nuclei. The stability is related to the balance between the Coulomb repulsion and the surface binding energy. Theoretical calculations have been made for the charge and matter distributions for heavy nuclei, and these calculations have been used to predict the masses and possible stability of superheavy nuclei. The reliability of these predictions is very dependent on the accuracy with which the calculations agree with known nuclei. Hence, it is of considerable interest to systematically measure the shapes of nuclei, especially massive

nuclei, in as much detail as possible in order to test and refine these theories and thereby improve the accuracy and reliability of their predictions.

Nuclei with proton and neutron numbers near closed shells tend to be spherical in shape, while those far away from closed shells tend to have permanent deformations and energy level structures which display rotational bands. The energy level spacings of these bands, electromagnetic transition rates between states in the bands, and the angular distributions of particles inelastically scattered from states in the bands all provide various details of the intrinsic nuclear deformations. In classical physics it is well known that the results of scattering experiments contain shape information. For example, light diffracted by an object carries information about the size and shape of that object. Consider the elastic and inelastic proton scattering angular distributions in Figure I-1, which display a diffraction-like variation of cross section with angle. This distribution of particles scattered from a nucleus can be used to describe the nuclear surface or details of the deformation if the interaction is adequately modeled. The scattering angle is related to the interaction distance between the projectile and the target in such a way that the scattering data, covering a range of angles, map the surface of the nucleus in the form of the scattering cross sections. The measurement of the shape of the

Figure I-1. Angular distribution for ground state rotational band of ^{238}U for proton scattering at 35 MeV.

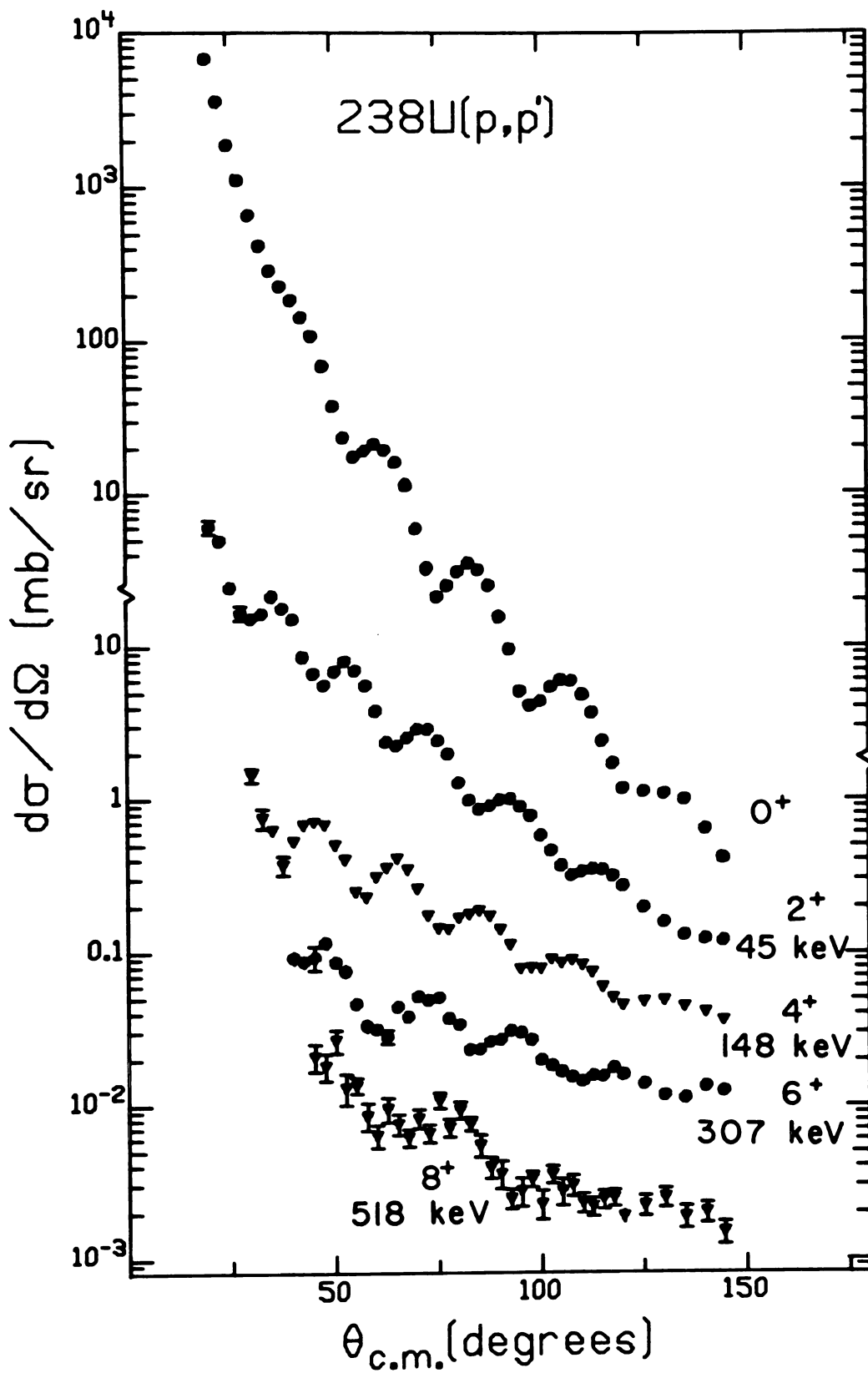


Figure I-1.

nucleus is an indirect measurement because the projectile interacts with the field or potential resulting from the distribution of nucleons. The observed data may be described by modelling the interaction, which is a function of parameters related to the shape of the object causing the scattering. A deformed optical model potential (DOMP), is used to describe the particle scattering data in the present work. Similar to light scattering, the model contains terms to describe the scattering and absorption of the projectile nuclei by the target nuclei. As the name implies, the surfaces in this model can be deformed with the deformations expressed as a deviation from spherical shape. The surface can be expressed as an expansion in terms of spherical harmonics. The coefficients in this expansion are the deformation parameters. The shape can also be expressed in terms of the multipole moments, which are related to the deformation parameters. For example, to first order, the quadrupole moment is proportional to the quadrupole deformation parameter β_2 . Using this model, information about the shape of a nucleus can be determined much like the reconstruction of the details of an object from the observation of the light that it reflects or scatters.

To summarize, the measurement of the deformation of a nucleus is carried out by describing the elastic and inelastic scattering cross sections with a model which has parameters explicitly related to its shape.

MOTIVATION

Both the rare earth and actinide regions lie between closed shells and are known to contain permanently deformed nuclei. Systematic studies of these nuclei have shown trends of large quadrupole deformations between closed shells and a sign change of the hexadecapole deformation in the same region.

Bertsch [Be68] has explained this systematic behavior using an observation of the effect on the nucleus by adding nucleons into the unfilled shells. In filling the shell, the nucleons are added nearest the symmetry axis, which increases the quadrupole moment. The addition of more nucleons fills the orbits near the equatorial region resulting in a tendency toward a more spherical shape. Figure I-2 shows the measured quadrupole and hexadecapole moments for the rare earth nuclei and Bertsch's predictions of these systematics.

Moments for the actinide nuclei have been measured by a variety of experimental techniques. Methods used include proton scattering at 23 MeV [Mo71] and at 35 MeV [Ki79], α -particle scattering at 50 MeV [He73, Da76], Coulomb excitation [Be73], and electron scattering [Co76]. The values of the moments from these measurements are plotted in Figure I-3 in addition to predictions based on microscopic calculations [Ne74, Ne76]. The microscopic calculations

Figure I-2. (a) Quadrupole moments of rare earth nuclei. From Reference [Ro77]. (b) Hexadecapole moments of rare earth nuclei. From Reference [Ro77]. (c) Prediction of trends in quadrupole and hexadecapole moments using formulation of Bertsch.

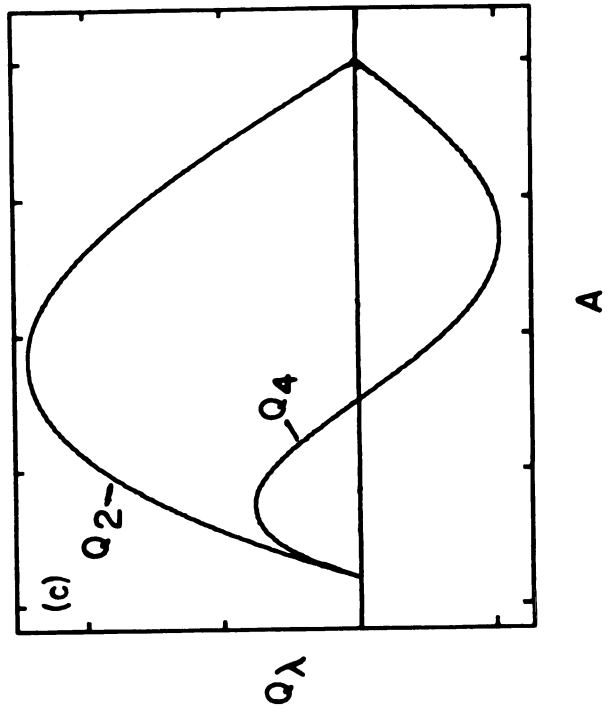
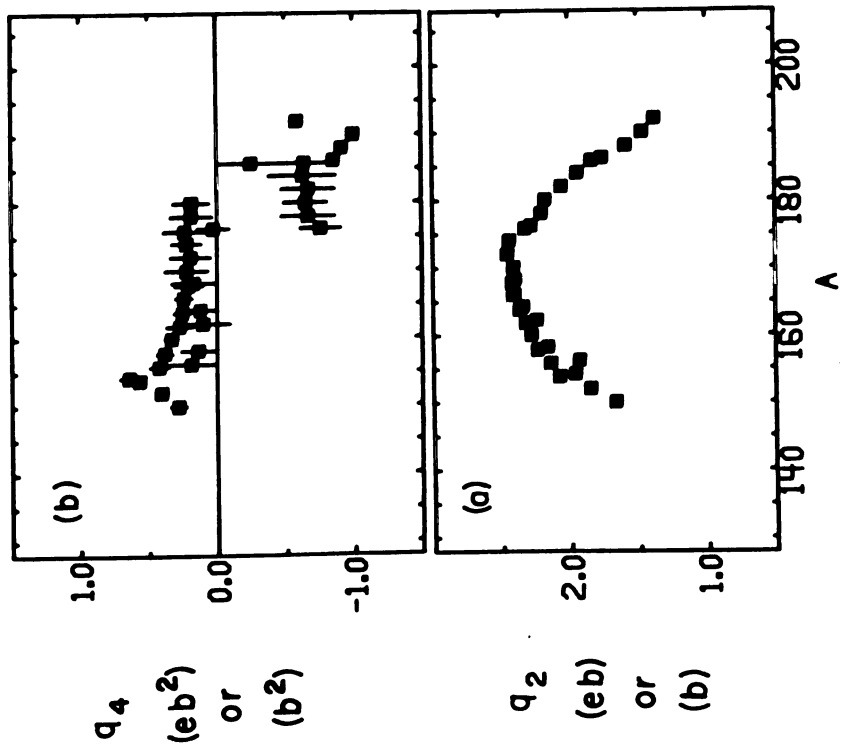


Figure I-2.

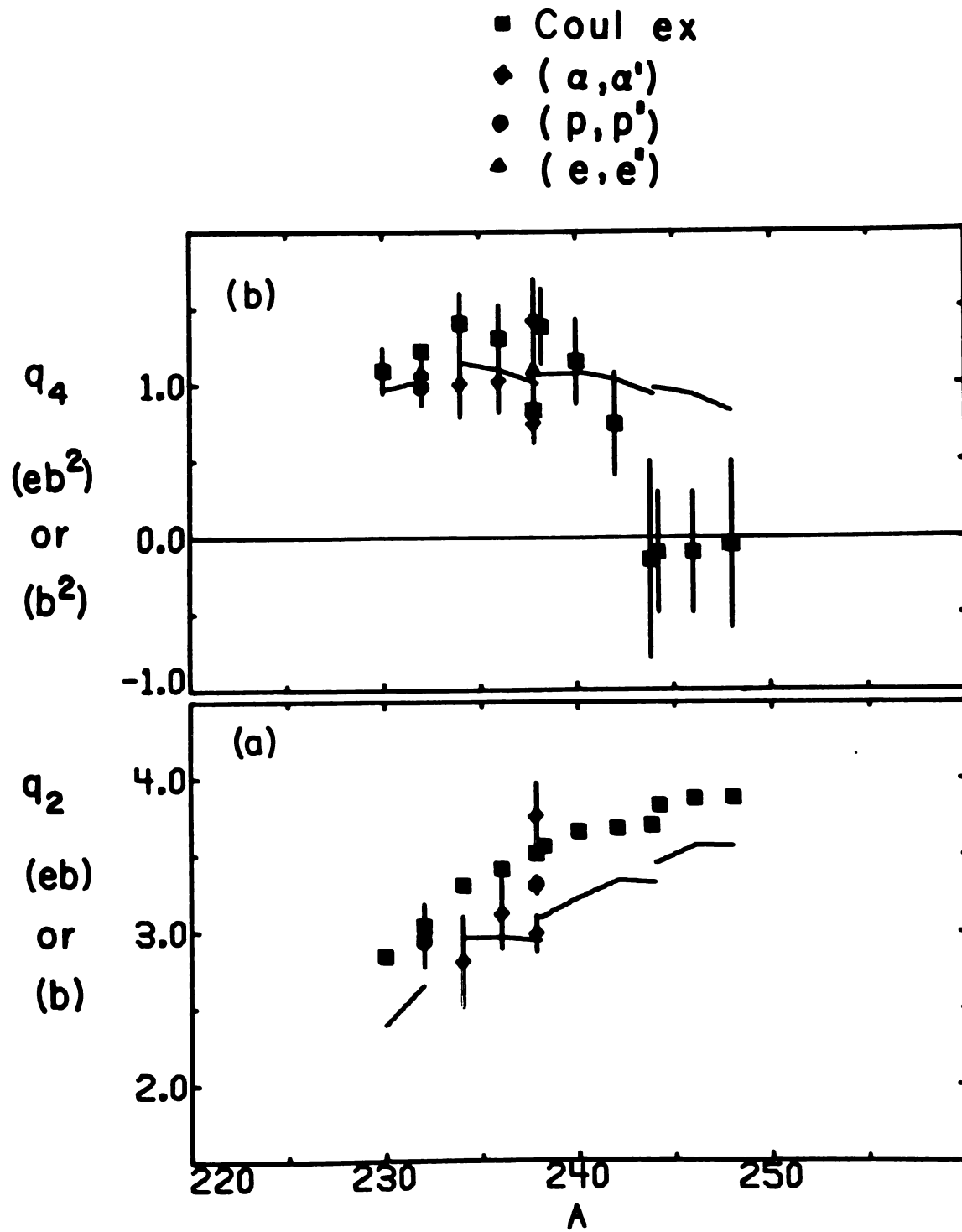


Figure I-3. (a) Quadrupole moments of actinide nuclei.
 (b) Hexadecapole moments of actinide nuclei.
 See text for references.

involve minimizing the nuclear potential energy as a function of the deformations and evaluating the moments. Although there is qualitative agreement between the measured and predicted values, the results of the measurements show some disagreement in both trends and magnitudes. The Coulomb excitation measurements follow the trends of the theoretical predictions but differ in magnitude. The α -particle scattering [Da76] results show disagreement with the previous α -particle scattering [He73] results and with the Coulomb excitation measurement in both trend and magnitude. Since the experimental methods are different, with each method having a different sensitivity to the proton and neutron distribution, the difference in the results may be attributed to a difference in the shape being measured or to a possible breakdown of the model used in the analysis.

The proton is used in this work because it is a simple hadronic probe which may lead to a fairly unambiguous model independent analysis. At a beam energy sufficiently above the Coulomb barrier the proton is more sensitive to the neutron matter distribution of the nucleus than it is to the proton or charge distribution [Ma77, Ma78]. Coulomb excitation and electron scattering (e, e') reactions are only sensitive to the charge distribution, whereas α -particle scattering at an energy of 50 MeV is about 50% Coulomb excitation. Proton scattering at an energy of 35 MeV is sufficiently above the Coulomb barrier so as to be

dominated by the nuclear potentials.

Most measurements to date in both the rare earth and actinide regions have been concerned with the quadrupole (q_2) and hexadecapole (q_4) moments, whereas very few have had any sensitivity to the hexakontattetarapole (q_6) moment. Previous work on ^{238}U (p,p') indicated the possible need for a β_6 deformation [Mo71], while a subsequent survey of (α,α') reactions on rare earths and ^{238}U indicate a general improvement in fits to the data by including a β_6 term [He73]. The proton scattering by King et al. [Ki79] at 35 MeV shows considerable structure in the higher excited state angular distributions which is necessary to have sensitivity to the higher order deformations in addition to the quadrupole and hexadecapole deformations.

By extending Bertsch's idea to the β_6 deformations and values of the q_6 moment, Figure I-4, the β_6 value can be expected to change sign twice in a region where the hexadecapole deformation changes sign once. In addition the first sign change can be expected in the portion of the region near uranium. Figure I-4 also contains microscopic calculations [Ni69] for the β_6 parameter for the rare earth nuclei showing a trend similar to that predicted by the Bertsch formalism. The purpose of the present work was to extend the survey of King, et al. to demonstrate the sensitivity of using proton scattering in the study of shape properties of the actinide nuclei and to do a systematic

Figure I-4. (a) Prediction of the trends of the quadrupole, hexadecapole, and hexakontattetarapole moments using formulation of Bertsch. (b) The predicted β_6 values [Ni69] for the rare earth nuclei.

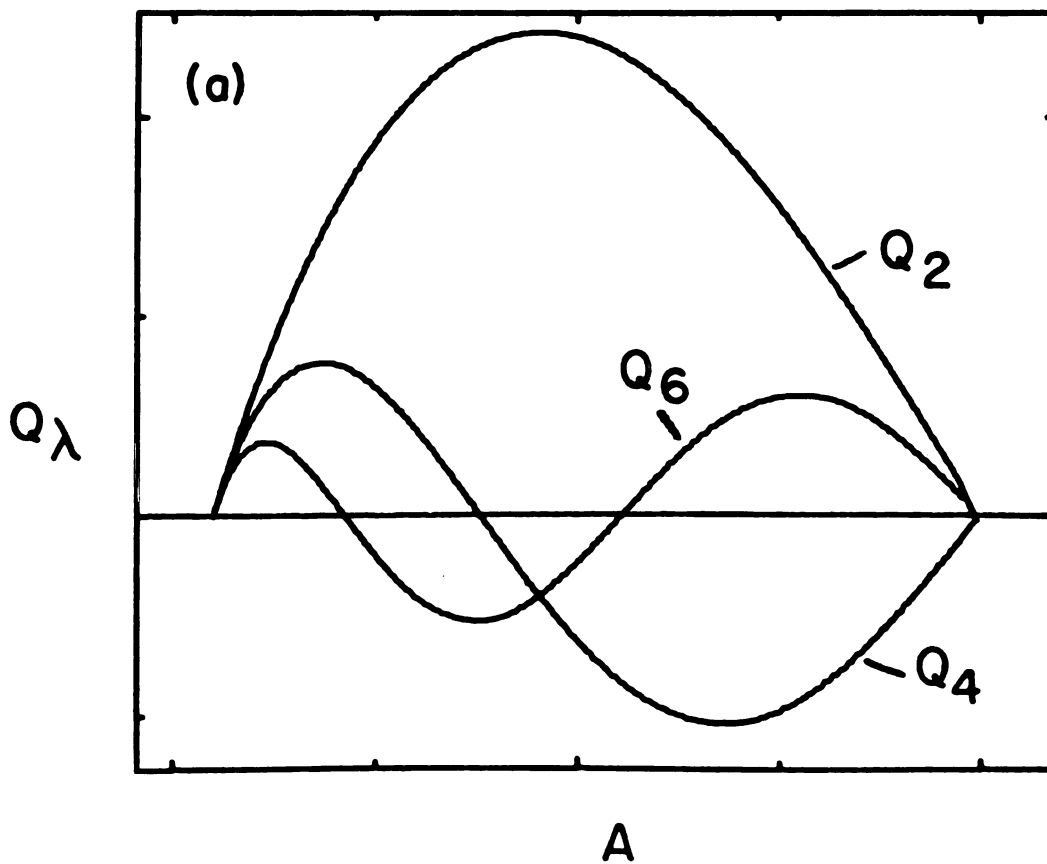
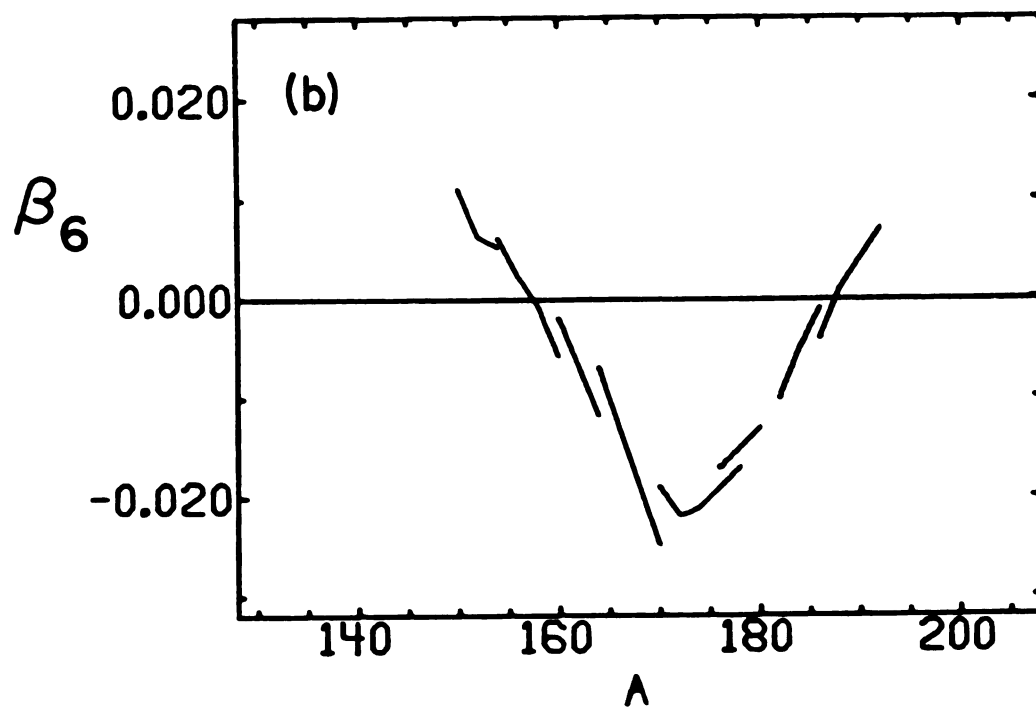


Figure I-4

study of the moments to test various experimental results and theoretical predictions.

ORGANIZATION

The following chapter discusses the theoretical model, its derivation and use, and techniques used to describe the data. In this work, the deformed optical model is used with a coupled channels formulation to describe the scattering cross sections for protons from the actinide nuclei. Chapter III describes the experimental setup and procedures used to gather the experimental data. The technique of dispersion matching, particle detection, and the targets used are described. In Chapter IV the data reduction and analysis are described. Chapter V contains the results of the analysis and a discussion of the significance of the results. In addition to the scattering experiment described in this thesis, Appendices A and B contain descriptions of the work associated with the development of position sensitive proportional counters. The first appendix deals with short high position resolution proportional detectors, while the second reports on the design, development, and testing of a multiwire proportional counter.

CHAPTER II

THEORETICAL METHODS

Optical Model Potential

The optical model potential for proton scattering from nuclei is analogous to light scattering from a cloudy crystal ball. The potential has a real part which accounts for scattering and an imaginary part which accounts for absorption of nucleons incident on the target nucleus. A summary of the optical model formalism is based on discussions by Hodgson [Ho63] and a number of textbooks [Pr62,MS70]. The general expression for the potential of the target nucleus is

$$V_o(\vec{r}) = V_c - Vf(\vec{r}) - i(Wg(\vec{r})+W_Dg'(\vec{r}))-(V_{SO}+iW_{SO})h(\vec{r}) \quad (\text{II-1})$$

The terms in this equation will be defined in the following text. The Coulomb interaction potential V_c is

$$V_c = Z_I Z_T e^2 \int \frac{\rho(r',\theta',\phi')d^3r'}{|\vec{r} - \vec{r}'|} \quad (\text{II-2})$$

where Z_I and Z_T are the charges of the projectile and target

nuclei. The charge distribution within the nucleus is given by $\rho(r, \theta, \phi)$. The charge distribution will be assumed to be of constant density but deformed and can be written as

$$\begin{aligned} \rho(r, \theta, \phi) &= \frac{3}{4\pi} R_c^3 & r < R_c(\theta, \phi) \\ &= 0 & r > R_c(\theta, \phi) \end{aligned} \quad (\text{II-3})$$

where R_c is the Coulomb radius. The angular dependence of the radii will be defined below. By using the expansion

$$\frac{1}{|\vec{r} - \vec{r}'|} = 4\pi \sum_{\ell=0}^{\infty} \sum_{m=-\ell}^{\ell} \frac{1}{2^{\ell+1}} \frac{r_{<}^{\ell}}{r_{>}^{\ell+1}} Y_{\ell m}^*(\theta', \phi') Y_{\ell m}(\theta, \phi) \quad (\text{II-4})$$

where $r_{<}$ ($r_{>}$) is the smaller (larger) of $|\vec{r}|$ and $|\vec{r}'|$. The Coulomb potential becomes

$$\begin{aligned} V_c &= \frac{3}{4\pi} Z_I Z_T e^2 \sum_{\ell m} \int \frac{r'^2}{2^{\ell+1}} \frac{r_{<}^{\ell}}{r_{>}^{\ell+1}} \rho(r', \theta', \phi') \times \\ &Y_{\ell m}(\theta', \phi') Y_{\ell m}(\theta, \phi) dr' d\Omega \end{aligned} \quad (\text{II-5})$$

The real well has a depth V and a radial form which may be defined using a Woods-Saxon form

$$f(r) = \{1 + \exp[(r-R)/a]\}^{-1} \quad (\text{II-6})$$

where R is the radius and a is the diffuseness. An

illustration of this function appears in Figure II-1a.

The imaginary portion of the potential has two terms, a volume term with well depth W and a surface term with well depth W_D . The surface term is used to include the effect of strong absorption at the nuclear surface. The form for the shape of the volume term is identical to the form for the real volume term although the radius and diffuseness may be different.

The surface imaginary term requires a radial form which is surface peaked. A possible expression is the derivative of the volume term

$$g'(r) = -4a_1 \frac{d}{dr}g(r) = \exp\left(\frac{r_1-R}{a_1}\right)\left\{1+\exp\left(\frac{r_1-R}{a_1}\right)\right\}^{-2} \quad (\text{II-7})$$

The normalization factor $4a_1$ causes the maximum value to be unity. Although there is no theoretical basis for this definition, the parameterization has the advantage of introducing no new variables and maintaining consistency in the model. Figure II-1b illustrates various calculations of the derivative of the volume term for a number of diffuseness values. Another possible form for $g'(r)$ is a Gaussian term but this appears to have no added advantages.

The spin-orbit portion with well depths V_{SO} and W_{SO} are used to explicitly include the interaction between the spin of the projectile and its orbital angular momentum relative to the target nucleus. This portion of the

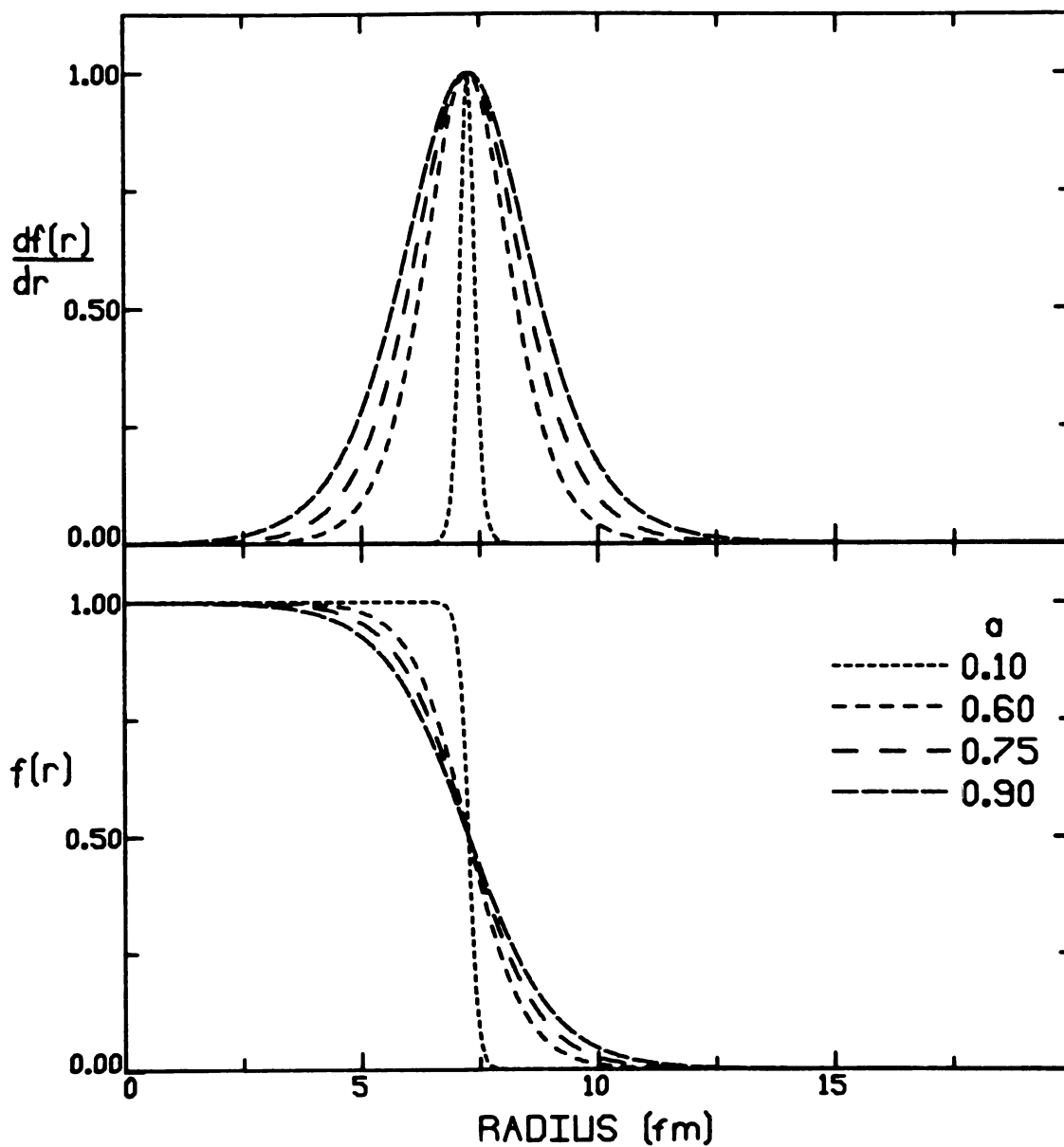


Figure II-1. Calculation of the Woods-Saxon term and its derivative for a number of diffuseness values. The radius used is $R = 1.17 A^{1/3}$, where $A = 238$.

potential is also surface peaked. An expression for the shape term $h(r)$ is the Thomas form,

$$h(r) = - (\hbar/m_{\pi}c)^2 \frac{1}{r} \frac{d}{dr} f(r) \quad (\text{II-8})$$

where m_{π} is the pion mass. The radius and diffuseness may be different from those of the real and imaginary portions. The spin-orbit radius is typically 20-30% smaller than either the real or imaginary radii. The imaginary spin-orbit term will be neglected since it is not required unless polarization data is being fitted.

Deformed Optical Model Potential (DOMP)

For deformed nuclei, the surface of the nucleus is defined by the expression of R . For spherical nuclei, R would be independent of angle and only depend on the nuclear mass for constant densities, $R_0 = r_0 A^{1/3}$ where r_0 is a constant and A is the nuclear mass. The existence of rotational energy levels in some nuclei indicates that the ground states of these nuclei can be treated as permanently deformed rotors. The deformation of the potential surface may be introduced by expressing the radius as a function of angle (assuming axial symmetry),

$$R = r_0 A^{1/3} \left(1 + \sum_{\lambda} \beta_{\lambda} Y_{\lambda 0}(\hat{r}) \right) \quad (\text{II-9})$$

where β_λ are the deformation parameters, and \hat{r} is the angular component of \vec{r} . To maintain consistency this form will be used to express the angular dependence of the radii in Equation II-1. This expression is simplified by including only the even λ terms. The $\lambda = 0$ term is excluded since this term would only serve as a normalization term. The $\lambda = 1$ term corresponds to the motion of the center of mass of the nucleus which can be eliminated. The $\lambda = 3$ term corresponds to an octupole deformation of the nucleus. Since there has been no observation of an octupole moment in the ground state of nuclei this term is also neglected. The odd terms would result in a form which would violate parity. In general, the odd terms are neglected to maintain a symmetry for rotation by π .

For rotational nuclei, the excited states of the rotations of the ground state have the same intrinsic structure, with the excitation energy appearing as rotational energy of the nucleus. The elastic scattering is defined by the diagonal elements of the effective interaction in the intrinsic ground state. The angular distribution for each state contains information such as the phase, amplitude, and frequency of the oscillations, and the slope and magnitude of the cross sections. Consider Figure II-2 which shows angular distributions for the lowest 0^+ , 2^+ , and 4^+ states in ^{238}U and ^{208}Pb [Wa73]. The difference in the structure of the angular distributions of all states is

Figure II-2. Comparison of lowest 0^+ , 2^+ , and 4^+ angular distributions for ^{238}U and ^{208}Pb . The ^{208}Pb data are from Reference [Wa73].

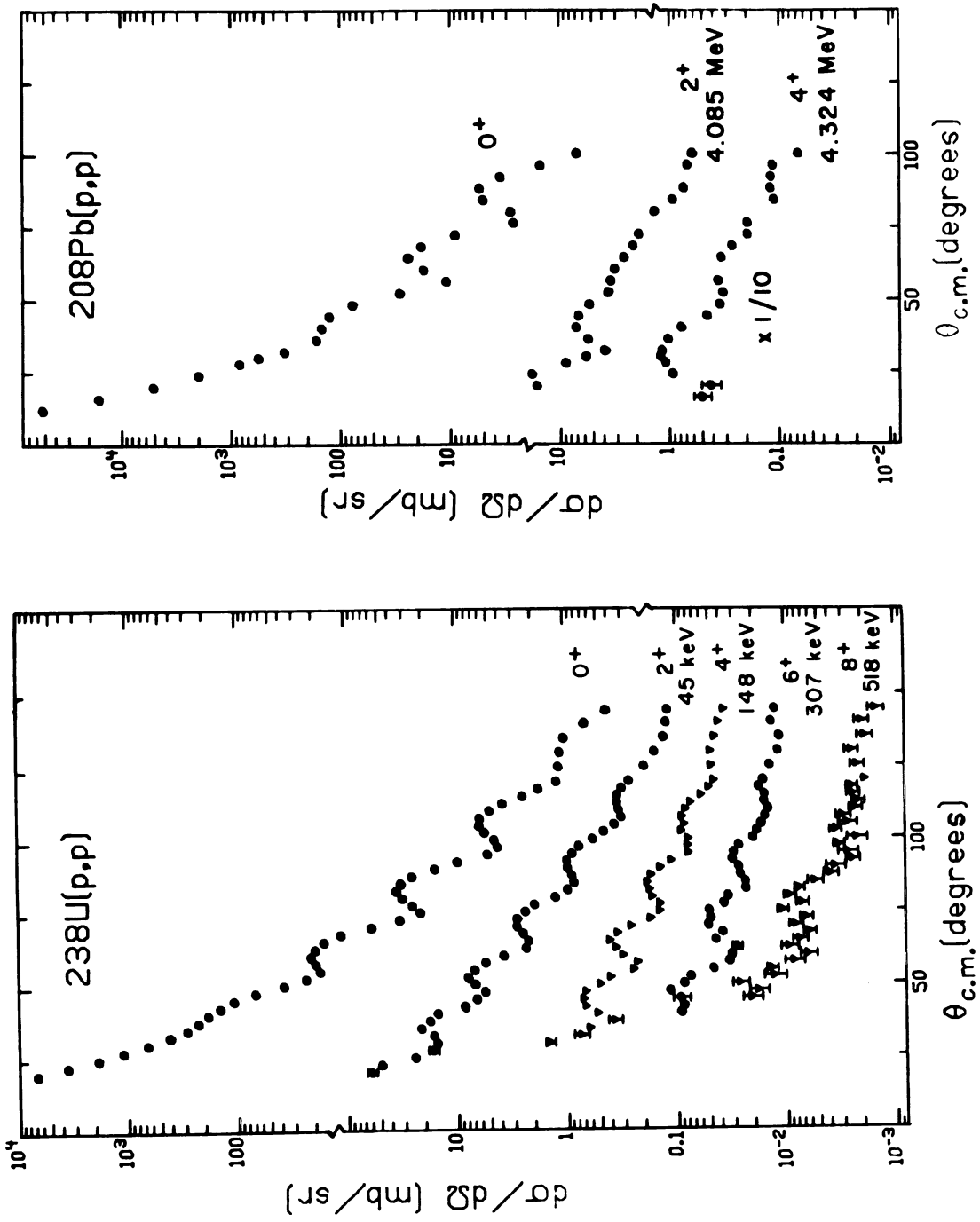


Figure II-2

due to the difference in the shape of the two nuclei, the lead nucleus being spherical and the uranium nucleus being permanently deformed. From the analysis of the angular distributions, information about the shapes of these nuclei can be obtained.

Multipole Moments

The contributions of the various β_λ terms to the shape of a surface, Figure II-3, can be related to the multipole moments of the nucleus. For example, the β_2 term reflects an elongation of the nucleus giving rise to a quadrupole moment (q_2), and the β_4 term gives rise to a hexadecapole moment (q_4). The moment is defined by the relation in Equation II-10. The integral of the potential over the nuclear volume is used to evaluate the moment

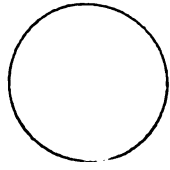
$$q_\lambda = \int r^\lambda Y_{\lambda 0}(\hat{r}) \rho(\bar{r}) d^3\bar{r} \quad (\text{II-10})$$

For a sharp edged distribution with deformation parameter β_2 the corresponding quadrupole moment is given by

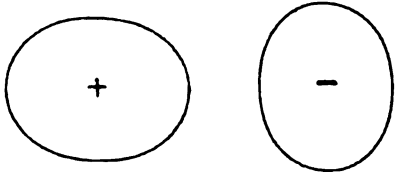
$$q_2 = \frac{3}{4\pi} \frac{R_0^2 (\beta_2 + 0.3604 \beta_2^2 + \dots)}{(1 + 0.2387 \beta_2 + 0.0143 \beta_2^2)} \quad (\text{II-11})$$

The β_6 term leads to the hexakontattetara moment (q_6).

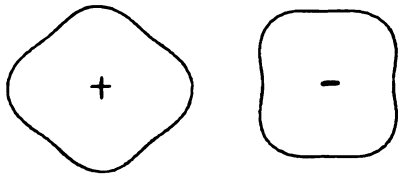
Figure II-3. Calculated surface shapes illustrating the contributions of the β_2 , β_4 , and β_6 deformation parameters. The symmetry axis is the horizontal axis.



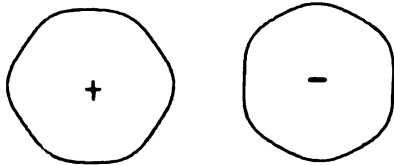
$$\beta_2 = \beta_4 = \beta_6 = 0.0$$



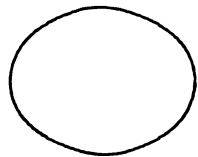
$$\beta_2 = \pm 0.250$$



$$\beta_4 = \pm 0.200$$



$$\beta_6 = \pm 0.050$$


 ^{238}U

$$\beta_2 = 0.226$$

$$\beta_4 = 0.054$$

$$\beta_6 = -0.011$$

$$R = R_0 (1 + \beta_2 Y_{20} + \beta_4 Y_{40} + \beta_6 Y_{60} + \dots)$$

Figure II-3

The values of deformation parameters extracted from scattering experiments are model dependent on the distribution used, as well as the model of the interaction.

The ambiguity of the model dependent parameters is illustrated by the coupling of the deformations and the nuclear radius. The cross sections depend on β but through the term $R\beta$, where R is the radius. A defined quantity, the deformation length, $\delta_\lambda = R\beta_\lambda$ is a less ambiguous parameter and can be used to compare results of various experiments. The deformation length may be compared to the displacement of the surface, $\delta R = R\beta_\lambda Y_{\lambda 0}^*(\hat{r})$, which may be a physically significant term. This factor may still contain ambiguities as the value of $R\beta_\lambda$ may also depend on the other optical model parameters.

Mackintosh [Ma76] has used a theorem due to Satchler [Sa72] to state that a folding model with a density independent interaction leads to folded potentials with the same multipole moments as those of the nuclear density. The assumption that the DOMP is derivable from a folding model leads to quantities which are more significant than the potential deformation parameters and should be related simply to the underlying nuclear moments. Mackintosh [Ma76] has found reasonable agreement for the folded quadrupole moment and the underlying nuclear moment for light nuclei. For heavy nuclei, alternative arguments point to either a breakdown of the application of Satchler's theorem or that

the nuclear deformation of the proton component is greater than the neutron component for the hexadecapole degree of freedom. For the actinide nuclei the q_{20} moment for the neutron distribution was about 10% higher than that of the proton distribution [Ma76]. The q_{40} moment for the proton distribution was found to be about 20% larger than the neutron distribution. An additional finding is that for α -particles the theorem application breaks down for heavy nuclei.

COUPLED CHANNELS CALCULATION

For proton scattering from a nucleus, the interaction strongly depends on the energy of the incident projectile. For energies below the Coulomb barrier the proton interacts only with the Coulomb field of the nucleus. At higher energies it interacts with the nuclear field where it can be either scattered or absorbed. The nucleus may be left in an excited state if the proton deposits energy in the nucleus. At sufficiently high incident energies, the number of excitation channels becomes infinite as the nucleus may be excited to any of its discrete or continuum states. Excitations may be direct or involve a cascade through two or more states (multistep excitations). When a cascade is involved, the interaction is a result of the coupling of the involved channels. The coupling is a complicated

mechanism and requires a special formulation.

The method of coupled channels consists of explicitly considering transitions between a number of strongly coupled states during the scattering process. In practice, the coupled channels space is severely truncated by the consideration of a limited number of channels. An important effect which is omitted is the excitations which involve the neglected channels as intermediate states and reactions such as (p,d), (p,t), etc. The truncation will lead to inaccuracies due to limitations placed on the vector space. To improve the accuracy an effective interaction which compensates for the neglected channels is desired. This interaction would be a complex non-local potential. It has been shown that an equivalent complex local potential can be used to replace the non-local potential. The DOMP contains a complex local potential which makes up its absorptive portion. The optical model is a phenomenological potential, not currently totally derivable from first principles. The parameterization is obtained through the fitting of the experimental data. Consequently, the fitting of the data will produce the effective interaction to compensate for the truncated space considered with the coupled channels calculation.

The coupled channels calculation entails a quantum mechanical solution of the Schrodinger wave equation (SWE). The eigenfunctions for the nucleus are defined by

$$H_A \phi_{\alpha J}(\vec{A}) = E_{\alpha J} \phi_{\alpha J}(\vec{A}) \quad (\text{II-12})$$

where H_A is the Hamiltonian for a nucleus with mass A , $E_{\alpha J}$ are the energy levels of the nucleus, and \vec{A} are the internal coordinates of the nucleus. The quantum number J denotes angular momentum of the nucleus with α containing all other quantum numbers required to describe the nucleus.

To consider the interaction of the nucleus with the projectile, in this case a proton, the total Hamiltonian becomes

$$H = H_A + T + V(\vec{r}, \vec{A}) \quad (\text{II-13})$$

where T is the kinetic energy of the proton and $V(\vec{r}, \vec{A})$ is the interaction of the projectile with the nucleus. The solution to the scattering problem is defined by

$$(H-E)\psi(\vec{r}, \vec{A}) = 0 \quad (\text{II-14})$$

with the appropriate boundary conditions. The quantum numbers αJ describe the nuclear state and the incident proton can be described using three additional quantum numbers jls . For simplicity in notation let $c = \alpha J j l s$ denote the nucleus and projectile in their initial state and c' denote any other possible state for the target and projectile.

The nuclear wave functions $\phi_{\alpha J}(A)$ form a complete orthonormal set so that $\psi(\vec{r}, \vec{A})$ may be expanded in terms of the wave functions for the nucleus and for the incident proton. It is advantageous to express the solution in terms of the total angular momentum I and parity π

$$\vec{I} = \vec{J} + \vec{J}, \quad \pi = (-1)^{\ell} \quad (\text{II-15})$$

Thus we have

$$\psi_{cI\pi}^m(\vec{r}, \vec{A}) = \sum_c \phi_{\alpha J} \phi_{cI\pi}(\vec{r}, \vec{\sigma}), \quad (\text{II-16})$$

where the term $\phi_{cI\pi}$ describes the relative motion between the nucleus and projectile. The term $\vec{\sigma}$ has been included to explicitly include the spin of the projectile. The wave function describing the relative motion may be expanded to separate out the spin and angular dependent terms

$$\phi_{cI\pi}(\vec{r}, \vec{\sigma}) = \frac{U_c(r)}{r} \phi_{cI\pi}(\hat{r}, \vec{\sigma}) \quad (\text{II-17})$$

where

$$\phi_{cI\pi}(\hat{r}, \vec{\sigma}) = C Y_{\ell m}(\hat{r}) \chi_c(\vec{\sigma}) \quad (\text{II-18})$$

where $U_c(r)$ is a radial wave function, C contains the numerical factors, and $Y_{\ell m}(\hat{r})$ are the spherical harmonics

which only depend on \hat{r} , where \hat{r} are the polar coordinates of \vec{r} . The expression $\chi_c(\vec{\sigma})$ is a spin function for the incident projectile.

Inserting Equation II-17 into Equation II-16, allows the solution of Equation II-14. This can be accomplished by multiplying by ϕ^* from the left and using the orthogonality of the components of ϕ^* . The result is a set of coupled equations for the radial wave function

$$(T_{c',c'} - V_{c',c'}(r) - E_{c'})U_{c'}(r) = - \sum_{c'' \neq c'} V_{c',c''}^I(r)U_{c''}(r) \quad (\text{II-19})$$

where

$$T_{c',c'} = \frac{\hbar^2}{2m} \left(\frac{d^2}{dr^2} + \frac{\ell(\ell+1)}{r^2} \right), \quad E_{c'} = -E_{\alpha J} + E \quad (\text{II-20})$$

$$k^2 = 2\pi E_{c'}/\hbar^2$$

where E is the bombarding energy and m is the reduced mass.

The matrix element $V_{c',c''}$ is

$$V_{c',c''}^I = \langle \phi_{c',I\pi}(\hat{r}, \vec{A}) | V(\vec{r}, \vec{A}) | \phi_{c'',I\pi}(\hat{r}, \vec{A}) \rangle \quad (\text{II-21})$$

The integration implied is only over the polar coordinates of \vec{r} and over all the internal coordinates \vec{A} . The resultant matrix element is a function of $r = |\vec{r}|$. Since $V(\vec{r}, \vec{A})$ is a scalar potential, $V_{c',c''}$ is diagonal in I and π and independent of m .

Two effects have been neglected in the above derivation. Since the proton is treated as a free particle, reactions such as pickup are excluded. Proton exchange with one in the target is also excluded by not allowing the overlap of the two wave functions. The number of channels in equation II-19 is equal to the number of possible couplings between the excited states which includes both the discrete and the continuum states yielding an infinite number of possible channels. To reduce the magnitude of the problem, the number of inelastic channels is limited to those with large cross sections and to other states of interest. In the present work, only the states of the ground state rotational band are included. The wave function is expanded in terms of the wave functions of the elastic scattering channel and one or more of the inelastic scattering channels. This leads to a finite problem which can be solved numerically using a computer.

When considering a certain number of states, the number of channels far exceeds the number of states. Recall that $c = \alpha J l j s$ labels a particular state and angular momentum of the scattered particle. For the total angular momentum I and parity π and for each state αJ there are a number of scattered particles $j l s$ which satisfy the quantum number relationships in Equation II-15. For a spin $1/2$ particle there are $2J+1$ couplings allowed. For each I, π value there are

$$N = \sum_{\text{states}} (2J+1) \quad (\text{II-22})$$

coupled channels, where the sum is over the states of the nucleus. A calculation involving the 0^+ , 2^+ , 4^+ , and 6^+ states contains 28 coupled channels. Adding the 8^+ state increases that number by 17. The number of differential equations also depends on the angular momentum of the incident particle. The angular momentum of the incident partial waves ranges from 0 to ℓ_{max} where $\ell_{\text{max}} = 2kR$, where R is the radius at which the interactions are effectively zero. For each ℓ there are $2j$ states giving a total number of differential equations of $4kRN^2$.

In solving the equations there is a coupled differential equation for each channel involved. Each equation has two boundary conditions, the first at the origin where the wave function must vanish. The second boundary condition exists at the exterior of the nucleus where the nuclear force vanishes. The wave functions become decoupled and the solutions are the Coulomb functions when the projectile is a proton. For a more detailed discussion of the boundary conditions and methods of solution, see Glendenning [G167], or Hodgson [Ho71].

An additional simplification leads to a well known method used to solve certain types of scattering problems. The Distorted Wave Born approximation (DWBA) is the result of considering only the transition which go directly from

the ground state such as transitions 1, 2, and 3 in Figure II-4. This reduces the differential equation for the target channel to an uncoupled differential equation and also the excited states channels are coupled only to the ground state channel. The coupled differential equations become

$$(T_c - V_{cc}^I - E_c)U_c^O(r) = 0 \quad \text{target channel (II-23)}$$

$$(T_c, -V_{c,c'}^I, -E_{c'})U_{c'}^O(r) = -V_{c,c'}U_c^O \quad \text{excited state channel (II-24)}$$

where c denotes the ground state and c' is an excited state. This method is suitable if excited states are not strongly coupled so that higher order transitions as 4, 5, 6 and 7 in Figure II-4 may be neglected.

Qualitatively, collective transitions in vibrational nuclei are not too strong, allowing the use of the Distorted Wave Born Approximation (DWBA). The transitions in deformed nuclei are quite strong. For ^{238}U the strength of the first excited state (2^+) always exceeds that of the ground state for scattering angles beyond 90 degrees. At more forward angles, the cross sections of the ground state and 2^+ are also comparable, as in the region of 70 degrees. Higher order transitions which involve the 2^+ level as an intermediate state cannot be neglected. Thus additional channels must be considered for deformed nuclei than are

Figure II-4. Schematic illustrating various coupling routes included in the coupled channels method. The energy level spacing corresponds to that of a deformed rotor.

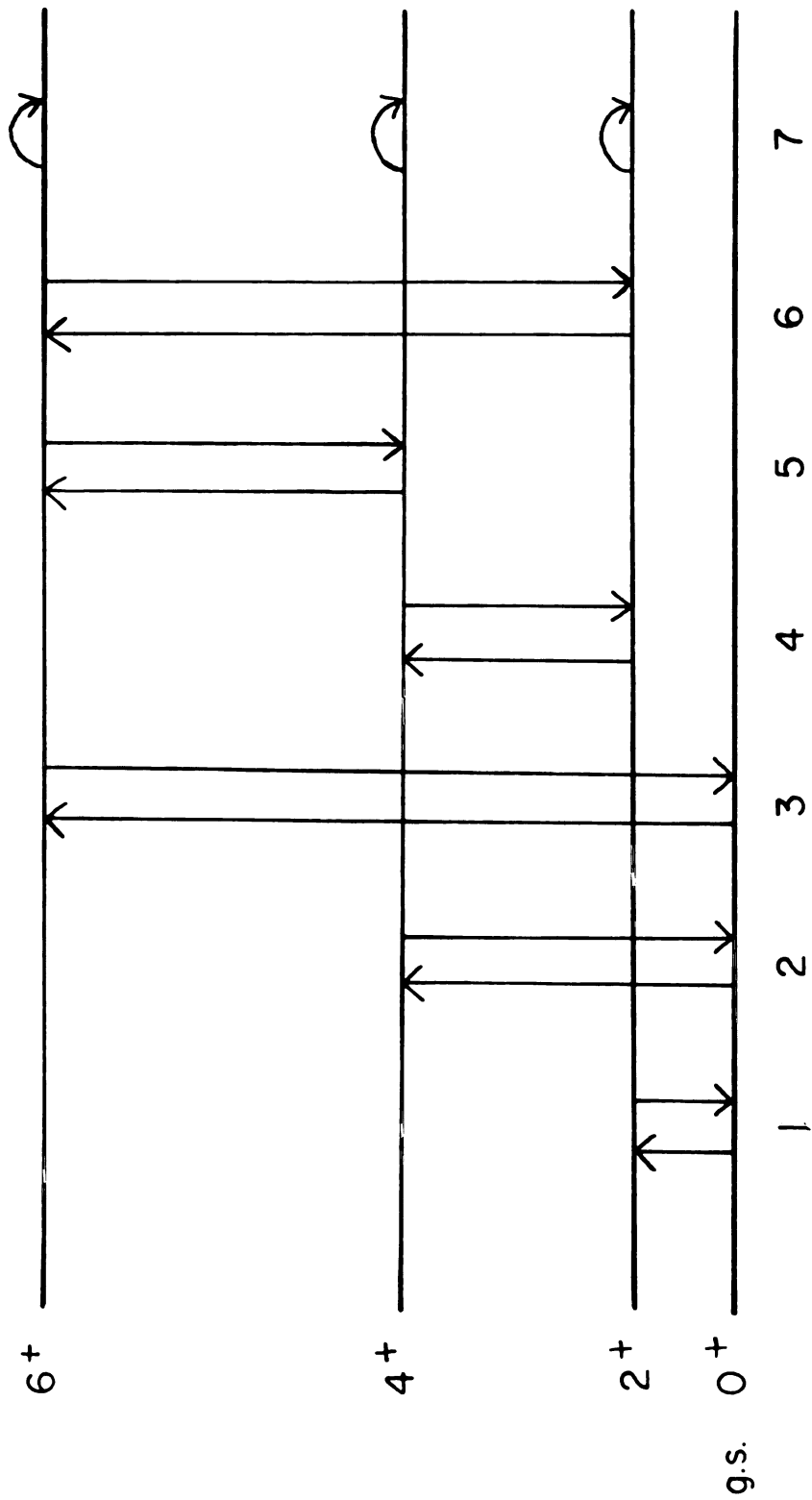


Figure II-4

considered using the DWBA. For example, transitions which populate the 2^+ state include 1, 2+4, 3+6, 1+7, . . . in Figure II-4. The inclusion of the additional channels complicates the solution of Equation II-19 as the equations are numerous and coupled.

The solution for the wave function should be a plane wave plus an outgoing wave given by

$$\begin{aligned} \psi_{\sigma} &= \exp(i\vec{k}\cdot\vec{r} + i\eta \ln(kr - \vec{k}\cdot\vec{r})) |\sigma\rangle \\ &+ \sum_{\sigma'} \frac{1}{r} F_{\sigma\sigma'}(\theta) \exp(ikr - i\eta \ln(kr)) |\sigma'\rangle \end{aligned} \quad (\text{II-25})$$

where σ is the component of the spin at infinity, \vec{k} is the momentum, and $\eta = Z_t Z_i e^2 / h^2 k$ the Coulomb parameter. The angular-momentum expansion of the solution becomes

$$\begin{aligned} \psi_{\sigma} &= \frac{4\pi}{kr} \sum_{\ell} i^{\ell} \exp(i\sigma_{\ell}) U_{\ell J}(r) \langle \ell s u \sigma | j m \rangle \langle \ell s u' \sigma' | \ell m \rangle \\ &\times Y_{\ell u}(\hat{k}) Y_{\ell u'}(\hat{r}) |\sigma'\rangle \end{aligned} \quad (\text{II-26})$$

where σ_{ℓ} is the Coulomb phase shift. The asymptotic expression for the radial wave function can be expressed in terms of the regular and irregular Coulomb functions

$$U_{j\ell}(r) = F_{\ell}(\eta, kr) + C_{\ell}^j (G_{\ell}(\eta, kr) + iF_{\ell}(\eta, kr)) \quad (\text{II-27})$$

Equation II-26 becomes

$$F_{\sigma\sigma'} = \delta_{\sigma\sigma'} F_c(\theta) + \frac{4\pi}{k} \sum_{\ell} \exp(2i\sigma_{\ell}) c_{\ell}^J \langle \ell s u \sigma | j m \rangle$$

$$\times \langle \ell s u' \sigma' | j m \rangle Y_{\ell u}(\hat{k}) Y_{\ell u'}(\hat{r}) | \sigma' \rangle \quad (\text{II-28})$$

where $F_c(\theta)$ is the Coulomb amplitude

$$F_c(\theta) = \frac{-\eta}{2k \sin^2 \frac{1}{2}\theta} \exp(-i\eta(\sin^2 \frac{1}{2}\theta) + 2i\sigma_0) \quad (\text{II-29})$$

For a spin 1/2 particle, the spin can couple in two ways with the angular momentum ℓ to give a total angular momentum $j = \ell + 1/2$ and the eigenvalues of which correspond to these two spin orientations are ℓ and $-(\ell + 1)$. Two scattering amplitudes result

$$A(\theta) = F_{\frac{1}{2} \frac{1}{2}} = F_c(\theta) + \frac{1}{k} \sum_{\ell} \exp(2i\sigma_{\ell}) \{ (\ell + 1) C_{\ell}^{\ell + \frac{1}{2}} + \ell C_{\ell}^{\ell - \frac{1}{2}} \}$$

$$\quad (\text{II-30})$$

$$\beta(\theta) = F_{\frac{1}{2} - \frac{1}{2}} = \frac{1}{k} \sum_{\ell} \exp(2i\sigma_{\ell}) \{ C_{\ell}^{\ell + \frac{1}{2}} - C_{\ell}^{\ell - \frac{1}{2}} \} P_{\ell} \cos(\theta) \quad (\text{II-31})$$

The cross section is given by

$$\sigma = |A(\theta)|^2 + |B(\theta)|^2 \quad (\text{II-32})$$

The boundary conditions require that the solution for the initial channel is of the form of Equation II-27 and

all other channels be outgoing waves

$$y_i = F_{\ell_i} + C_i^1(G_{\ell_i} + iF_{\ell_i}), \quad (\text{II-33})$$

$$y_F = C_F^1(G_{\ell_F} + iF_{\ell_F}) \quad (\text{II-34})$$

From these, the amplitudes can be found,

$$F_{\mu_F \sigma_F \mu_i \sigma_i}(\theta) = \frac{4\pi}{k_i} \{i^{\ell_i - \ell_F}\} \exp(i\sigma_{\ell_i} + i\sigma_{\ell_F})$$

$$* \langle \ell_i s_{\mu_i} \sigma_i | j_i m_i \rangle \langle j_i I_i m_i \mu_i | JM \rangle Y_{\ell_i \mu_i}(\hat{k}_i)$$

$$* \langle \ell_F s_{\mu_F} \sigma_F | j_F m_F \rangle \langle j_F I_F m_F \mu_F | JM \rangle \langle Y_{\ell_F \mu_F}(\hat{k}_F) \rangle \quad (\text{II-35})$$

where σ and μ are the projections of the spins of the projectile and target and i and F refer to the initial and final states. The cross section becomes

$$\frac{d\sigma(\theta)}{d\Omega} = \frac{1}{2s+1} \frac{1}{2I_i+1} \frac{k_F}{k_I} \sum |F_{\mu_F \sigma_F \mu_i \sigma_i}(\theta)|^2$$

The code ECIS [Ra74] uses a different method to achieve a solution. The ECIS method involves an iterative procedure to obtain a solution to the coupled differential equations as opposed to integration of the solutions. The usual method of solving coupled equations results in as many solutions as there are equations, although only one is needed. The ECIS method involves a search for this

solution by iteration. This method results in a reduction of computational time but has the disadvantage of larger storage requirements than the standard coupled channels methods. The ECIS method gives better results than DWBA codes after the first iteration, while the second iteration gives the same result as the standard coupled channels method. A complete description of the ECIS method is contained in reference [Ra72].

CHAPTER III

EXPERIMENTAL METHOD

Introduction

The measurement of elastic and inelastic proton scattering from the actinide nuclei presents various experimental problems. The major one is the spacing of the states in the ground state rotational band. The excitation energy of the first excited state (2^+) is roughly 45 keV for uranium and thorium. An energy resolution of about 15 keV is adequate to resolve the first excited state from the ground state, which permits accurate determination of the peak areas.

Since the Coulomb barrier for protons on uranium is about 13 MeV, particle energies sufficiently above this are required for strong nuclear as well as electric interaction. The 35 MeV proton beam from the MSU cyclotron is well suited to these studies as its energy is well above the Coulomb barrier and sufficient energy resolution is achievable. In fact, an energy resolution of 1.5 keV [No74] for 35 MeV protons has been obtained in test situations using the MSU cyclotron and the Enge split-pole

spectrograph [Sp67] by utilizing the technique of dispersion matching [Bl71]. The energy resolution in the focal plane depends on both the beam resolution and the position resolution of the particle detector. The beam resolution is enhanced with the dispersion matching so that the detector resolution becomes a significant problem. Detectors routinely used in the spectrograph focal plane have an optimum position resolution of about .25 mm which results in an energy resolution of less than 10 keV for 35 MeV protons. The target thickness can degrade the resolution further by a maximum of 5 keV for a 1 mg/cm^2 target. However, the expected data rates are high enough that thinner targets may be used.

Dispersion Matching

Dispersion matching [Co59] involves spatially dispersing the beam at the target so that the image contains information about the energy of the beam. The dispersion of the spectrograph is used to cancel the coherent energy spread of the beam. Effects which make the beam incoherent such as multiple scattering in the target cannot be cancelled, however.

Consider (Figure III-1) a point image at the focal plane with an energy spread equivalent to that of the beam. The high and low energy particles at this image

Figure III-1. Schematic illustration of Enge split-pole spectrograph and scattering chamber.

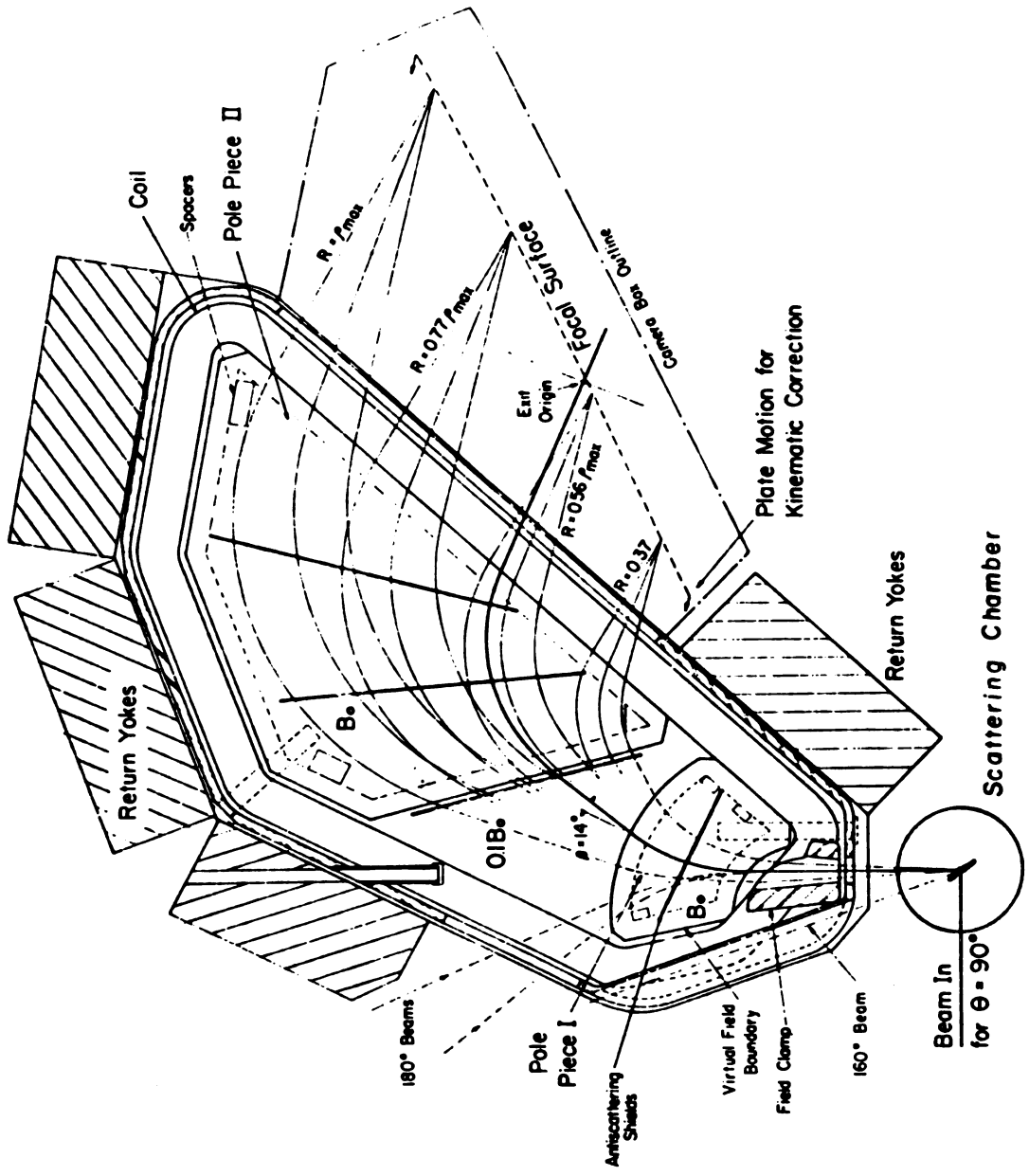


Figure III-1

must originate from different positions on the target. If the beam from the cyclotron is dispersed to match this dispersion by the spectrograph, the high and low energy particles in the beam at the target will arrive at the same position at the focal plane. The standard procedure is to adjust the focussing elements of the beam transport system, depicted in Figure III-2, to obtain an accurate image of BOX 5 at the target location. The production of an image at the target may be observed by the insertion of an object at the BOX 5 location and observing the resultant image on a scintillator at the target position. The beam at BOX 5 is dispersed by the analyzing magnets M3 and M4 so that the horizontal position at BOX 5 is dependent on the energy. It is possible to vary the energy spread of the beam at the target by adjusting the width of slits at BOX 5. A small energy spread may be obtained only with a substantial loss of beam current. Additional fine tuning of the beam transport system is done to obtain a narrow image of an elastic scattering line or the beam at the focal plane of the spectrograph. When the dispersion matching parameters are optimized it is possible to use the full beam intensity extracted from the cyclotron without any deterioration in energy resolution observed in the inelastic scattering spectrum in the spectrograph focal plane. Detectors used in part of this tuning procedure are discussed in Appendix A.

Figure III-2. Experimental layout showing the beam transport system used with the spectrograph.

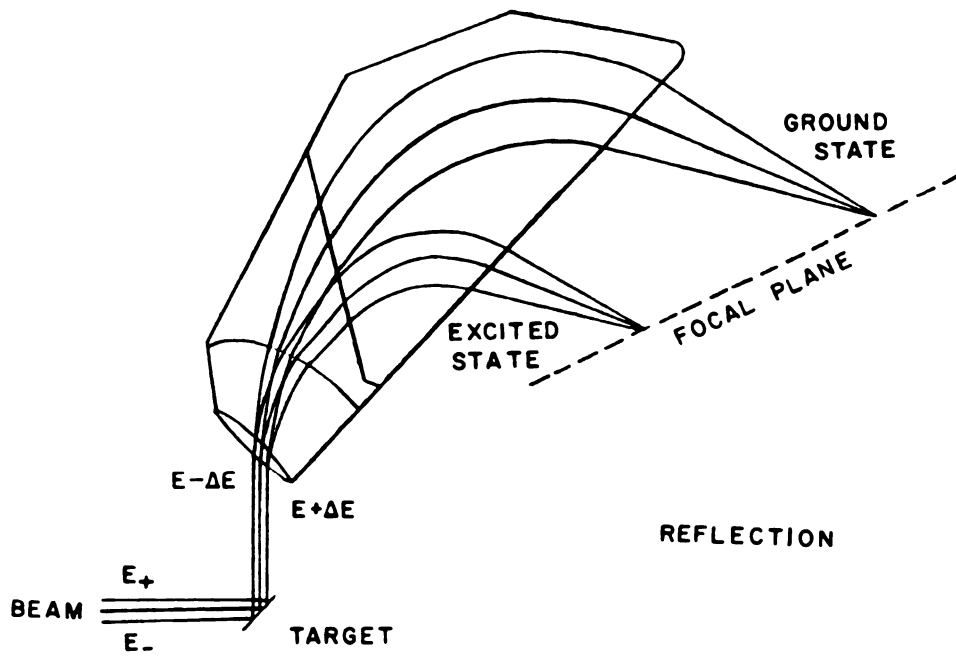
Different angular ranges of the data dictate different modes of dispersion matching. The standard procedure is to rotate the target such that the target angle relative to the normal to the beam is one half the scattering angle. Keeping the target angle at one half the scattering angle maintains constant effective dispersion over a range of scattering angles. Consider Figure III-3a for scattering at 90 degrees. The geometry used for forward angle scattering is the transmission mode where the scattered particles pass through the target. This mode has an advantage that the effects of the target thickness are minimized as the maximum total thickness seen by the incident and the scattered particle is equal to the target thickness. When the scattering angle is greater than 90 degrees, causing the target angle to exceed 45 degrees, the width of the beam spot may exceed the horizontal extent of the target material. When the target is not rotated, scattering to angles near 90 degrees cannot be done since the scattered particles are blocked by the target ladder assembly.

An alternative is to use a reflection mode as in Figure III-3b. In the reflection mode the particles entering the spectrograph come from the same side of the target as the beam is incident. This has two major difficulties, the first being that the maximum thickness seen by the incident and scattered particle is twice the thickness of the

Figure III-3. Illustration of the two modes used for dispersion matching. For forward angles ($\theta < 90^\circ$), the transmission geometry (a) is used. For back angles ($\theta > 90^\circ$), the reflection geometry (b) is used.

ENGE SPLIT-POLE SPECTROGRAPH

a)



b)

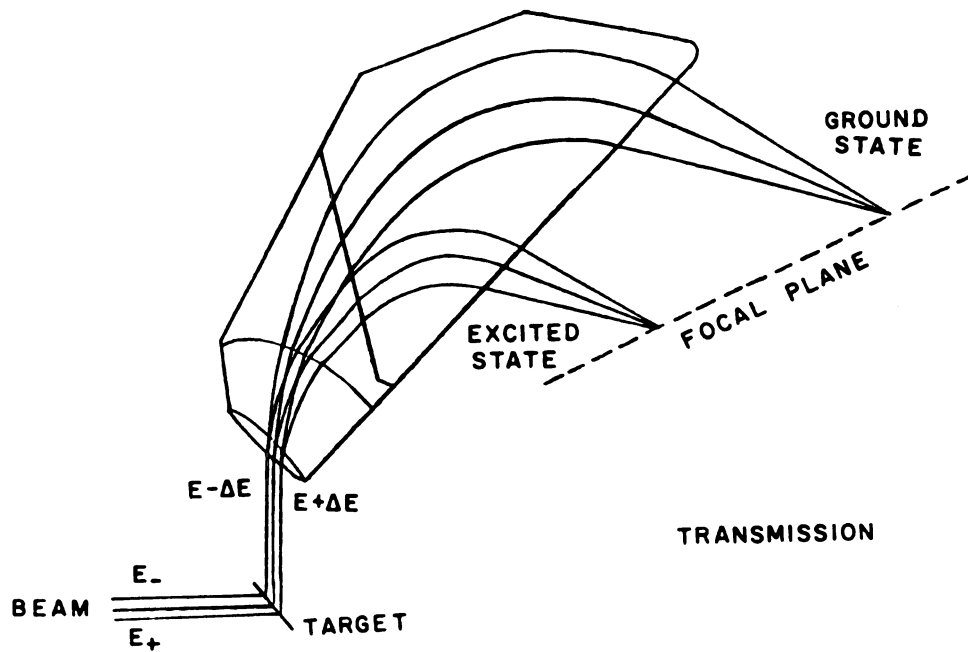


Figure III-3

target material. This is relatively minor when compared with the effects caused by the dispersion matching being wrong. The beam is dispersed such that the beam energy spread is now enhanced rather than cancelled. The spectrograph views the opposite side of the target where the energy spread is effectively reversed. To correct this, it is necessary to reverse the sign of the horizontal magnification of the beam between BOX 5 and the target. Beam optics calculations were done using TRANSPORT [Br74] to determine the correct beam-line settings. Two additional quadrupoles Q7' and Q8' placed near M5, as seen in Figure III-2, are required to produce a horizontal crossover prior to two of the existing quadrupoles, Q9 and Q10. The beam transport system prior to BOX 5 remains unchanged. The reflection mode produces a comparable image to the image produced by the no-crossover mode, with no loss of energy resolution. Figure III-4 shows spectra for protons scattered from a ^{176}Yb target [Me79] for the reflection and transmission mode and also for the target in reflection mode with the beam transport system setup for transmission mode.

Particle Detection

To take full advantage of the high quality beam, dispersion matching requires measuring the position of particles at the focal plane with a high degree of accuracy.

Figure III-4. Spectra resulting from 35 MeV protons scattered from a ^{176}Yb target for the two modes of dispersion matching; (a) transmission, (b) reflection, and (c) target rotated for reflection mode with the beam transport system set up for transmission mode. Figure III-4c represents the worst possible case where the beam energy spread is enhanced rather than cancelled.

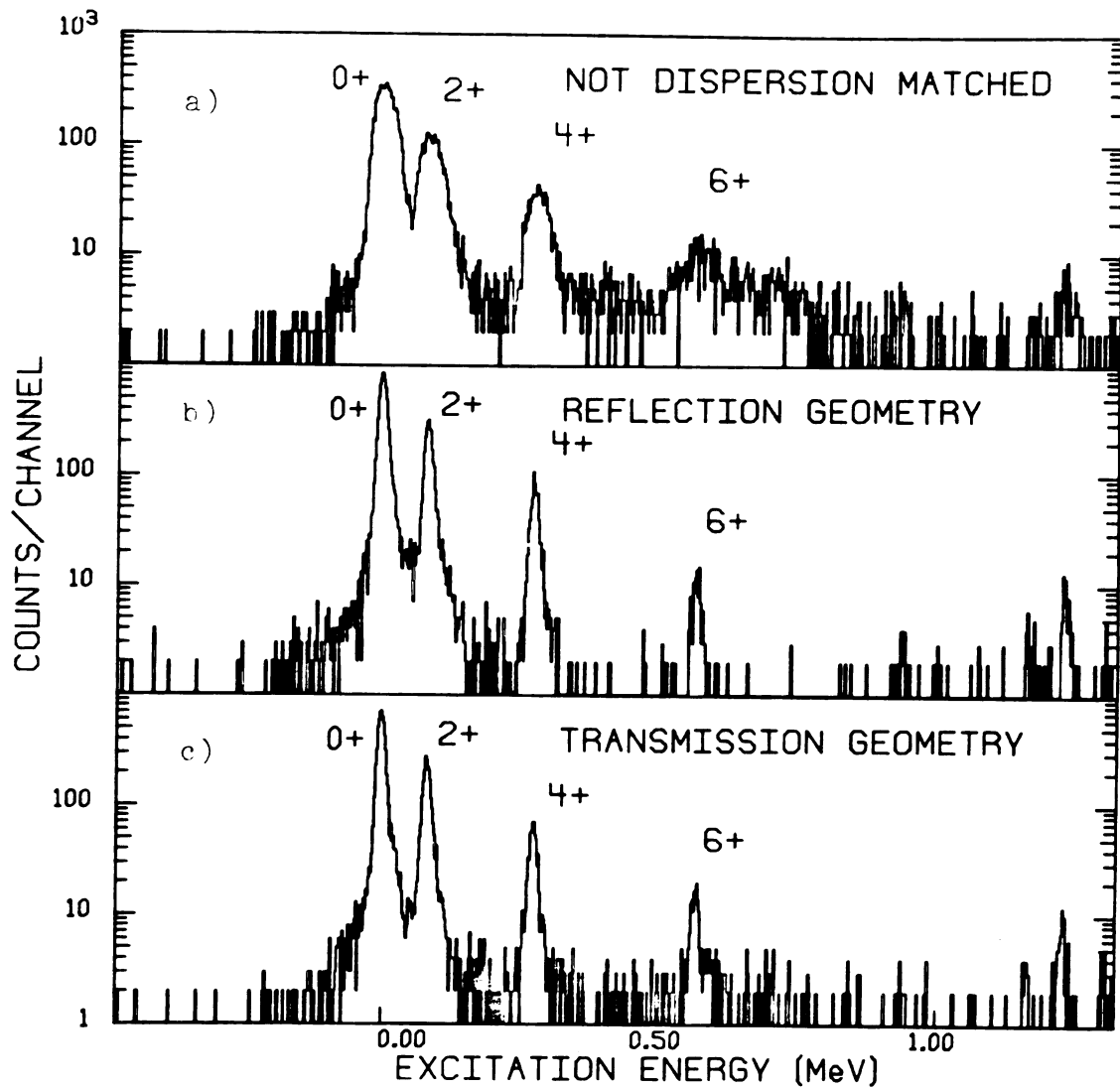
$^{176}\text{Yb} (p,p')$ $\theta = 90^\circ$ $E_p = 35.3 \text{ MeV}$ 

Figure III-4

Photographic emulsions in the focal plane have extremely good position resolution and linearity. However, in this experiment their usefulness is limited. The position of each track is measured directly. The tracks appear in an emulsion deposited on a glass plate and the position is found using a microscope and mechanical readout. The emulsion can become saturated with tracks from the particles, limiting the number of distinguishable events per unit area. High resolution enhances this effect as a particle line such as the elastic scattering line may have a total width of 100 μm . Track saturation prevents the acquisition of both strong and weak states on the same plate. To recover the data requires the scanning of the plates, which is time consuming and may be impossible for strong lines. Also, the use of plates prevents continuous monitoring of the experiment and the resolution cannot be checked or tuned without an additional detector.

The disadvantages of plates make a position sensitive detector with direct position readout useful. To observe both elastic and inelastic scattering where the excited states may have cross sections four orders of magnitude smaller than the cross section for elastic scattering, requires a position sensitive detector which has a much better dynamic range.

The detector used was the inclined cathode delay-line counter [Mk75]. This device utilizes a more sophisticated

readout scheme than the standard charge division proportional counter and is illustrated in Figures III-5 and III-6. A particle passing through the detector leaves a track of dissociated electrons. The electrons are collected and multiplied on the active wires. The guard wires are for field shaping only, having no appreciable gain. The avalanche at the active wires induces a signal on the cathode. The cathode is made position-sensitive by dividing it into sections and connecting the sections together using a tapped delay line. The cathode consists of stripes parallel to the particle trajectory (45 degrees from normal to the detector) to minimize the projection of the particle track onto the position readout.

By measuring the relative time delay between the particle passing through the detector and the signal emerging from the end of the delay line, the position is obtained. A method used to derive the position is to use the signal from one end to start a time to amplitude converter (TAC) and the signal from the other end, delayed in time by the total delay of the delay line, to stop the TAC.

The optimal resolution obtained is less than the tap spacing because of an interpolation property of the delay line readout. Although an event is localized on the anode wires, the charge induced on the cathode is over a region roughly equal to the cathode-anode spacing. The centroid of the induced charge carries accurate position information

Figure III-5. Schematic cross section of the inclined cathode delay-line counter. Labeled parts are: (A) window frames, (B) anode support, (C) separator foil, (D) anode wires-five active and 4 guards, (E) anode wire for ΔE counter, (F) pickup stripe board, (G) frame for delay line and board, and (H) delay line. From Reference [Mk75].

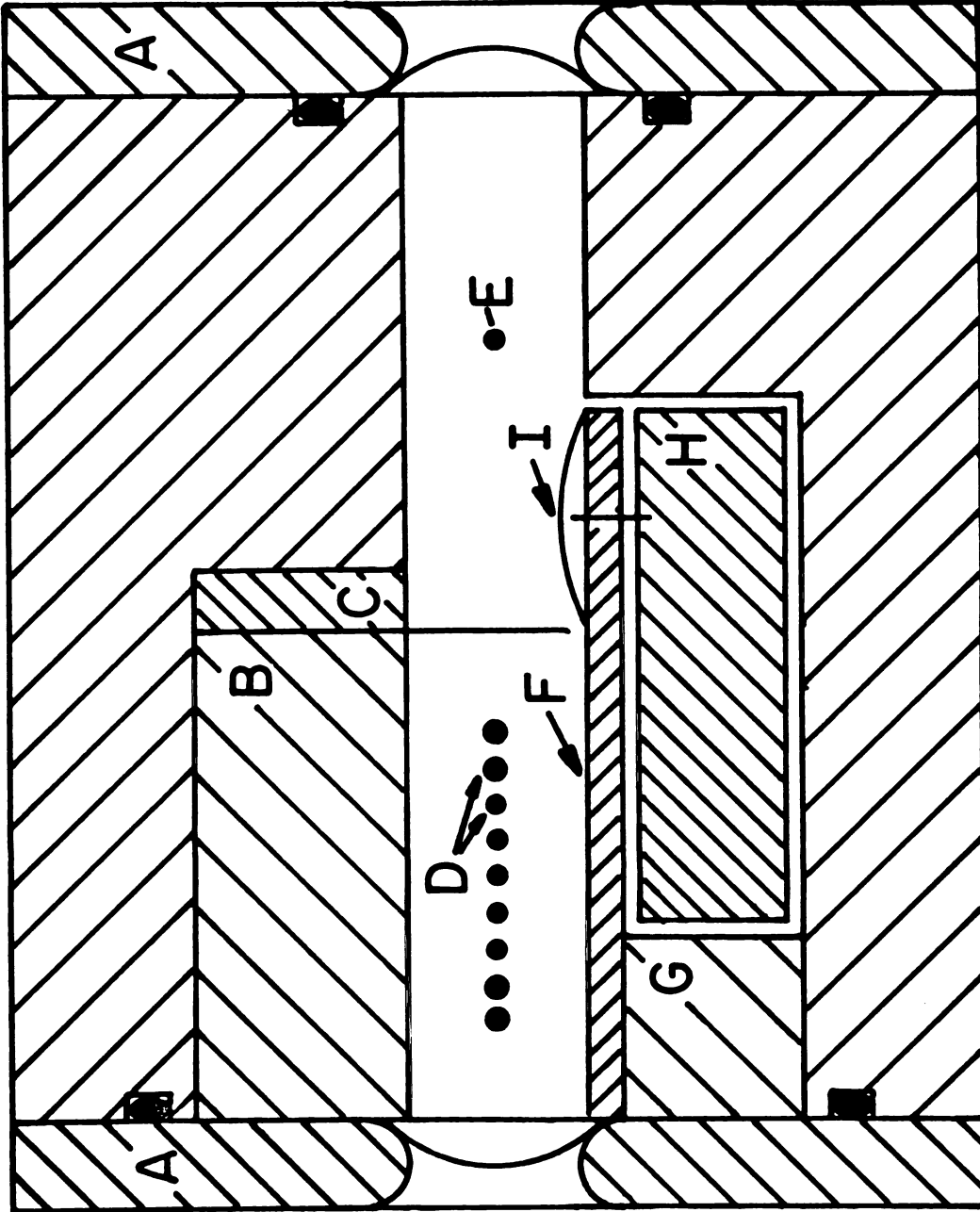
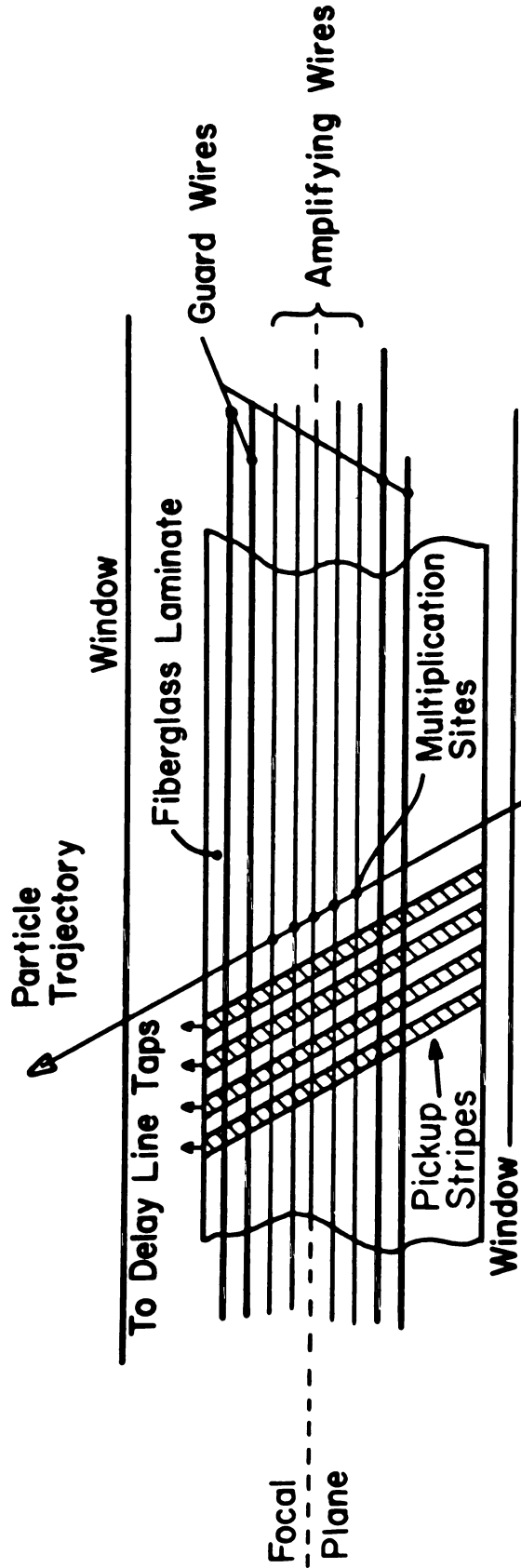


Figure III-5



SCHEMATIC (Plan View) OF COUNTER

Figure III-6. Schematic (plan view) of counter. From reference [Mk75].

and through suitable electronic shaping this information can be preserved.

In addition to the position from the delay line counter, a second proportional counter gives particle energy loss (ΔE) information. The counter is also backed with a plastic scintillator which yields timing information and particle energy. From the timing information, the time of flight of the particle through the spectrograph relative to the cyclotron RF is determined. This is possible because the beam from the cyclotron comes in bursts with the frequency of the cyclotron RF. A schematic of the electronic setup used is shown in Figure III-7. In order for an event to be valid it must satisfy E, ΔE and time-of-flight requirements. The requirements placed on each event are useful in rejecting unwanted particles and gamma-ray background events.

The counter electronics were modified from the original description. Signals were obtained from the active wires, and the delay line was terminated using pulse transformers [Bk76] and Radeka [Rd74] 'electronically cooled' preamplifiers, which eliminated the resistive delay-line termination and gave an increased signal to noise ratio. The signal from the active wires was used to determine the energy loss in the delay line portion of the counter. It has been found that the high and low energy tails on the peaks correspond to events with higher energy loss

Figure III-7. Schematic of electronics used to acquire the proton scattering data.

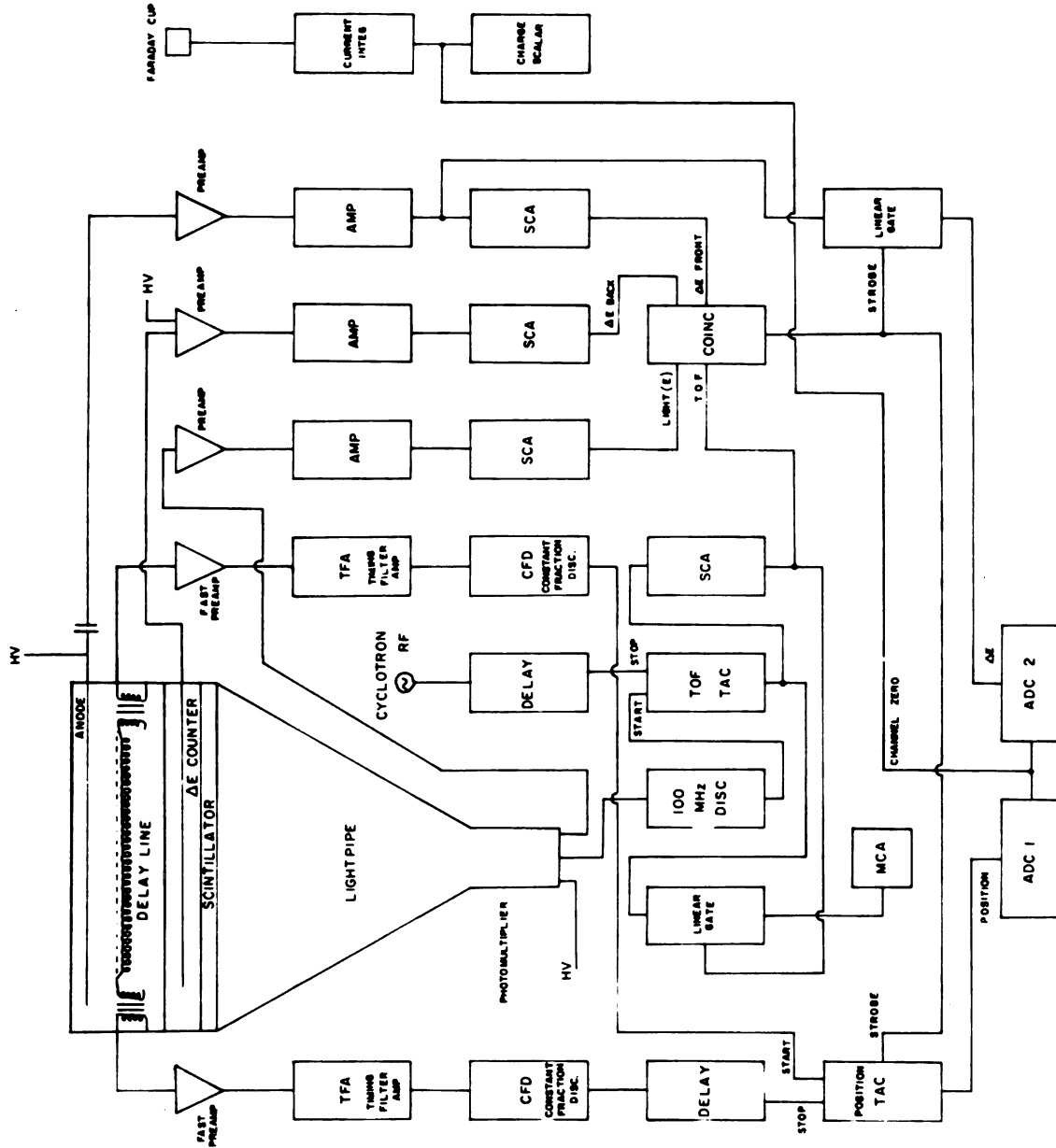


Figure III-7

in the counter. Two position spectra were recorded, one corresponding to the high energy loss in the front counter and the second containing all other valid events. The high ΔE band, called the wing band, was set to contain about 5 percent of the total events. Figure III-8 illustrates the results of the high energy loss selection. The gating has the effect of reducing the extent of the high and low energy tails, which simplifies the fitting of the data. The fitted peak areas were corrected by scaling the areas by a factor generated by determining the fraction of events in the wing band for each spectrum.

Target Thickness Monitor

A NaI(Tl) detector was installed in the scattering chamber at a scattering angle of 90 degrees to monitor the target thickness. Particles scattered from the nuclei in the target have different energies from those scattered from the nuclei of the backing material or contaminants, which are measured using the NaI(Tl) detector. The area of the peak corresponding to scattering from the target material is extracted and the effective target thickness calculated. The scattering data measured in the spectrograph are scaled relative to the effective thickness determined by the monitor detector.

Figure III-8. Comparison of wing and data (good) energy loss bands.

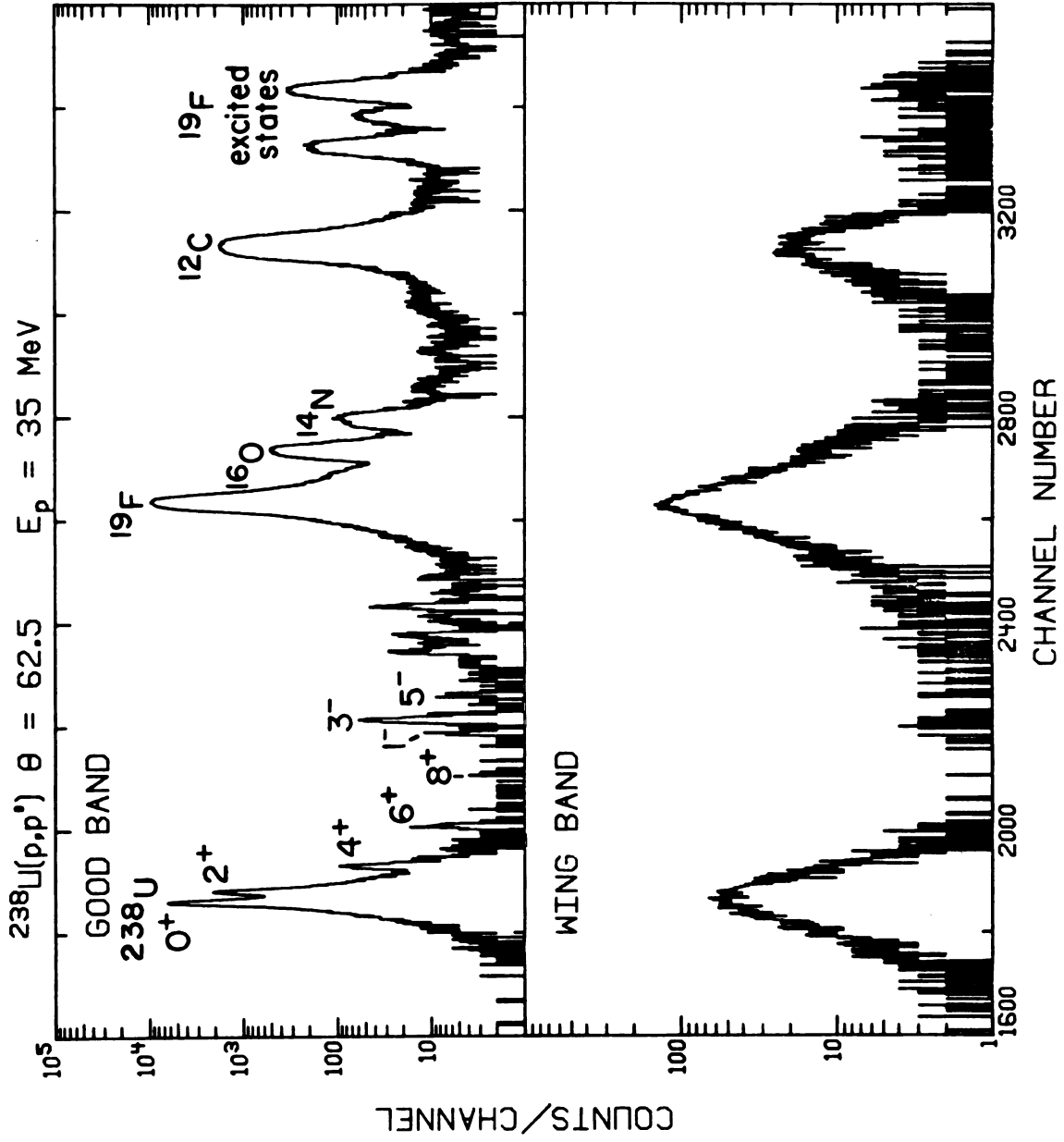


Figure III-8

Beam Current

The beam current was monitored using a water-cooled Faraday cup to stop the beam. A current integrator determined the charge collected at each scattering angle. The beam current was adjusted to maintain a maximum of three percent dead time for the position TAC or the computer ADC. The scattering data were deadtime-corrected by scaling the data by a factor equal to the current integrator output scaled in a scalar inhibited by the ADC busy signal divided by the output scaled in a free scaler. Typical beam currents ranged from 50 nA to 3 μ A. The lower currents were used at forward angles where high particle count rates would contribute to large dead times.

Targets

The target material is radioactive and in the case of ^{234}U and ^{236}U , quite difficult to obtain. The production and handling of radioactive targets must be done with care to prevent contamination of the target-making equipment or the experimental apparatus. The angular range of the data to be covered, where the elastic scattering cross section covers at least five orders of magnitude, requires that the target be sufficiently thick to keep the time required for acquiring the angular distribution

within reasonable limits. The need for relatively precise inelastic scattering data, where the strength of the 8^+ may be as much as four orders of magnitude less than the elastic sets a lower limit on the thickness of the target material. It has been shown [Wa73] that targets with thicknesses less than $400 \mu\text{g}/\text{cm}^2$ have little effect on the energy resolution for 35 MeV protons. Targets with a thickness in this range are also well suited to these experiments in allowing efficient use of the available beam current.

The effects of contaminants in the target are not as important for the actinide nuclei as for lighter nuclei due to the kinematic recoils of the nuclei in the target. The competing elastically scattered particles from contaminants have lower energies than the particles scattered from the target material being studied with the energy difference increasing with angle. Figure III-9 shows spectra of particles scattered from the ^{234}U target at a number of angles illustrating the kinematic shift of the contaminant peaks. A relatively straight forward way of identifying the contaminants is to display the raw data in this form and identify peaks which shift relative to the elastic as a function of scattering angle.

It is apparent that contaminants with small mass present less of a problem making it beneficial to use target backings and target making procedures which do

Figure III-9. Spectra for 35 MeV protons scattered from a ^{234}U target for a number of lab angles showing kinematic shift of target contaminant peaks.

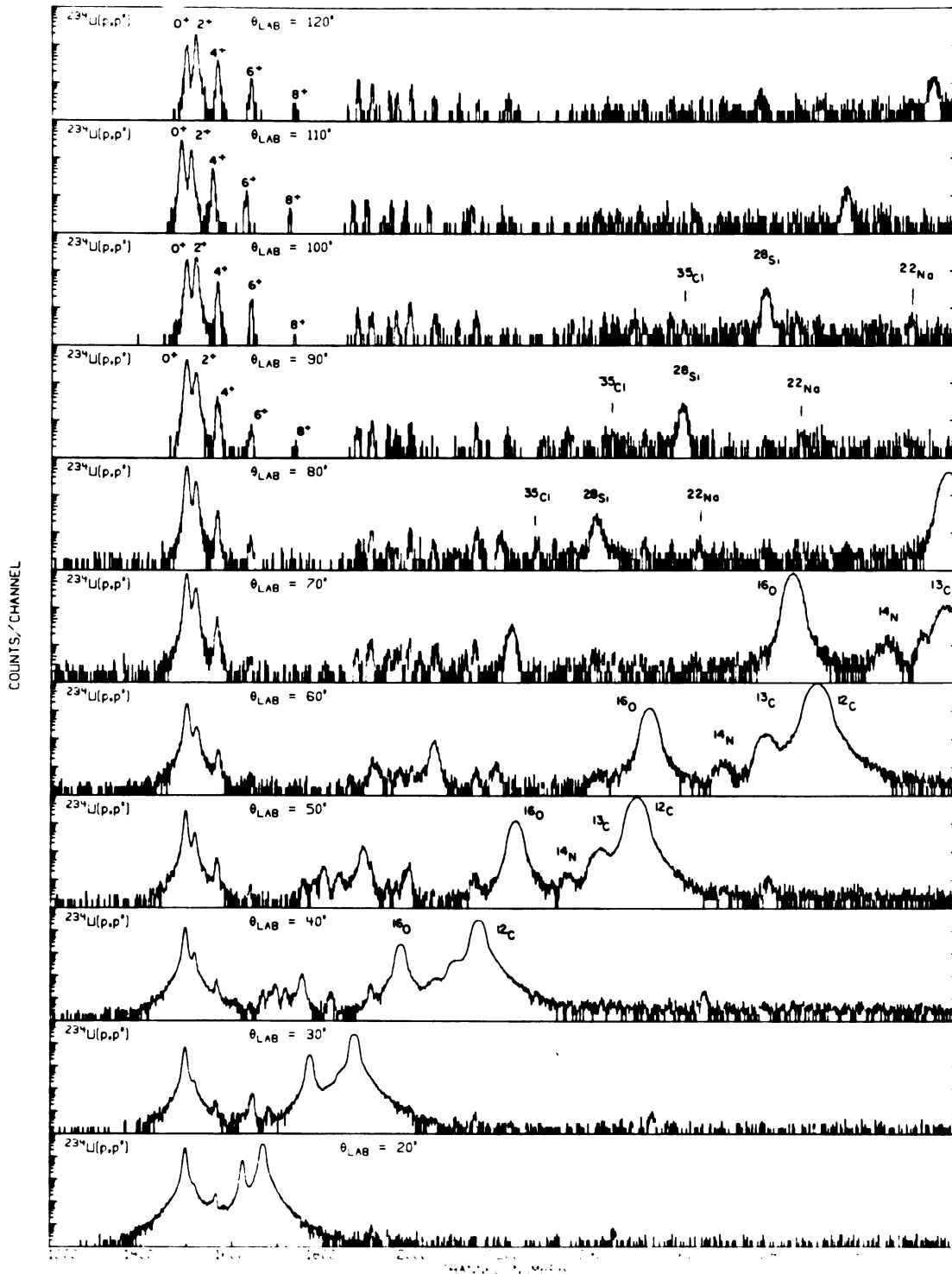


Figure III-9

not introduce heavy contaminants. Uranium and thorium metal are difficult to prepare into relatively thin ($<500 \mu\text{g}/\text{cm}^2$) self-supporting foils. An $800 \mu\text{g}/\text{cm}^2$ rolled thorium foil was used although it degraded resolution and contained a number of contaminants introduced by the rolling procedure. Since suitable self-supporting foils are not available carbon foils were chosen as the backing material to support the target material. A sputtering device [No78] was used to deposit uranium metal on carbon backings but yielded thin targets ($100 \mu\text{g}/\text{cm}^2$). The pure metal targets on carbon backings broke due to strains induced by the oxidation of the metal. The high melting temperatures of the pure metals make vacuum deposition of the pure metal difficult and may introduce undesired contaminants from the tungsten or tantalum boats required in the evaporation. The metals are also quite reactive, which quickly strains and breaks the backing foils. Natural uranium and thorium tetrafluorides are suitable target materials with relatively low melting points for clean vacuum deposition. The fluorine contamination is observed at only forward scattering angles. The targets produced were $250 \mu\text{g}/\text{cm}^2$ in thickness on $20 \mu\text{g}/\text{cm}^2$ carbon backings making them well suited to this experiment. Contaminants in the target include fluorine, carbon and oxygen.

The ^{234}U and ^{236}U targets were made [Be73] by depositing the material onto $40 \mu\text{g}/\text{cm}^2$ carbon backings using an

electromagnetic isotope separator. These targets are relatively free of contaminants, except those introduced by the backing foil and vacuum system. The observed contaminants include sodium, chlorine, and silicon, in addition to carbon and oxygen. However the thickness of the target material was only $30 \mu\text{g}/\text{cm}^2$ which severely limited the statistics. The targets were originally made for (α, α') Coulomb excitation studies where the $30 \mu\text{g}/\text{cm}^2$ is about the thickest that might be used. The thicker backings on these two targets were used to add strength to the target to avoid possible breakage and loss of the target material. The amount of target material on the backing was small so that extreme care was taken to prevent discrepancies in the measured scattering cross sections, introduced by the motion of the beam spot relative to the target material. The monitor spectra were fitted and the resultant effective target thicknesses used to correct the data except at forward angles ($\theta < 45$ degrees). At forward angles, cutting back the beam current produces a smaller beam spot, making the cross section less sensitive to beam spot motion.

CHAPTER IV

DATA REDUCTION

The position spectra were fit using an interactive peak fitting code SCOPEFIT [Dv78]. The code is used to fit the background, fit the peaks with an empirical peak shape, and sum the peak area in the background-subtracted data. The first order reference peak for fitting is generated by using the elastic scattering peak. The reference peak shape was then adjusted to obtain a best fit to the elastic peak and the inelastic states with which the elastic peak overlapped. A typical fit is shown in the Figure IV-1. The cross sections are calculated from the areas by using the standard relation

$$\frac{d\sigma}{d\Omega} = \frac{N \cdot 2.67 \cdot A \cdot \cos\phi_T}{d\Omega \rho Q} \frac{Q}{Q_{DT}} \quad \text{IV-1}$$

where N is the peak area,

A is the target atomic mass,

ϕ_T is the target angle,

Q is the charge in $\mu\text{Coulombs}$,

ρ is the target thickness in mg/cm^2 , and

Q_{DT} is the charge scaled with a scalar inhibited by the ADC-busy signal.

Figure IV-1. Spectra and fit line to the 0^+ , 2^+ , and 4^+ states of $^{238}\text{U}(p,p')$ at 57.5° .

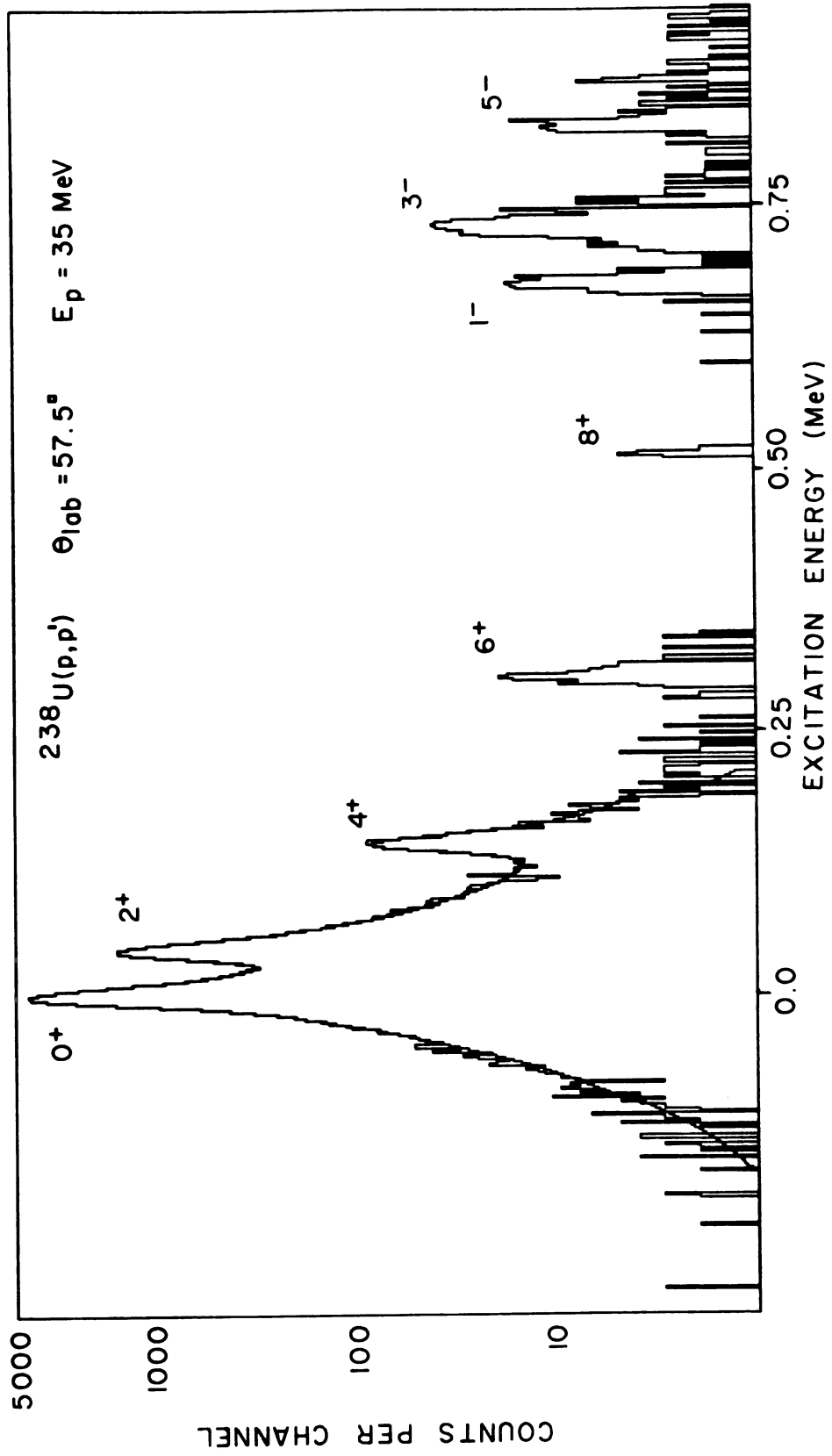


Figure IV-1

The solid angle $d\Omega$ is defined by the spectrograph acceptance aperture. A majority of the data was taken using a 0.69 msr ($1^\circ \times 2^\circ$) aperture. Data for $125^\circ < \theta < 144.5$ degrees for ^{234}U was taken using a 1.2 msr ($2^\circ \times 2^\circ$) aperture to speed data acquisition.

The data are scaled by a factor to correct for the number of counts in the "wing" band described above and for target thickness variations as determined by the monitor spectra. Typical corrections are 0-3% for the dead time, and 2-5% for the wing band. An uncertainty of 3 percent was folded quadratically with the statistical or fitting error to account for possible systematic errors in the normalization. Several targets of ^{232}Th and ^{238}U were used. The data were normalized by comparing common angular points. The overall absolute normalization was obtained by comparing the data to coupled channels calculations using Becchetti-Greenlees optical model parameters [Be69]. The normalization was reevaluated following preliminary searches on the optical model and deformation parameters. The forward angles ($\theta < 50^\circ$) only are used as these points are least sensitive to the model parameters. The scattering angles are checked from the spectra by taking advantage of the large kinematic shifts of the lighter mass impurity peaks for forward angles. This is important because the elastic cross section is a very strong function of the scattering angle at forward angles. The

initial deformation parameters were obtained from the Coulomb deformation parameters of Bemis [Be73] using 'BR scaling'. This scaling was accomplished by keeping $R_C\beta_C = R\beta$ where R_C and R are the Coulomb and volume term radii, respectively, and β_C and β are the Coulomb and volume term deformation parameters. The deformation parameters for the volume, imaginary, surface-imaginary, and spin-orbit are set equal. The volume, imaginary, and spin-orbit radii were fixed at the Becchetti-Greenlees optical model parameter values. The Coulomb radius and deformations (β_2, β_4) used were those of Bemis [Be73]. Because of the ambiguity involving the imaginary well depth and the diffuseness, the volume imaginary well depth was fixed at the Becchetti-Greenlees value of 5.0 MeV for a majority of the searches. The cross sectional data appears in tabular form in Appendix C.

In order to extract the deformation parameters for the nuclei being studied, the optical model parameters must be optimized by obtaining a best fit for the ground state data. The excited state cross sections are more sensitive to the deformation parameters, which are optimized for best fits to the inelastic scattering data. In addition to the quadrupole (β_2) and hexadecapole (β_4) deformation parameters, the hexakontattetarapole (β_6) deformation parameter were included. Figure IV-2 illustrates the sensitivity of the ^{238}U data to the inclusion of a non-zero β_6 deformation parameter in the calculation.

Figure IV-2. Calculated cross sections showing the best fits to the data with and without the β_6 parameter. The best fit for $\beta_6 = 0.0$ is calculated using the parameters of King et al. [Ki79].

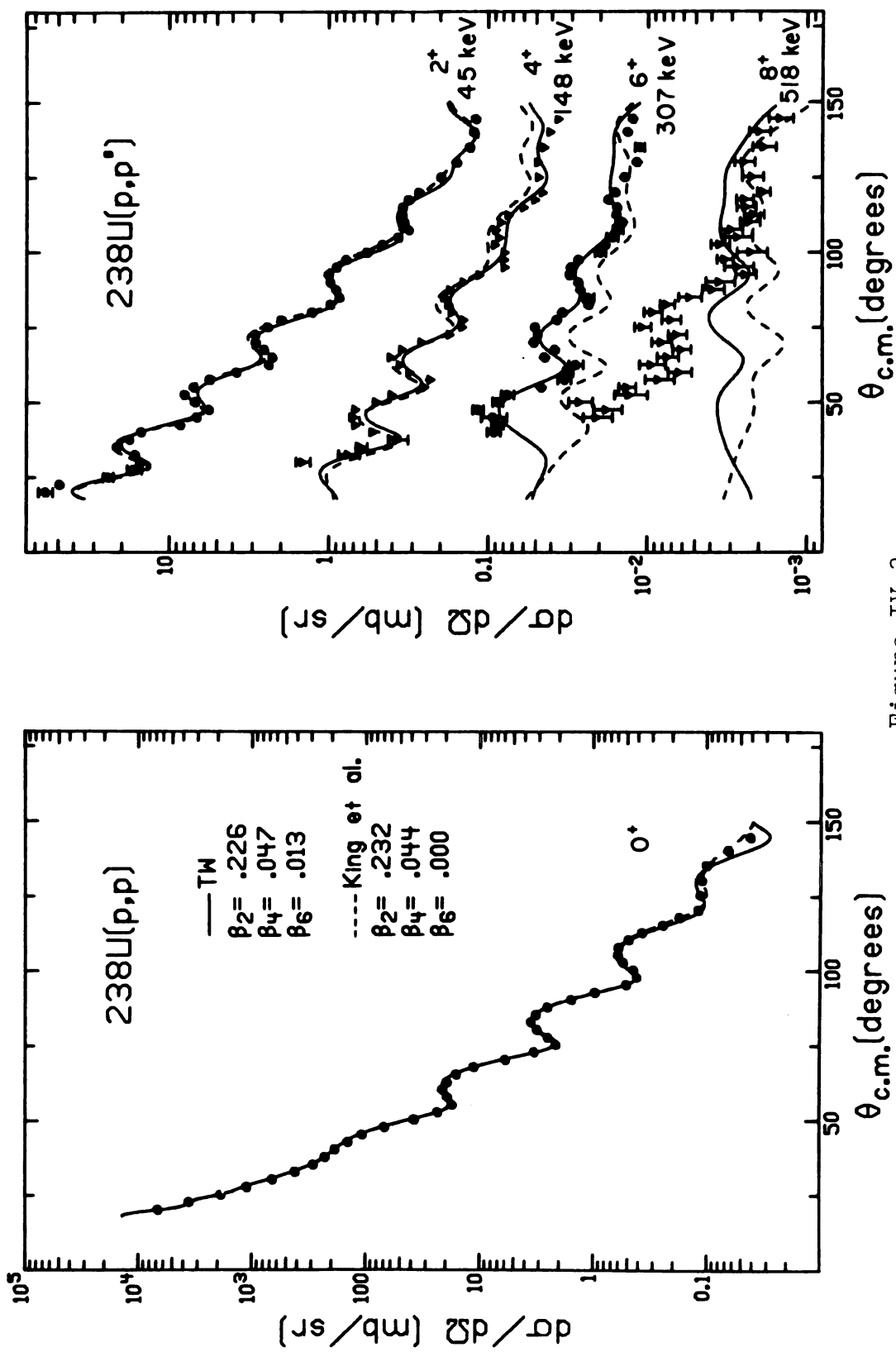


Figure IV-2

Optical Model Search

The angular distributions were fit using the Deformed Optical Model Potential (DOMP) in the coupled channels code ECIS [Ra74]. The parameters were adjusted using the automatic search option of the computer code. First parameters were searched on by preferentially weighting the state which is most sensitive to the parameters being searched on. For example, the elastic scattering cross section data were fitted by varying the optical model parameters V , W_D , V_{SO} , a and a_1 . The β_2 search was conducted with the 2^+ angular distribution weighted. For the optical model parameter and β_2 searches the calculation included couplings between the 0^+ , 2^+ and 4^+ states. The 6^+ state was included in the calculation when fitting the 4^+ angular distribution by varying β_4 .

 ^{238}U Analysis

The full calculation required to search on the β_6 parameter exceeded the available size of the data processor. Alternatives include scaling the experimental data or omitting portions of the potential such as the deformation of the spin-orbit potential. Scaling the experimental data can be done to account for the omitted 8^+ state. It was found that the inclusion of an additional state tended to

reduce the cross section in states with lower excitation energies in the rotational band. Figure IV-3 illustrates the effects of adding additional excited states in the coupled channels calculation.

The data was scaled using a 0-2-4-6-8 calculation and a 0-2-4-6 calculation for ^{238}U with all potentials deformed (these calculations were test calculations carried out on a larger computer at Daresbury) [Ro79]. The parameters used in the calculations are the best fit values for ^{238}U reported by King [Ki79] with $\beta_6 = 0.00$. The scaling factor consists of the ratio of the two calculations for the particular state and angle involved. Figure IV-4 shows the correction factors for the 0^+ through 6^+ states for the full range of angles. The scaling is largest for the 4^+ at back angles and the 6^+ state. The 0^+ and 2^+ states are changed by less than 1 percent throughout the angular range.

To test the scaling method, the cross sections from a 0-2-4-6-8 calculation with β_6 set to -0.02 were scaled using the above described technique. The resultant calculated 'data' was fit using 0-2-4 and 0-2-4-6 calculations with the values for β_2 , β_4 , and β_6 listed in Table IV-1. The same angular range as the actual data was used and the optical model parameters and deformation parameters not involved in the search were the same as used to generate the 'data'. The results show agreement with the starting deformation parameters. Thus by using the scaling

Figure IV-3. Illustration of the result of adding additional excited states to the coupled channels calculation.

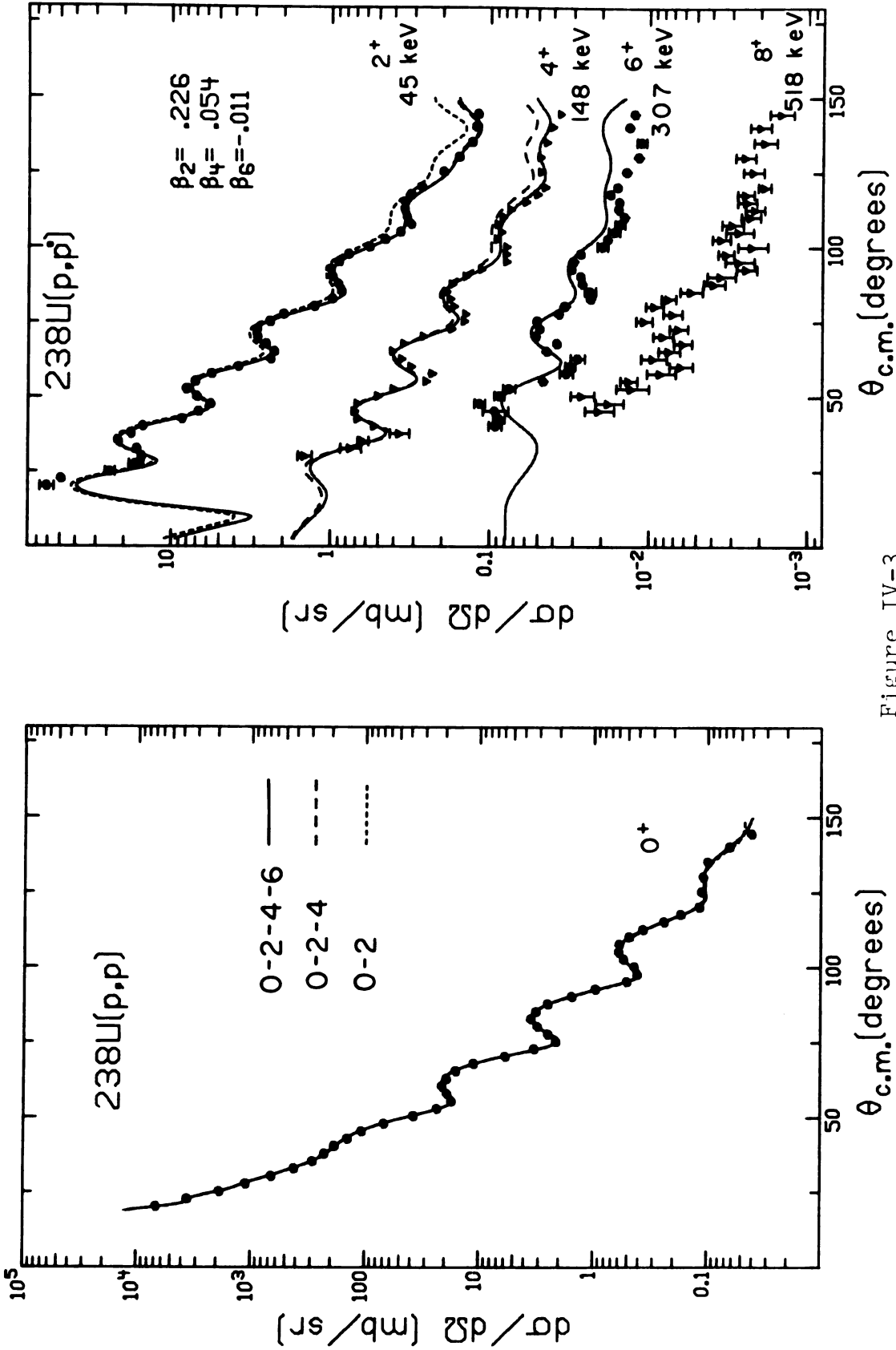


Figure IV-3

Figure IV-4. Illustration of the ratios of a 0-2-4-6 calculation to a 0-2-4-6-8 calculation for each state in ^{238}U . The ratios were used to scale the experimental data to compensate for the omission of the 8+ state in further calculations.

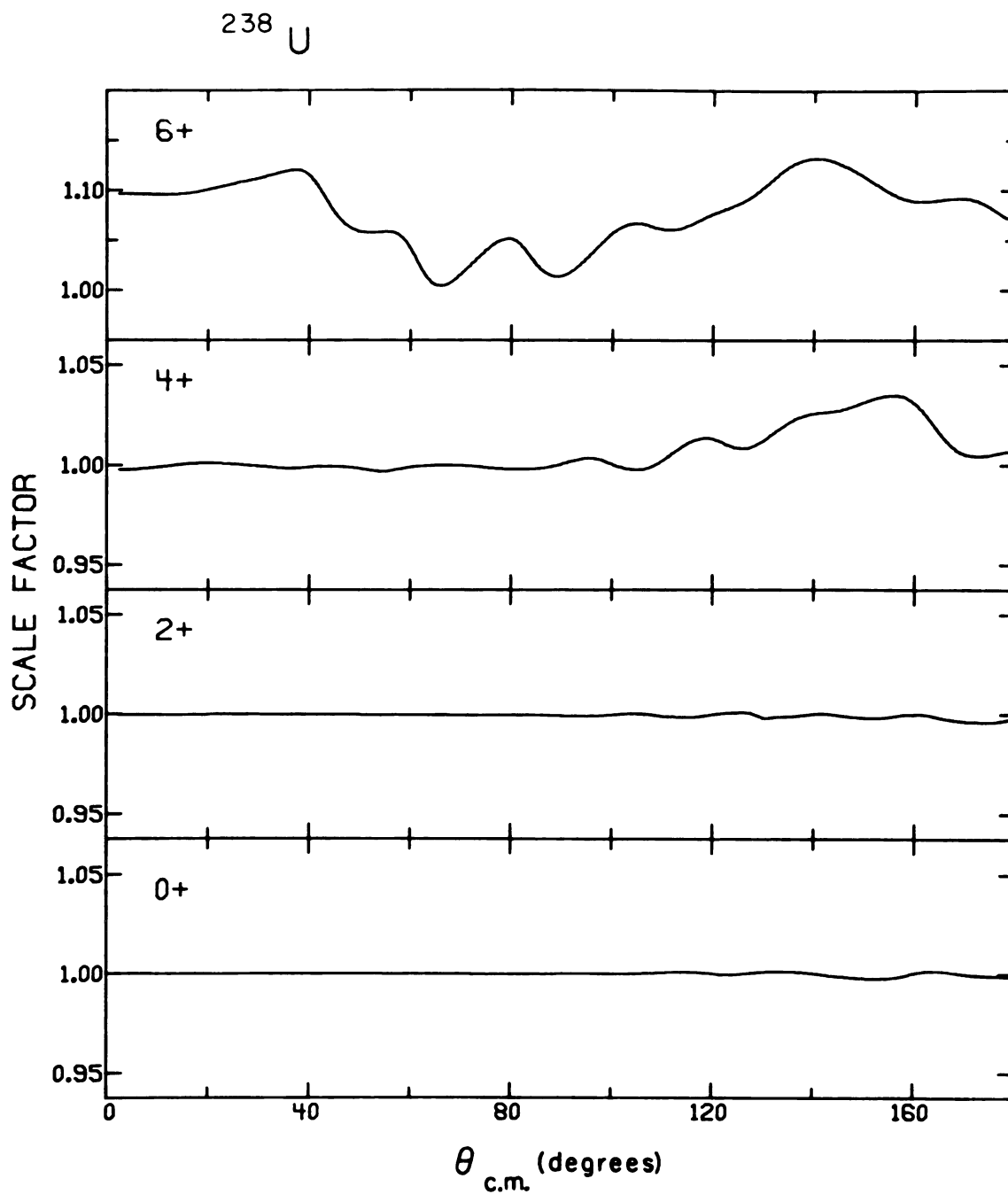


Figure IV-4

Table IV-1. Results of fitting scaled 'data' with DSO calculation and actual 'data' with SSO calculation. The 'data' are calculated values for ^{238}U using 0-2-4-6-8 couplings with deformed spin-orbit in a calculation using the parameters of King, et al. [Ki79].

RESULTS OF FIT

	DSO (scaled 'data')	SSO (actual 'data')
β_2 (expected)	0.2320	0.2320
β_2 min $\chi^2(0+)$	0.2320	0.2270
β_2 min $\chi^2(2+)$	0.2320	0.2310*
β_2 min $\chi^2(4+)$	<0.2000	0.2219
β_4 (expected)	0.0420	0.0420
β_4 min $\chi^2(0+)$	0.0420	0.0753
β_4 min $\chi^2(2+)$	0.0420	0.0245
β_4 min $\chi^2(4+)$	0.0410*	0.0396*
β_4 min $\chi^2(6+)$	0.0400	0.0390
β_4 min $\chi^2(8+)$	-----	0.0381
β_6 (expected)	-0.0200	-0.0200
β_6 min $\chi^2(0+)$	-0.0200	>0.0000
β_6 min $\chi^2(2+)$	-0.0206	>0.0000
β_6 min $\chi^2(4+)$	-0.0201	-0.0242
β_6 min $\chi^2(6+)$	-0.0180*	-0.0174*
β_6 min $\chi^2(8+)$	-----	-0.0175

* Indicates value which would be most significant.

approximation reliable deformation parameters may be extracted even though the actual calculation required to extract the deformation parameters is impossible to carry out.

The ^{238}U data were scaled and fitted using the deformed spin-orbit (DSO) calculations, including the 6^+ state. Searches on the well depths, the diffusenesses and the deformation parameters β_2 and β_4 were done separately using a DSO calculation until a χ^2 value convergence was obtained using the search procedure described above. The β_6 parameter was calculated by fitting the scaled 6^+ angular distribution. The data were then fitted by varying V , W_D , V_{SO} , a , a_1 , β_2 and β_4 simultaneously minimizing the total χ^2 value for the 0^+ , 2^+ , and 4^+ states with the actual data. The β_6 parameter was held fixed for this search procedure.

By including only a spherical spin orbit (SSO) interaction in the potential rather than the deformed spin-orbit (DSO) interaction, the magnitude of the calculation is greatly reduced. This makes the 0-2-4-6-8 calculation possible using the available computer, although the quality of the fit to the ground state data is reduced by using this method. To investigate the effects of the elimination of the spin orbit deformation, the calculated 'data' described above were fitted by varying the deformation parameters individually using the SSO calculation. The results are

listed in Table IV-1. There are deviations between the fitted deformation parameters and the initial deformation parameters but this method may still be viable for obtaining relatively accurate values for the deformation parameters with a considerable savings in computational time. The SSO fits were done without readjusting the optical model parameters which may account for some of the differences.

The spherical spin-orbit (SSO) calculation was used to fit the unscaled ^{238}U data by searching on the parameters V , W_D , V_{SO} , a , a_1 , β_2 , β_4 , and β_6 using a similar procedure described for the deformed spin orbit searches. The resultant best fit to the ground state yields χ^2 values which are a factor of 2-3 greater than the χ^2 values for the deformed spin orbit calculation. The excited state angular distributions could be fit with comparable χ^2 values. The best fit parameters and results from the spherical spin orbit calculations are compared to the results from the deformed spin orbit calculations in Table IV-2. Figure IV-5 contrasts the best fits to the data for the DSO and SSO calculations.

The search procedure used to obtain best fits to the data yielded results which require care in interpretation. Comparable fits could be obtained for continuous values of the product W and a_1 . This is of no great consequence, but a_1 has nearly the same effect on slope of the 0^+ and 2^+

Table IV-2. Best fit parameters resulting from fits to ^{238}U data with deformed spin orbit (DSO) and spherical spin orbit (SSO) calculations.

RESULTS OF FIT					
Parameter		DSO		SSO	
V	(MeV)	52.963	(190)	52.934	(340)
W	(MeV)	5.000		5.000	
W_D	(MeV)	4.477	(220)	4.021	(430)
V_{SO}	(MeV)	6.756	(170)	6.603	(245)
a	(fm)	0.756	(11)	0.718	(26)
a_i	(fm)	0.807	(19)	0.842	(31)
a_{SO}	(fm)	0.750		0.750	
r	(fm)	1.170		1.170	
r_i	(fm)	1.320		1.320	
r_{SO}	(fm)	1.010		1.010	
β_2		0.226	(1)	0.226	(2)
β_4		0.052	(1)	0.047	(2)
β_6		-0.011	(1)	-0.013	(1)

Figure IV-5. Comparison of the best fits to ^{238}U using the deformed spin orbit (DSO) and spherical spin orbit (SSO) calculations.

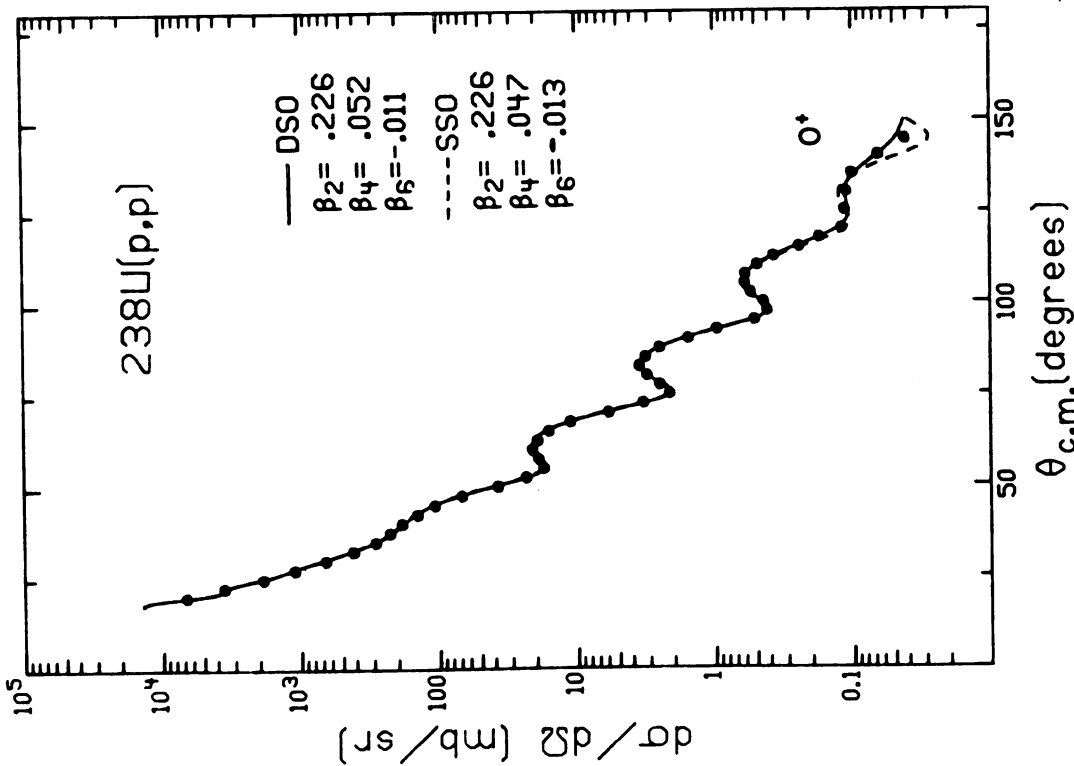
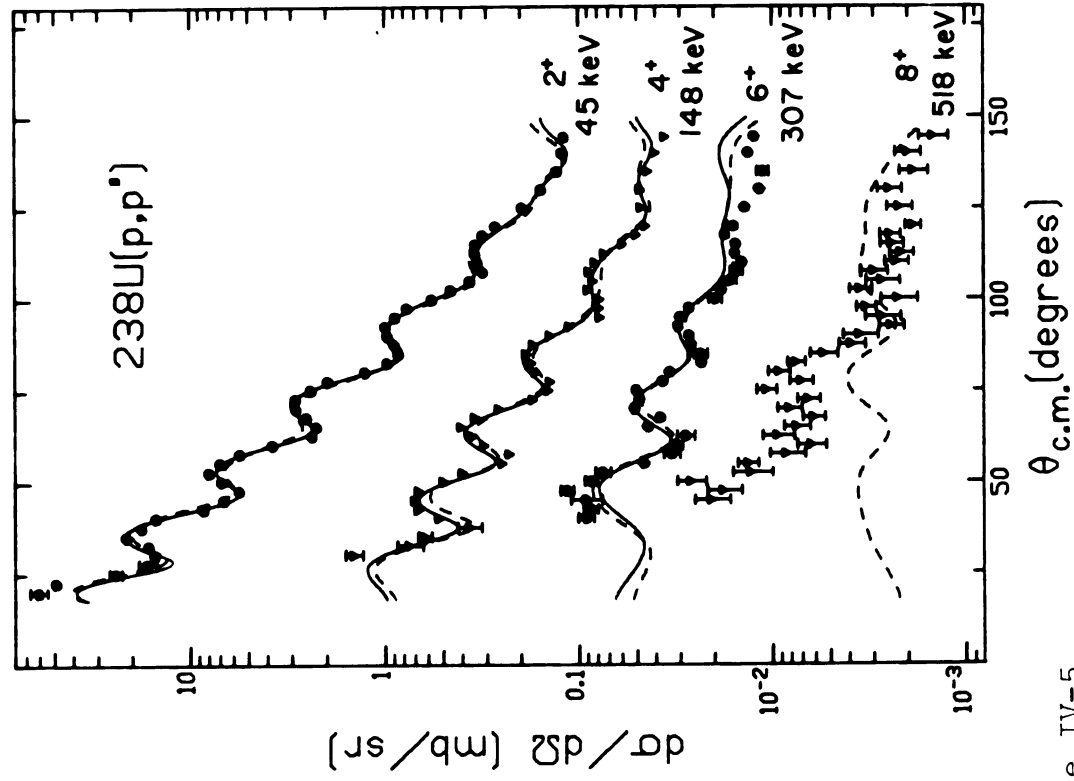


Figure IV-5

data as does the β_2 deformation parameter, so that erroneous results for β_2 could be obtained by allowing a to deviate continuously and compensating with β_2 . For the searches W was fixed at the Becchetti-Greenlees value of 5.0 MeV and a_1 allowed to vary.

Limiting the number of states included in the coupled channels calculations had some adverse effects on the fitting of the data. It was observed that improved fits to the ground state (0^+) resulted in a worsened fit to the first excited state (2^+) for the optical model parameter searches. The results of the β_2 search would give a smaller χ^2 for the 2^+ data, while increasing the χ^2 for the 0^+ angular distribution. The searches were repeated a number of times using the results of the previous calculation as the starting parameters for the search. The β_2 parameter oscillated about a value which is nearly equal to the final parameter obtained. The optical model parameters also oscillated in value to compensate for the β_2 values. The value of β_4 was not as subject to change as the β_2 parameter, showing no oscillatory tendencies. Table IV-3 lists values of the parameters and chi square values resulting from two search sequences, showing the results of the fits for two extreme values of β_2 . A phenomenon to note is that the higher values of β_2 yield higher χ^2 values for the 4^+ angular distribution, whereas the lower values result in a decreased χ^2 value for the 4^+ data. Figure IV-6 shows the

Table IV-3. Values of optical model parameters, deformation parameters, chi square values and moments corresponding to the extreme values of β_2 .

Parameter		^{238}U		^{232}Th	
V	(MeV)	53.599	53.686	52.671	53.276
W_D	(MeV)	4.036	4.050	5.193	4.753
V_{SO}	(MeV)	6.605	6.991	5.830	6.213
a	(fm)	0.749	0.754	0.723	0.725
a_1	(fm)	0.811	0.795	0.797	0.791
β_2		0.224	0.233	0.206	0.212
β_4		0.052	0.052	0.067	0.067
β_6		-0.011	-0.011	0.009	0.009
$\chi^2(0+)$		72.	75.	103.	106.
$\chi^2(2+)$		261.	291.	246.	246.
$\chi^2(4+)$		380.	1862.	560.	1782.
q_2	(eb)	3.215	3.346	2.872	2.261
q_4	(eb)	0.860	0.893	0.972	0.994
q_6	(eb)	0.097	0.107	0.298	0.309

Figure IV-6. The χ^2 values for the 0^+ , 2^+ , and 4^+ angular distribution data for two ranges of β_2 with corresponding optical model parameters.

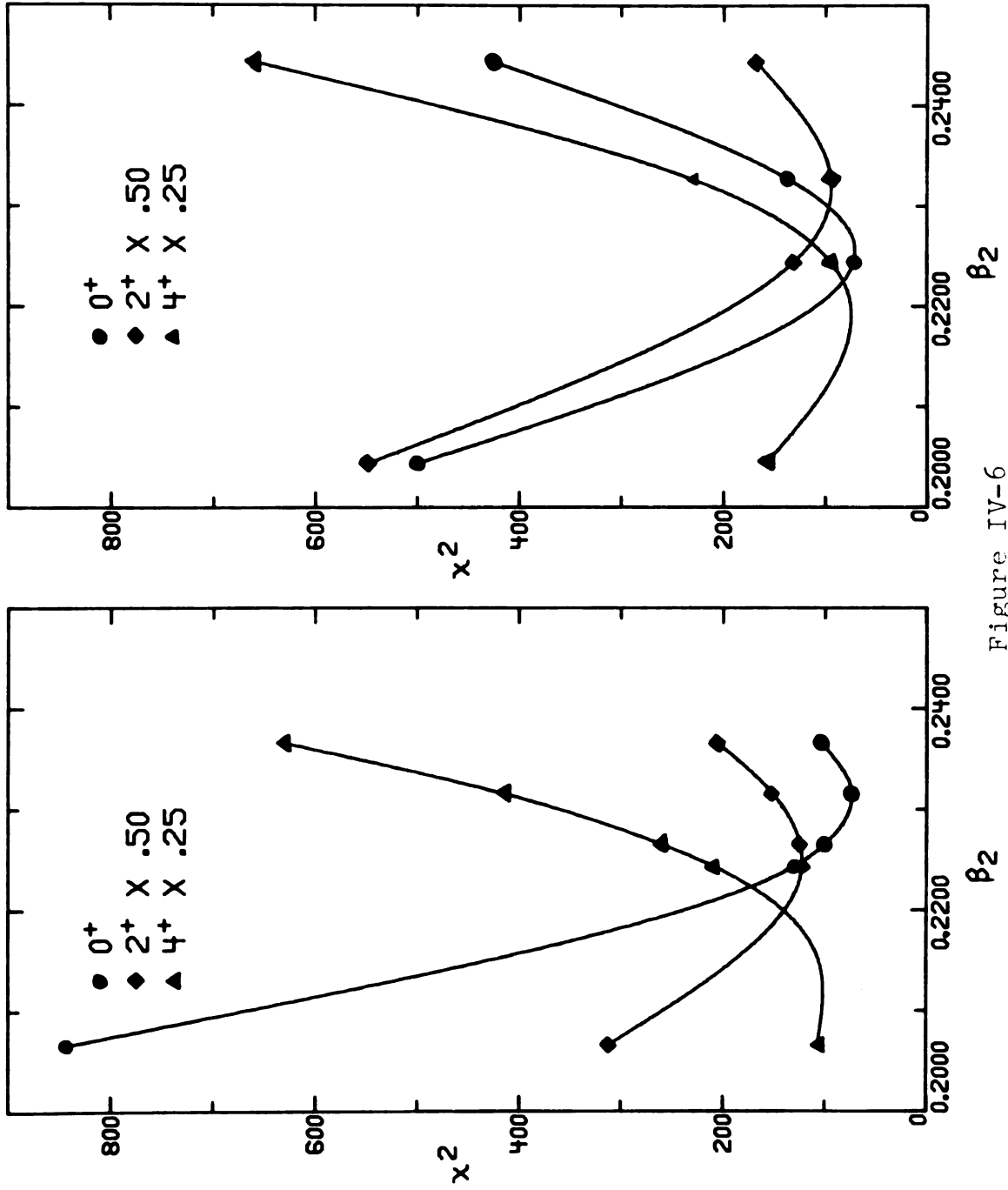


Figure IV-6

χ^2 values as a function of β_2 for the 0^+ , 2^+ , and 4^+ angular distributions for the 2 different β_2 searches. Since the parameters are correlated, the results of the search procedure is the production of a series of values for the optical model and deformation parameter, β_2 which yield good fits to the 0^+ and 2^+ angular distributions. Figure IV-7 illustrates two fits to the data with β_2 values which differ by about 4 percent. The optical model parameters for each β_2 are different which indicates that the other parameters in the optical model compensate for a change in a particular parameter. This discrepancy in the moment may be the result of the fitting procedure rather than inaccuracies in the measurement. Since there is considerable interplay between the parameters, the inclusion of the 6^+ state into the calculation and the simultaneous search on a number of parameters yields an unique value for β_2 with errors much smaller than 4 percent.

^{232}Th Data Reduction

The data were fit using a deformed spin orbit calculation with both scaled and unscaled data. The unscaled data were fit with the optical model parameters V , W_D , V_{SO} , a and a_1 and the deformation parameters β_2 and β_4 varied with the same method as was used for the ^{238}U data. In order to search on the β_6 parameter, and use the full

Figure IV-7. Illustration of the fit to the data resulting from the use of the β_2 parameter which yields a minimum χ^2 value for the 2+ data in Figure IV-6.

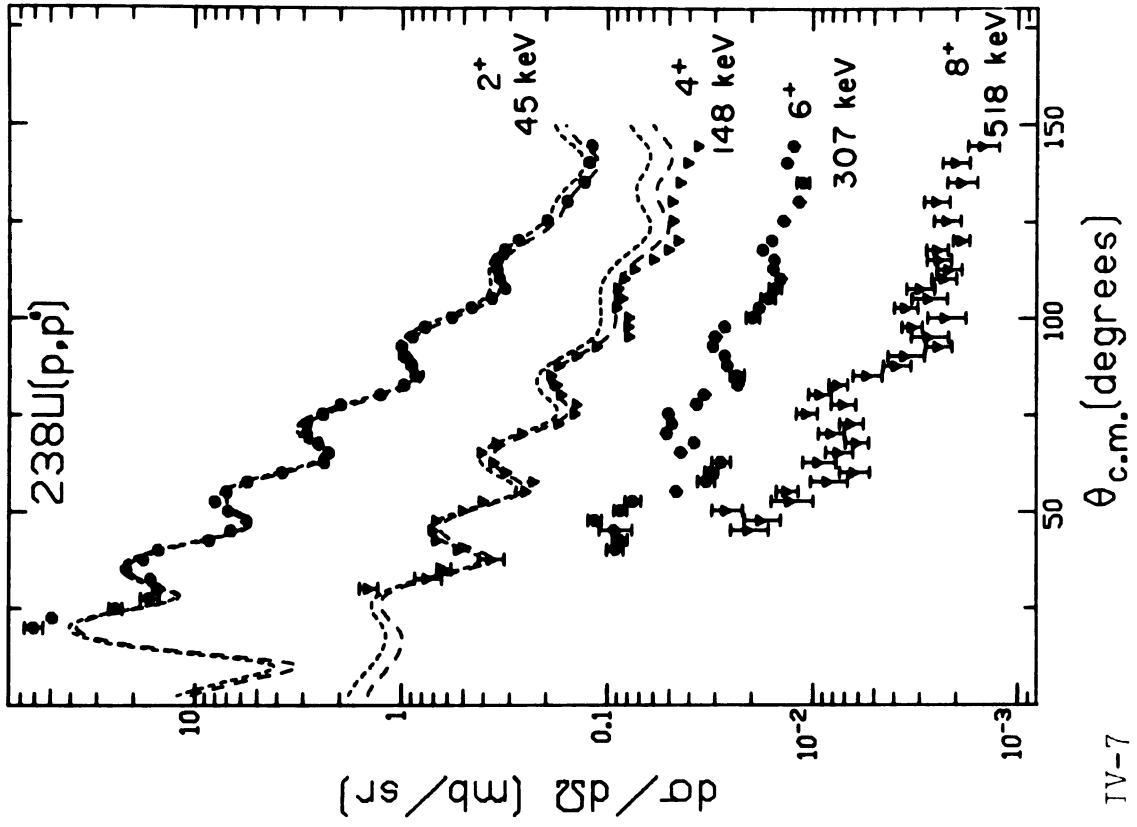
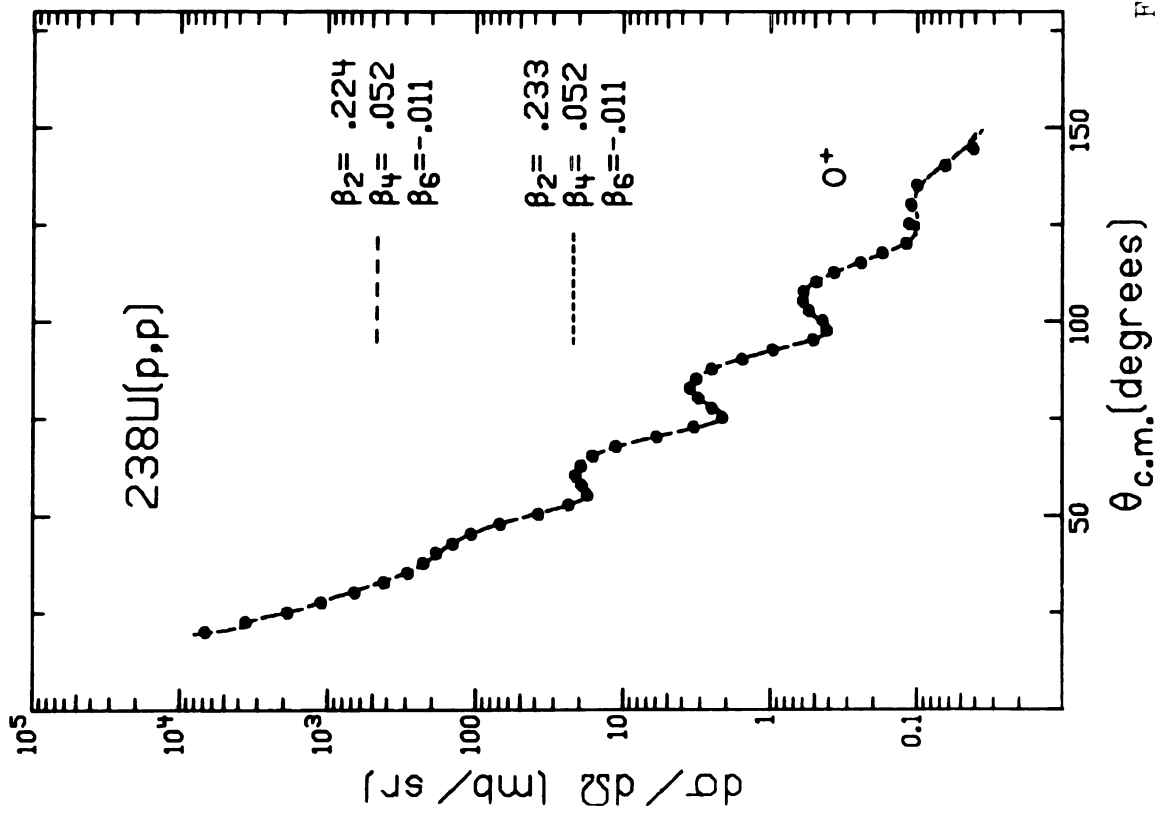


Figure IV-7

deformed potential, the data were scaled. The scaling is the same as done for ^{238}U except that ^{232}Th test calculations done at Daresbury [Ro79] were used. Figure IV-8 shows the correction factors as a function of angle for the four states included in the calculation. The fitting to the scaled data was done with the imaginary volume well depth set equal to 5.0 MeV. The value of this parameter was previously searched upon with it showing little change from the 5.0 MeV value predicted by Becchetti-Greenlees calculations. This data also shows a tendency for the β_2 value to oscillate. The variation was about 4 percent of the value of β_2 . An improvement to the χ^2 value for the 2^+ data with an increase in the χ^2 values for the 0^+ and 4^+ data is evident for larger values of β_2 . Table IV-3 contains sets of parameters resulting from the β_2 search. Figure IV-9 displays the χ^2 values for the 0^+ , 2^+ , and 4^+ states resulting from β_2 searches about the extreme values in the oscillation. Figure IV-10 shows the different fits for the different deformation parameters. A calculation of the quadrupole moment shows a variation of about 5 percent. The oscillation may be in part due to the effect of not including the 6^+ state in the calculation when searching on the β_2 parameter. The inclusion of this state changes the fit to the 4^+ angular distribution quite dramatically. The case of the higher β_2 value which yields a larger χ^2 value for the 4^+ angular distribution will be improved as the effect of the

Figure IV-8. Illustration of the ratio of a 0-2-4-6 calculation to a 0-2-4-6-8 calculation for each state in ^{232}Th . The ratios were used to scale the experimental data to compensate for the omission of the 8+ state in further calculations.

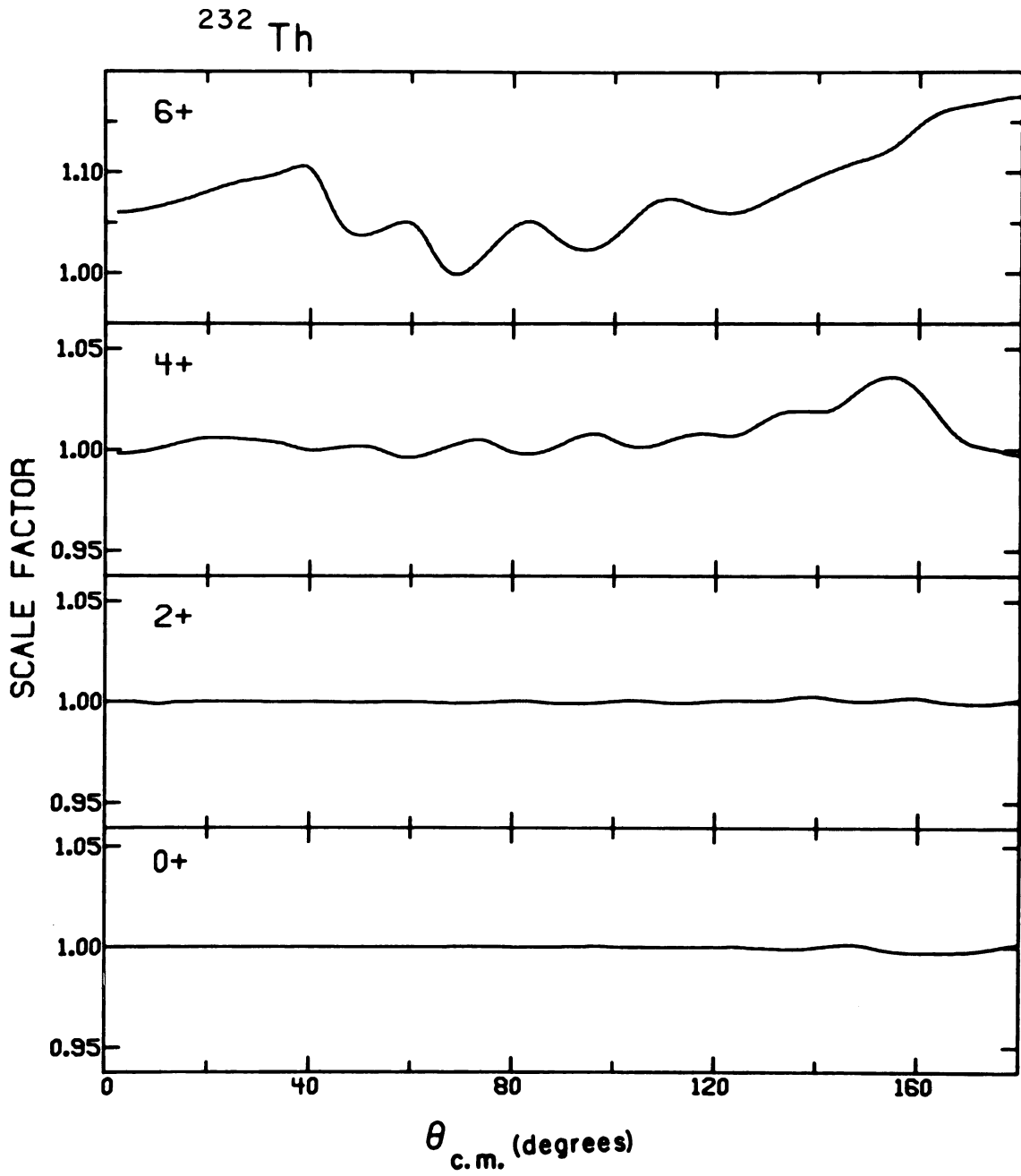


Figure IV-8

Figure IV-9. The χ^2 values for a 0^+ , 2^+ , and 4^+ angular distribution data for two ranges of β_2 with corresponding optical model parameters.

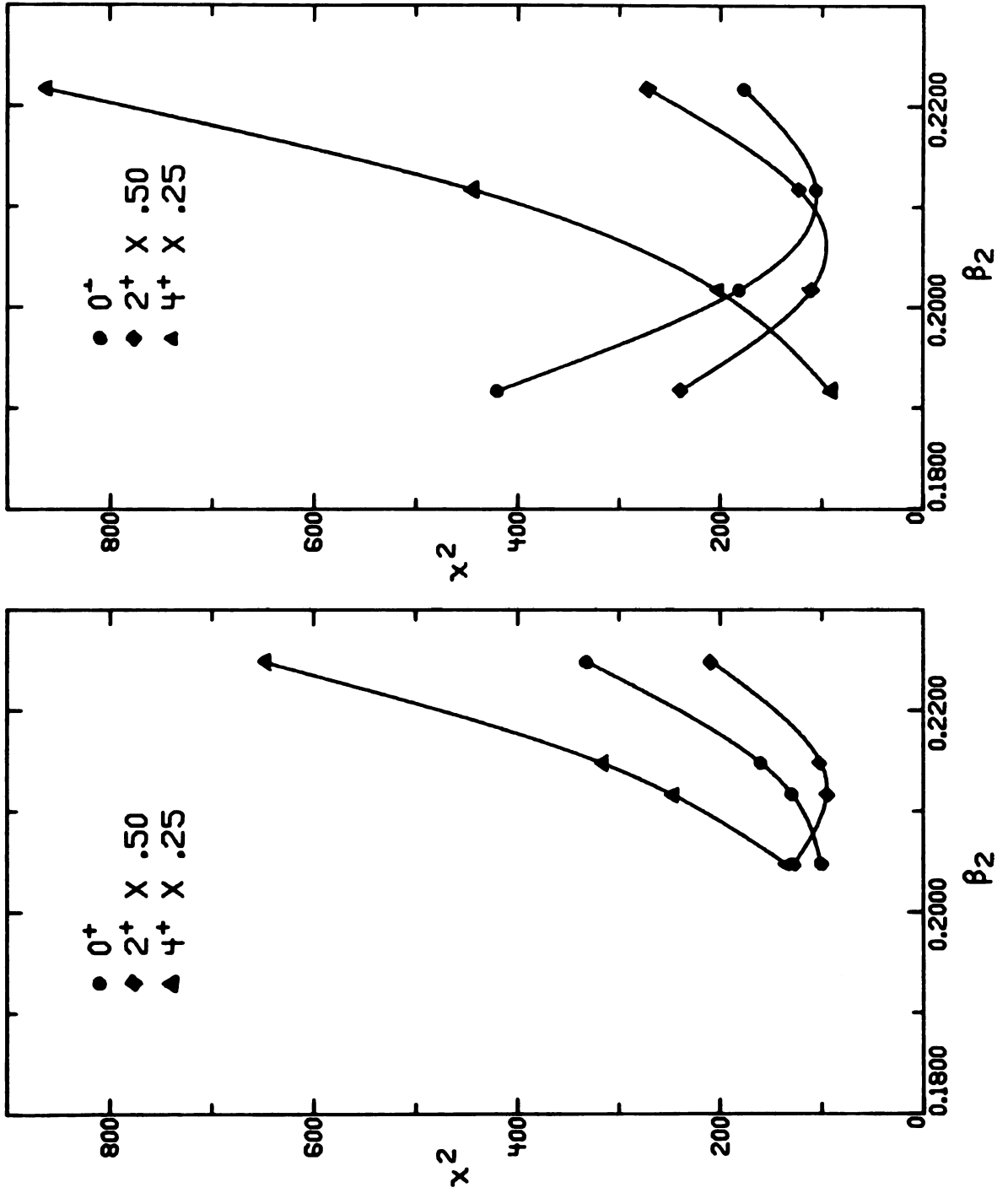


Figure IV-9

Figure IV-10. Illustration of the fit to the data resulting from the use of the β_2 parameter which yields a minimum χ^2 value for the 2^+ data in Figure IV-9.

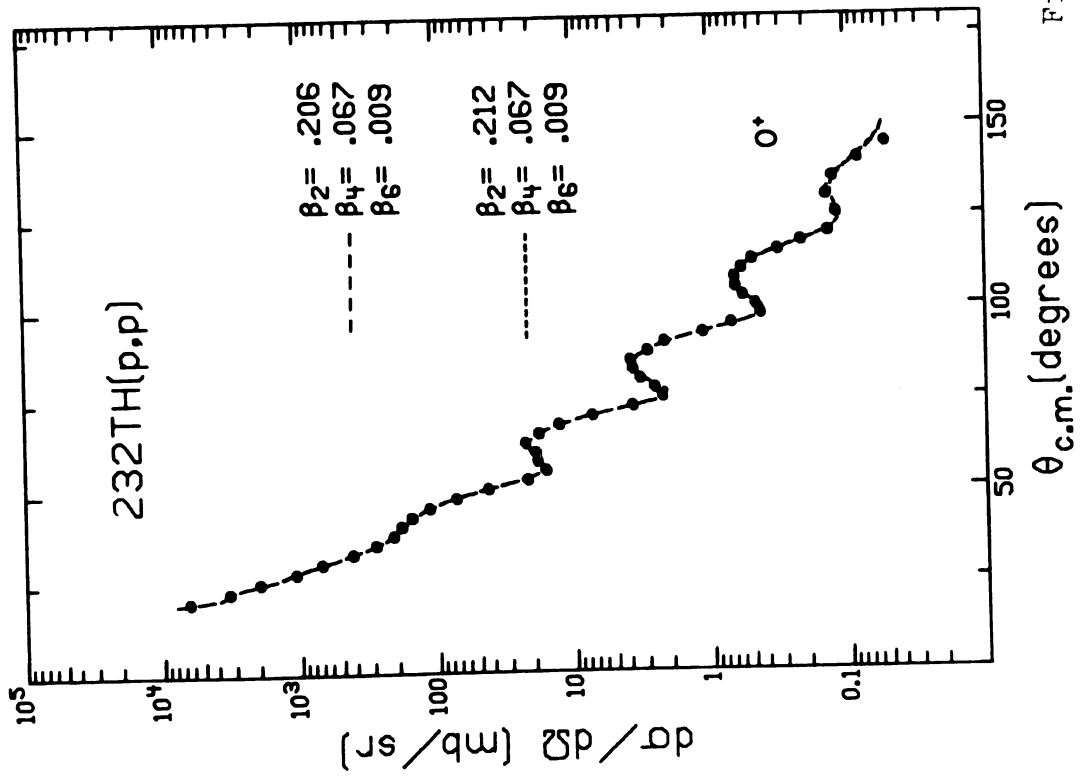
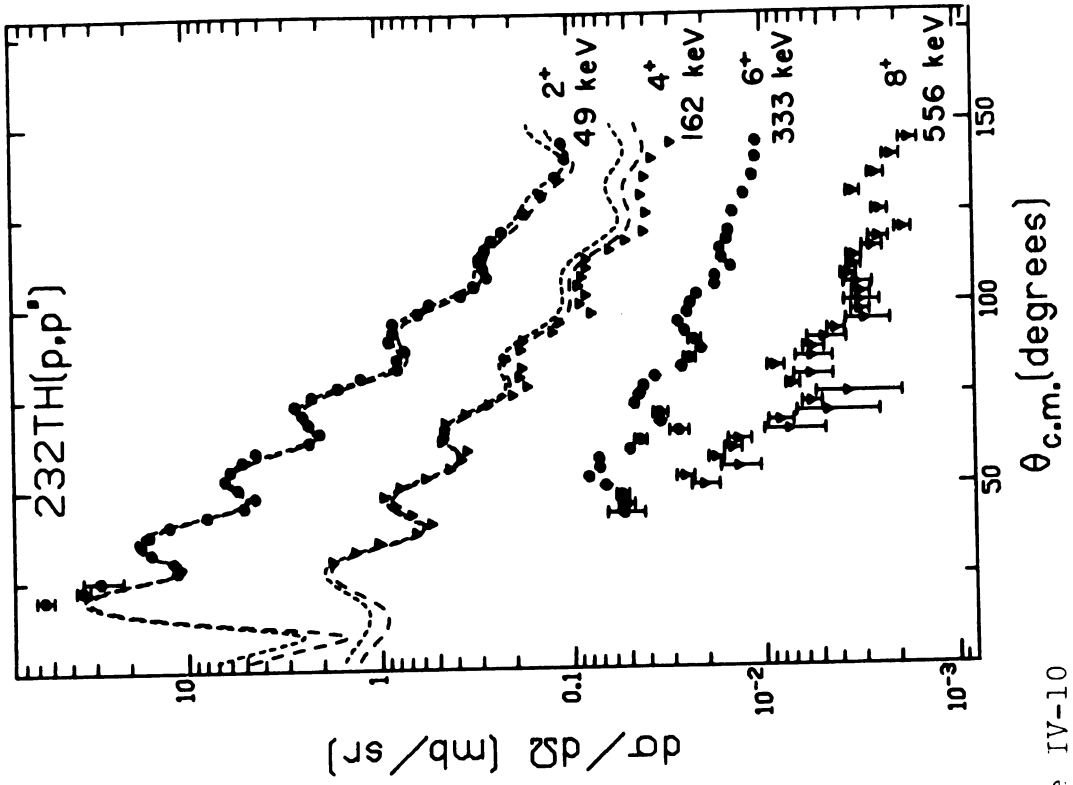


Figure IV-10

added 6^+ state is to lower the 4^+ cross section at back angle where the disagreement is worst (Figure IV-10). The use of a simultaneous search on a number of parameters with the full calculation eliminated this situation for ^{238}U and should be no different for ^{232}Th .

The scaled data were fit until a convergence was obtained with the β_4 and β_6 values not changing appreciably during the search procedure. Using these best fit parameters from the scaled data searches, the actual data were fit by varying V , W_D , V_{SO} , a , a_1 , β_2 , and β_4 simultaneously using a 0-2-4-6 deformed spin orbit calculation. The ^{232}Th data were also fit using a SSO calculation with searches on the optical model parameters V , W_D , V_{SO} , a and a_1 , and the deformation parameters β_2 , β_4 , and β_6 , using 0-2-4 and 0-2-4-6-8 SSO calculations respectively. The best fit parameters for the scaled data (DSO) and the actual data (SSO) searches appear in Table IV-4 with the best fits to the data illustrated in Figure IV-11.

^{234}U and ^{236}U Data Reduction

The starting points for the searches were the Becchetti-Greenlees optical model parameters with the β_2 and β_4 deformations parameters a result of 'BR scaling' of the Coulomb deformation parameters of Bemis [Be73]. The data were fit similarly to the other nuclei with the optical

Table IV-4. Best fit parameters resulting from fits to ^{232}Th data with deformed spin orbit (DSO) and spherical spin orbit (SSO) calculations.

RESULTS OF FIT				
Parameter	DSO	(error)	SSO	(error)
V (MeV)	52.973	(780)	53.024	(300)
W (MeV)	5.000		5.000	
W_D (MeV)	4.960	(420)	4.860	(280)
V_{SO} (MeV)	6.047	(350)	6.080	(170)
a (fm)	0.730	(17)	0.723	(10)
a_i (fm)	0.792	(14)	0.801	(10)
a_{SO} (fm)	0.750		0.750	
r (fm)	1.170		1.170	
r_i (fm)	1.320		1.320	
r_{SO} (fm)	1.010		1.010	
β_2	0.202	(2)	0.204	(2)
β_4	0.068	(1)	0.067	(1)
β_6	0.009	(2)	0.010	(2)

Figure IV-11. Best fits to the ^{232}Th data for the deformed spin orbit (DSO) and spherical spin orbit (SSO) calculations.

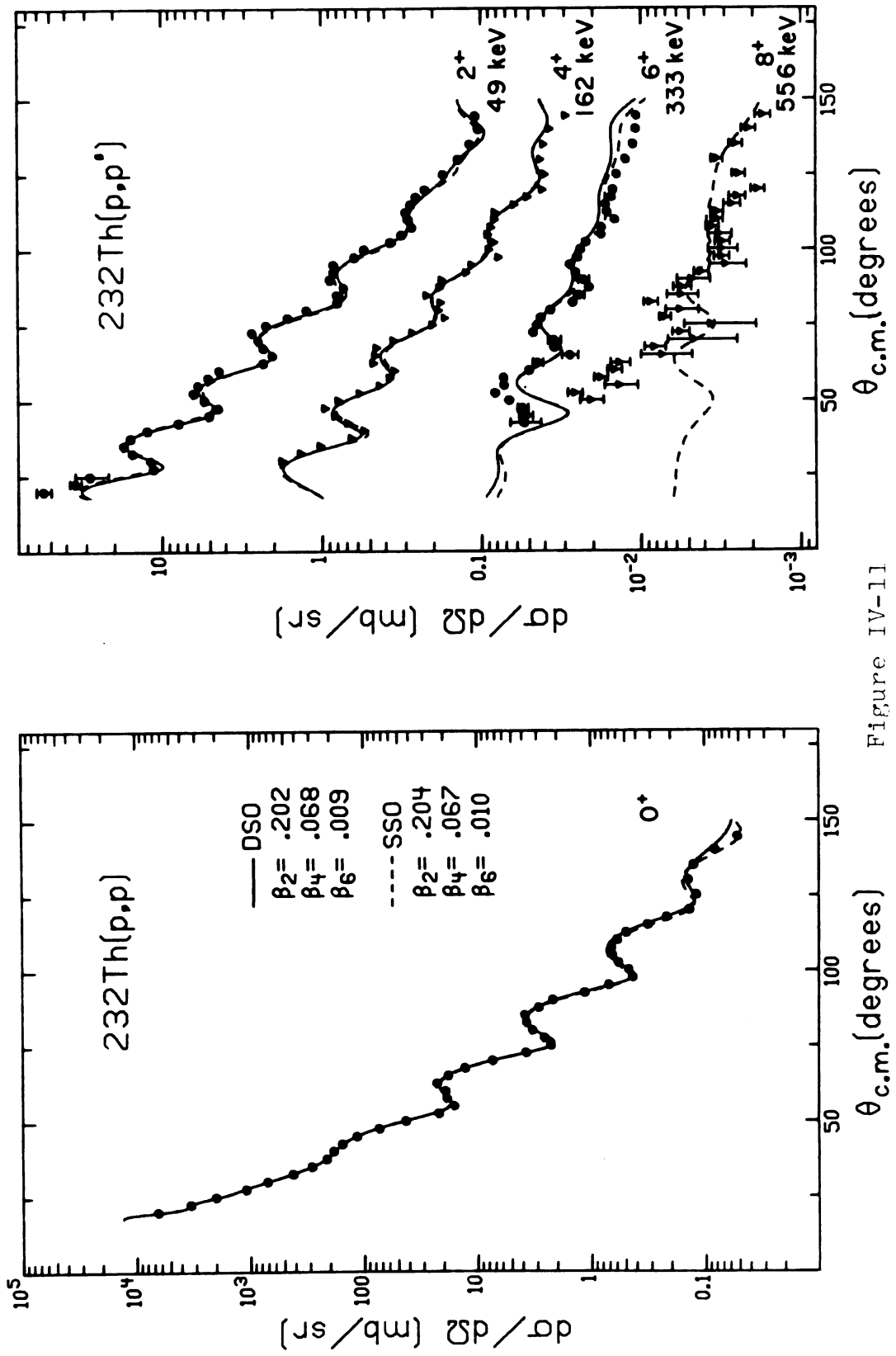


Figure IV-11

model parameters V , W_D , V_{SO} , a and a_1 searched on separately with a 0-2-4 calculation for the 0^+ angular distribution. The 2^+ angular distribution was fitted with the same calculation with the deformation parameter β_2 varied. The β_4 search was made using a 0-2-4-6 calculation with the 4^+ data weighted. This sequence was repeated until the parameters stabilized and the normalization rechecked for the forward angle elastic scattering data. A value for the β_6 parameter was found using a spherical spin-orbit (SSO) in a 0-2-4-6-8 calculation and searching for a minimum χ^2 value for the 6^+ state. The change in β_6 affects the fit of the other states so that the search procedure on the other parameters needs to be repeated until the values of the search parameters including β_6 stabilize and a minimum total χ^2 value is obtained for the 0^+ , 2^+ , 4^+ , and 6^+ data. The data were fit using a SSO calculation with couplings up to the 8^+ included. The optical model parameter values were found by minimizing the χ^2 value for the 0^+ angular distribution using a 0-2-4 calculation. The deformation parameters were evaluated using a 0-2-4-6-8 calculation to minimize the total χ^2 value for the 2^+ , 4^+ , and 6^+ angular distributions. Figure IV-12 and Figure IV-13 show the best fits to the data. Tables IV-5 and IV-6 list the parameters yielding the best fit to the data for both the DSO and SSO calculations.

Figure IV-12. Best fits to the ^{236}U data for the DSO and SSO calculations.

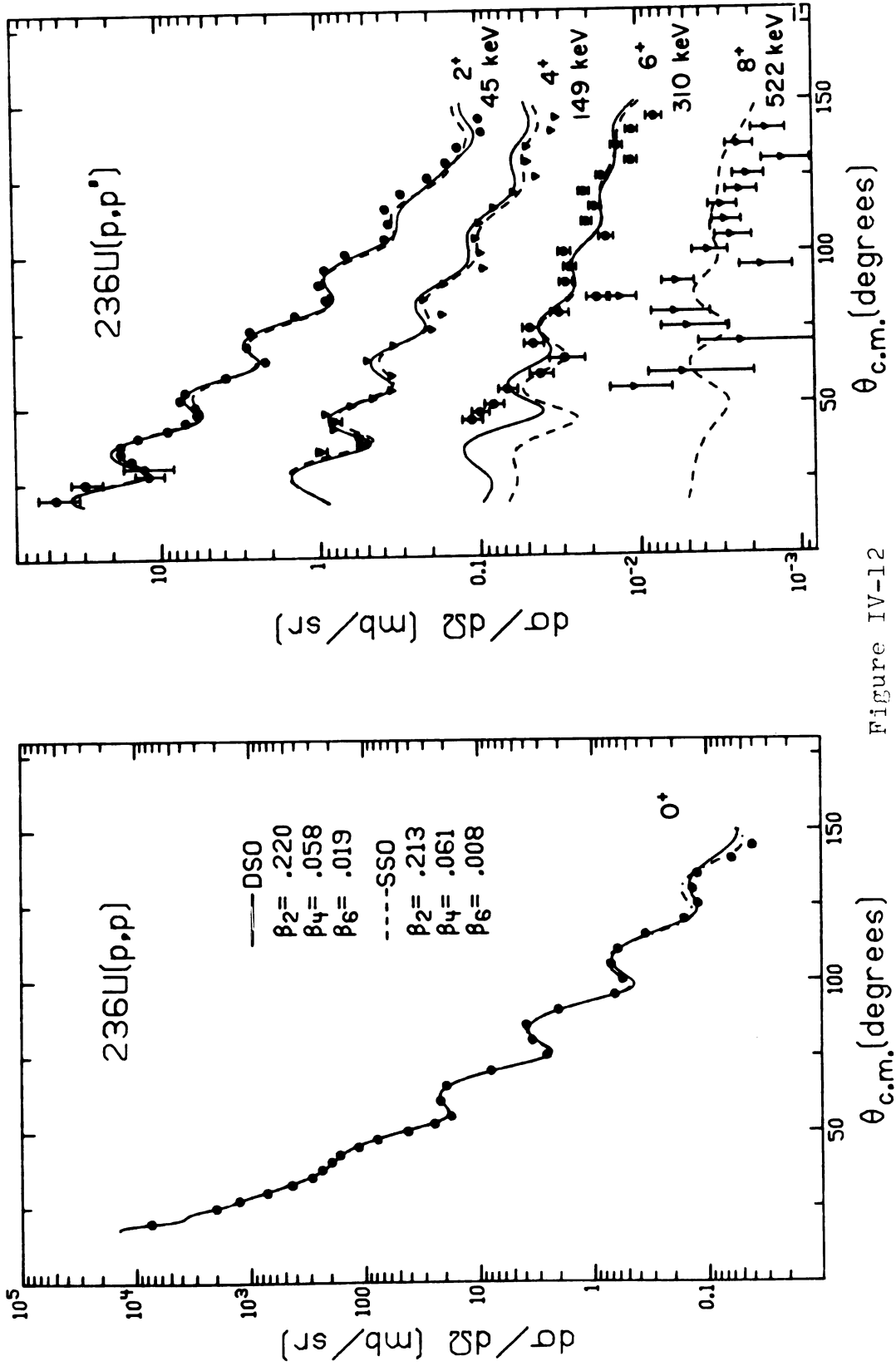


Figure IV-12

Figure IV-13. Best fits to the ^{234}U data for the DSO and SSO calculations.

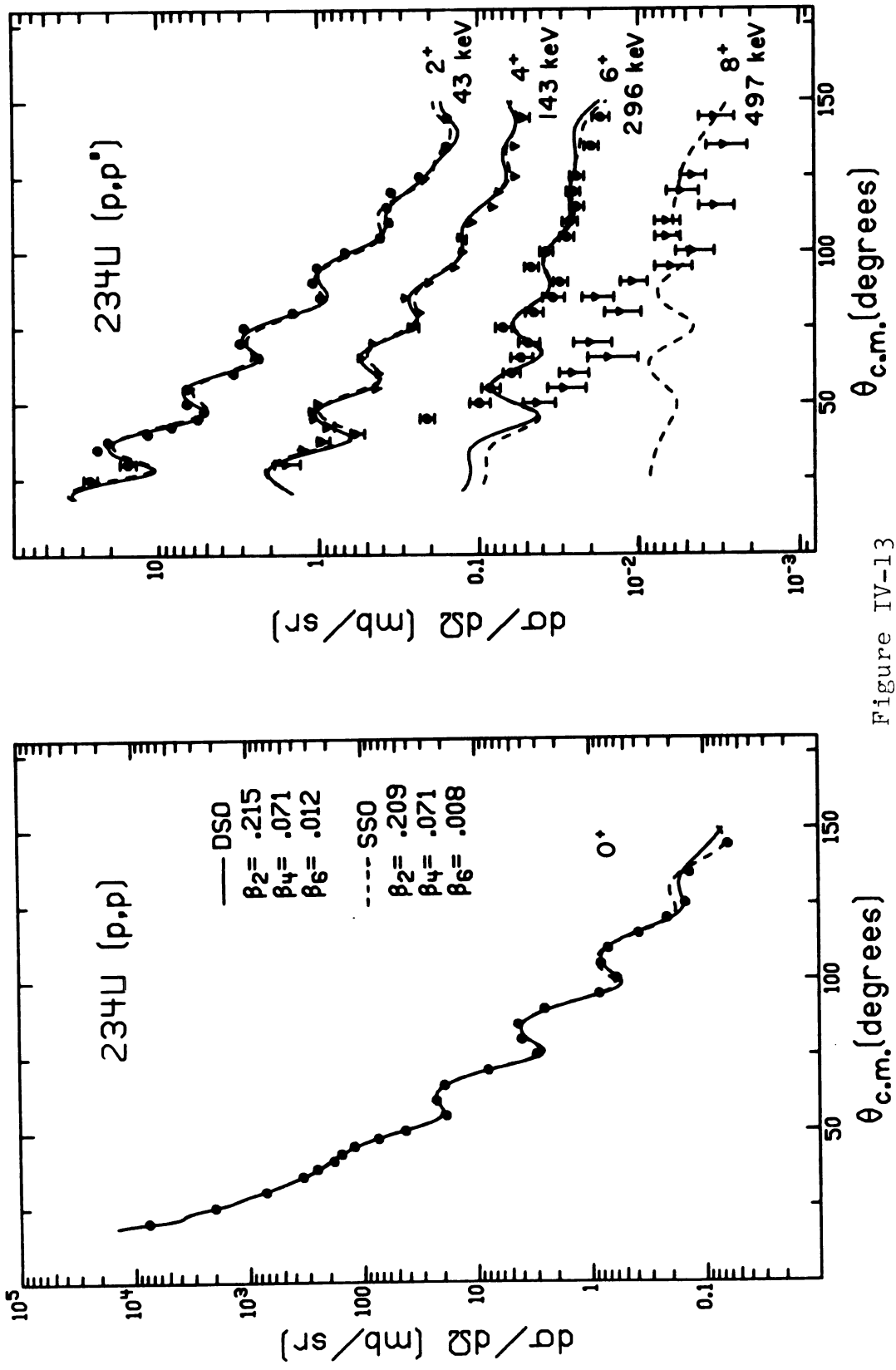


Figure IV-13

Table IV-5. Best fit parameters resulting from fits to ^{236}U data with deformed spin orbit (DSO) and spherical spin orbit (SSO) calculations.

RESULTS OF FIT				
Parameter	DSO	(error)	SSO	(error)
V (MeV)	52.716	(470)	52.890	(390)
W (MeV)	5.000		5.000	
W_D (MeV)	5.364	(480)	5.123	(660)
V_{SO} (MeV)	5.884	(600)	6.006	(700)
a (fm)	0.745	(22)	0.738	(40)
a_i (fm)	0.776	(22)	0.780	(45)
a_{SO} (fm)	0.750		0.750	
r (fm)	1.170		1.170	
r_i (fm)	1.320		1.320	
r_{SO} (fm)	1.010		1.010	
β_2	0.220	(2)	0.218	(2)
β_4	0.063	(2)	0.060	(2)
β_6	-0.003	(5)	-0.003	(5)

Table IV-6. Best fit parameters resulting from fits to ^{234}U data with deformed spin orbit (DSO) and spherical spin orbit (SSO) calculations.

RESULTS OF FIT				
Parameter	DSO	(error)	SSO	(error)
V (MeV)	54.792	(700)	54.938	(600)
W (MeV)	5.000		5.000	
W_D (MeV)	5.314	(970)	4.885	(560)
V_{SO} (MeV)	6.769	(420)	6.843	(550)
a (fm)	0.768	(22)	0.749	(12)
a_1 (fm)	0.722	(32)	0.729	(16)
a_{SO} (fm)	0.750		0.750	
r (fm)	1.170		1.170	
r_1 (fm)	1.320		1.320	
r_{SO} (fm)	1.010		1.010	
β_2	0.214	(2)	0.210	(2)
β_4	0.072	(2)	0.072	(2)
β_6	0.007	(4)	0.007	(3)

CHAPTER V

RESULTS AND DISCUSSION

The multipole moments are calculated using the best fit parameters from the data analysis within the coupled channels formalism. Figure V-1 compares the results of the deformed spin-orbit (DSO) and the spherical spin-orbit calculations. The results of this work are also compared with the microscopic calculation [Ne76]. These microscopic calculations [Ne76] involve finding the minimum of the nuclear potential energy treated as a function of the deformations. The wave functions of the nucleus at the equilibrium point are found and the moments are calculated using the multipole moment operators. In this calculation the average single-particle potential is expressed in terms of a harmonic oscillator potential. Overall, the trends of the moments resulting from the two analyses are similar, but not in complete agreement. For the uranium nuclei, the moments found using the SSO results are systematically lower. However, the moments for ^{232}Th calculated using the SSO parameters agree quite well with the moments calculated from the DSO results. The SSO calculations do not fit the ground state data as well as the DSO calculations for angles

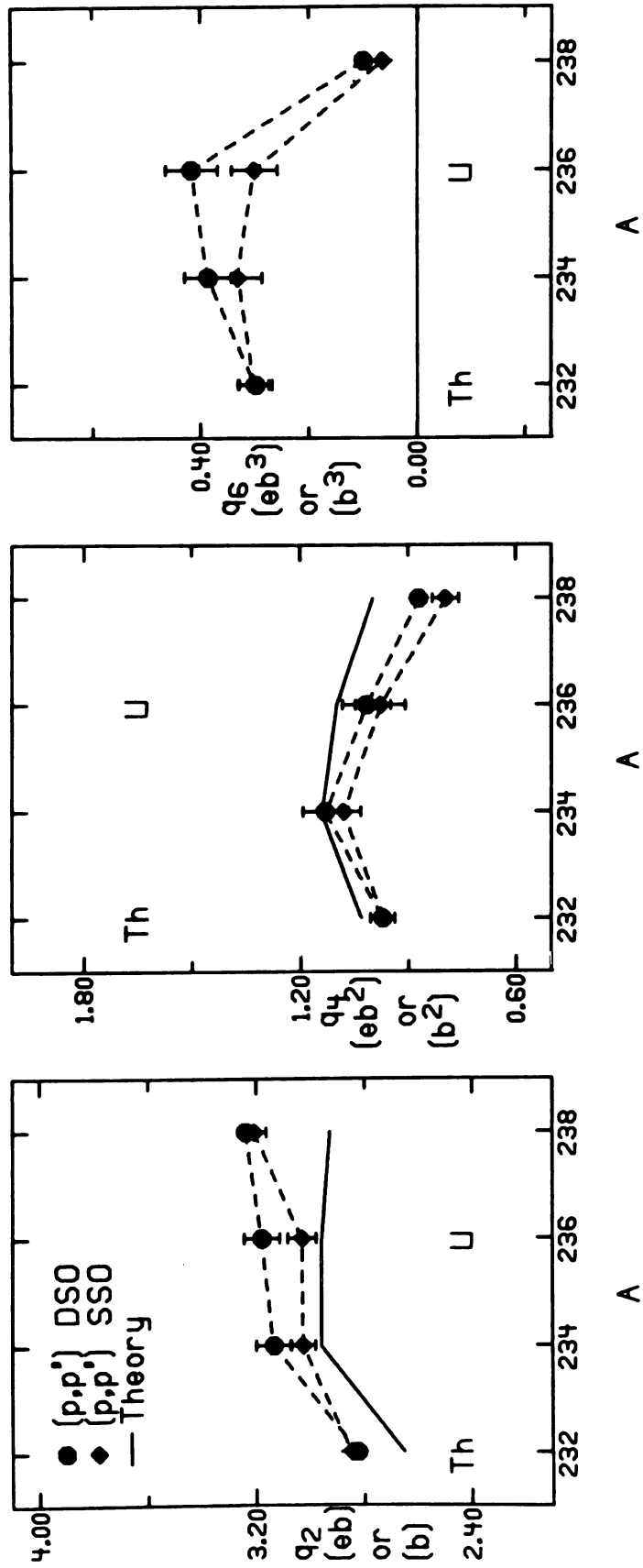


Figure V-1. Calculated moments for this work using the parameters which give a best fit to the data for DSO and SSO calculations.

beyond 120 degrees. Another major difference between the SSO and DSO calculations (Figures IV-5, 11, 12 and 13) is the phase of the cross sections. The diffusenesses and deformation parameters (Tables IV-2, 4, 5, and 6) are in good agreement for ^{232}Th for the SSO and DSO calculations. The same parameters show considerable deviations for the uranium isotopes with the DSO and SSO calculations. Since the DSO calculation leads to a better overall fit to the data, these results will be used in further comparisons.

The moments follow the trends predicted by the model of Bertsch [Be68], including the extension of the formalism to the q_6 moment (Figure I-4a). Although β_6 changes sign the moment does not but the trend indicates a change in sign for the q_6 moment in this region. Since this moment follows a predicted trend the β_6 value extracted appears to be physically significant not simply an artifact of the fitting procedure. The previously illustrated sensitivity of the fit to the data of the β_6 parameter, Figure IV-2, where the effect of using a non-zero β_6 value improves the fit, adds confidence to the extracted value. The quadrupole and hexadecapole moments also follow the trends predicted by this shell filling argument.

Figure V-2 compares the moments calculated using the DSO parameters with the moments from Coulomb excitation [Be73], electron scattering (e,e') [Co76], α -particle scattering [He73], and microscopic calculations [Ne74]. The q_2

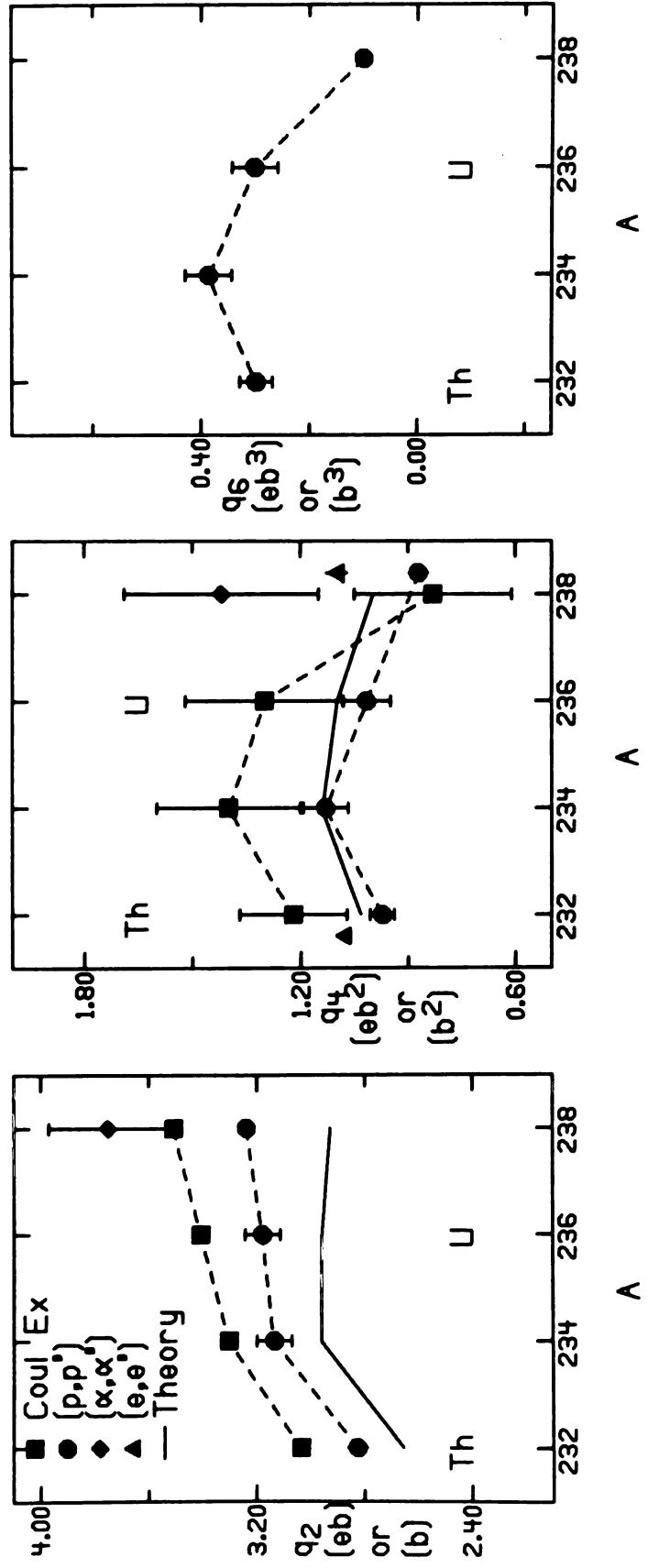
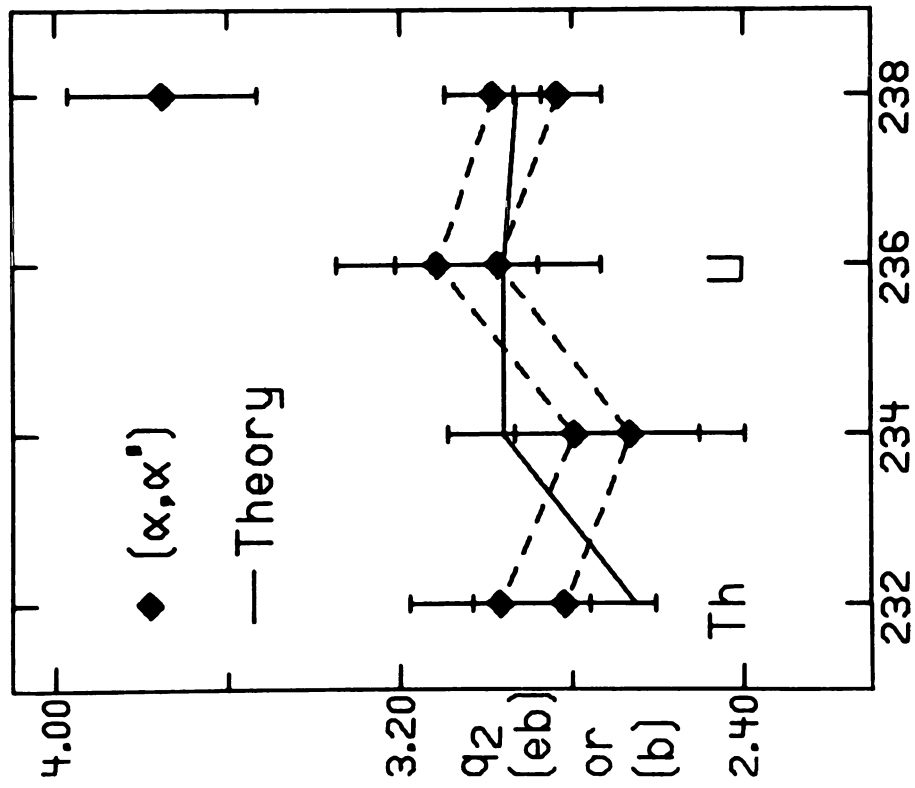
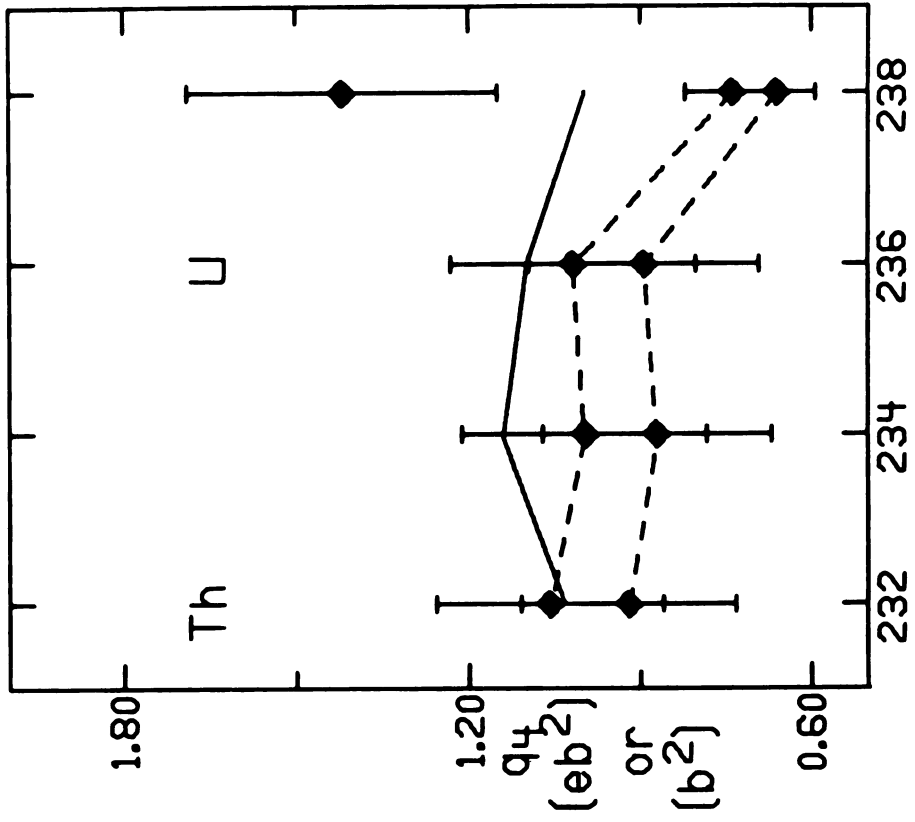


Figure V-2. Comparison of the moments resulting from this work with previous experimental results and microscopic calculations. See text for references.

moments for this work agree in trend with both the Coulomb excitation and theory although the Coulomb excitation results are between 5% and 8% higher and the theory consistently lower than the moments from this work. The q_4 moments agree in trend with the Coulomb excitation results for the three lighter nuclei although the magnitudes of the Coulomb excitation are between 24% to 28% higher. The trends of these two q_4 studies are in disagreement when ^{238}U is included. The q_4 moments from this work are 10% less than the (e,e') moments for ^{232}Th and 20% less for ^{238}U . Both trend and magnitude with the microscopic calculations are closely followed. The α -particle scattering q_2 and q_4 moments for ^{238}U using parameters from Reference [He73] disagree with the moments from this work. The Hendrie et al. [He73] results moments also disagree with the results of the systematic study by David et al. [Da76] (Figure V-3). The two studies use the same beam energy so that the Hendrie result should agree with the David result. This discrepancy may be in part due to the data analysis. A strong correlation was found between the charge and potential deformations and the charge deformation was fixed to yield the proper quadrupole moment. In this way the potential deformation is linked with the charge quadrupole moment. Since the α -particle scattering results are not reproducible, this indicates some problem or ambiguity in the analysis. There are two sets of values plotted for the

Figure V-3. Comparison of the moments obtained using α -particle scattering at 50 MeV.



A

A

Figure V-3.

David et al. study. The double values in the moments are the result of maintaining the same deformation parameters for different values of the optical model parameters including the volume term radius. Since the moments depend on a product of R and β , the doubled value situation exists. The (α, α') results appear to agree, within uncertainties, to the microscopic calculations, but the lack of any definite trend for the q_2 moment may indicate some inconsistency or model breakdown in the analysis.

The results of this work show agreement with the trends and, in part, magnitudes with the microscopic calculations for both the q_2 and q_4 moments. Neglecting the q_4 moment of ^{238}U , the Coulomb excitation measurements and this work show very similar trends, but with the above mentioned discrepancies in the magnitudes. This discrepancy, if significant, would indicate a smaller moment for the neutron distribution than for the proton distribution. This was also observed for the rare earth nuclei ^{154}Sm and ^{176}Yb , as well in the preliminary analyses of ^{232}Th and ^{238}U by King et al. This difference is opposite the difference predicted by Hartree-Fock calculations [NR77] which indicate that the charge moment is smaller than the nuclear moment. These calculations predict the neutron quadrupole moment to be 5% larger than the proton quadrupole moment for ^{232}Th and 3% larger for ^{238}U . The neutron hexadecapole moment is predicted to be 7% larger than the proton

hexadecapole moment for ^{232}Th and 1% larger for ^{238}U . The Hartree-Fock calculations differ from the above mentioned microscopic calculations. For each nucleon in this calculation, the potential used is the average potential generated by the other nucleons, with additional rearrangement terms used for density dependent interactions. The wave functions are found in a self-consistent method by iterating the potential and the wave functions until a solution is obtained. Typically, the starting wave functions are an expansion of the oscillator potential. The experimental results are in line with the findings of Mackintosh [Ma76] in work involving Satchler's theorem. His findings indicate that either the neutron density for certain heavy nuclei is much less deformed than the proton density or the folding model breaks down in an unexpected manner, inconsistent with the form of the density dependence most likely to occur, or with exchange effects, at least as they may be included at the present time. Thus there is an indication that the charge and matter distributions are different, but this issue is clouded by the necessary use of a model dependent analysis. Improvements to the analysis may include the use of independent deformation parameters for the real and imaginary terms in the DOMP, as is the case for the radii and diffusenesses. The addition of the 8^+ state to the DSO calculation would require considerably larger and more time consuming calculations, but would

allow a better determination of the value and the addition of an additional state may be used to evaluate β_8 if the data supports a non-zero value for β_8 .

APPENDICES

APPENDIX A

INTRODUCTION

The ability to obtain very narrow (50 μm) [No74] lines for charged particles using nuclear emulsions in the focal plane of the Enge split-pole spectrograph [Sp68] at the Michigan State University Cyclotron Laboratory makes it an excellent device to measure the ultimate position resolution obtainable with position sensitive detectors. Markham and Robertson [Mk75] were able to measure a position resolution of 220 μm FWHM for 35 MeV protons, using the inclined cathode delay line counter. From this measurement, they were able to determine a contribution of 140 μm FWHM due to residual effects in the counter. The residual width is caused by effects associated with charge collection in the counter and secondary ionization of the proportional counter gas. A program was undertaken to develop position sensitive detectors in order to study the resolution attainable with thin proportional counters.

The goal of the program was the development and use of small position sensitive gas proportional counters. The counters were built for particles at normal incidence to minimize energy loss straggling effects in the counter

gas which usually dominate resolution at 45 degrees [Mk75]. At normal incidence there are still contributions to the observed line width from the line width of the beam, multiple scattering in detector window and gas, and electronic noise. The contribution of the beam has been measured independently using photographic emulsions [No74]. Multiple scattering effects are minimized by normal incidence and the residual contributions can be calculated, for both the window and the counter gas. An analysis of the contributions to line width by the gas and window appear in Table A-I. The electronic noise for resistive division counters was estimated by injecting test pulses into the preamplifiers.

To obtain normal particle incidence, the counter is placed at an angle of 45 degrees to the focal plane. Since the detector is not parallel to the focal plane, the particle groups cannot be focussed at all points along the detector, resulting in the need to stabilize the position of the peak on the detector. A computer feedback system is used to control the spectrographic magnet power supply while maintaining the position peak within a fixed window. The computer also outputs the peak width by using a digital to analog convertor (DAC) and a meter to give a visual readout of the peak width during the beamline tuning process [No74]. A difficulty with using a thin detector for lightly ionizing particles such as 35 MeV protons is that the energy loss of the particle in the detector is small,

Table A-1. Estimation of contributions to line width for thin proportional counters.
 All contributions in μm are added in quadrature.

Counter	Window	Gas ^c	Electronics	Beam	Total Calculated	Measured	Residual
1 mm Resistive Division	15 ^a	1	20	35 ^d	43	50	25
2 mm Resistive Division	5 ^b	2	20	45 ^e	50	65	41
2 mm Delay Line	5 ^b	3	--	45 ^e	45	65	47

^a6 μm Havar.

^b6 μm aluminized Mylar.

^cPropane (1 atm).

^dMeasured independently with speculator.

^eCalculated from measured peak widths using kinematic defocussing of ^{16}O peak.

requiring high gains in the counter. With appropriate choice of gas filling and some attention to construction details to permit operation at high voltages, adequate gas gains can be obtained. In this work, two techniques for position readout were used, charge division with a resistive wire and delay-line readout of induced signals from a low resistance wire.

CONSTRUCTION AND PERFORMANCE

Two resistive wire counters were built using 25 μm carbon coated quartz wire [Zv01]. The first detector was 1-mm thick and used a sandwich type construction as shown in Figure A-1. Its active area was 10 mm long and 2.5 mm in height. The sandwich consisted of a pair of 0.5 mm thick spacers glued to either side of the wire, with 6.25 μm Havar windows glued to the outsides. The wire leads out of the sandwich were made using Havar strips. The wire was held in place with a conductive adhesive, which also limited the resistive portion of the wire to the active region (resistance = 80 k Ω). This module was placed in a frame which made the gas and electrical connections to the spectrograph. The operational bias was 1850 volts on the wire for a propane gas filling at 1 atmosphere pressure. A position resolution of 50 μm FWHM (full width at half maximum) along the detector (70 μm FWHM along the

EXPLODED VIEW

THIN PROPORTIONAL COUNTER
 TOTAL THICKNESS = 1 mm

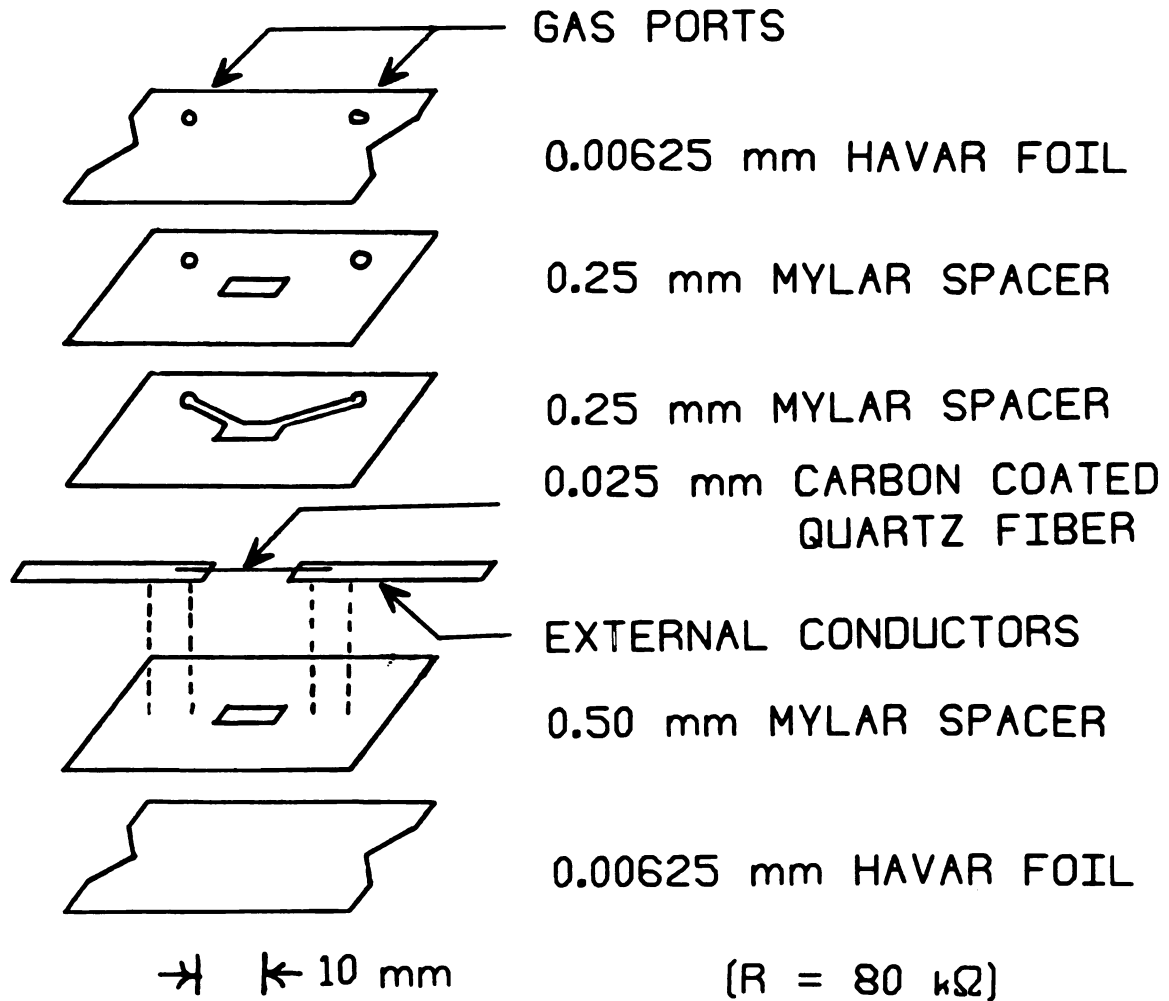


Figure A-1. Exploded view of 1 mm thick resistive division counter.

focal plane) was observed (Figure A-2) for 35 MeV protons elastically scattered from a $20 \mu\text{g}/\text{cm}^2$ carbon foil. The position spectrum represents an energy loss selection compromising about 40 percent of the total events. It was found that selecting particles with a particular energy loss signal yielded resolution about 20 percent better than the position resolution resulting from the acceptance of all events. Electrical breakdowns occurred often because of the small spacings in this counter. These damaged the resistive coating on the wire resulting in the need for frequent wire replacement. In order to improve the reliability, a 2-mm thick resistive counter was built using the same wire and active area as the first design. The new design used 1-mm thick G-10 fiberglass laminate spacers to support the wire in a groove cut into the aluminum body of the detector as in Figure A-3. The quartz wire was held in place using a conductive adhesive which also made electrical contact with larger wires connected to the feed-throughs. A line width of $65 \mu\text{m}$ (FWHM) along the detector was measured with this detector. This counter was more reliable than the first as the bias required was similar but the breakdown paths were longer. However, the carbon coating on the quartz fiber deteriorated for high counting rates (10 KHz) in a localized area (.1 mm) during the tuning process. This deterioration takes the form of a resistance change which results in position nonlinearities. To further

Figure A-2. Position spectrum for 35 MeV elastically scattered protons.

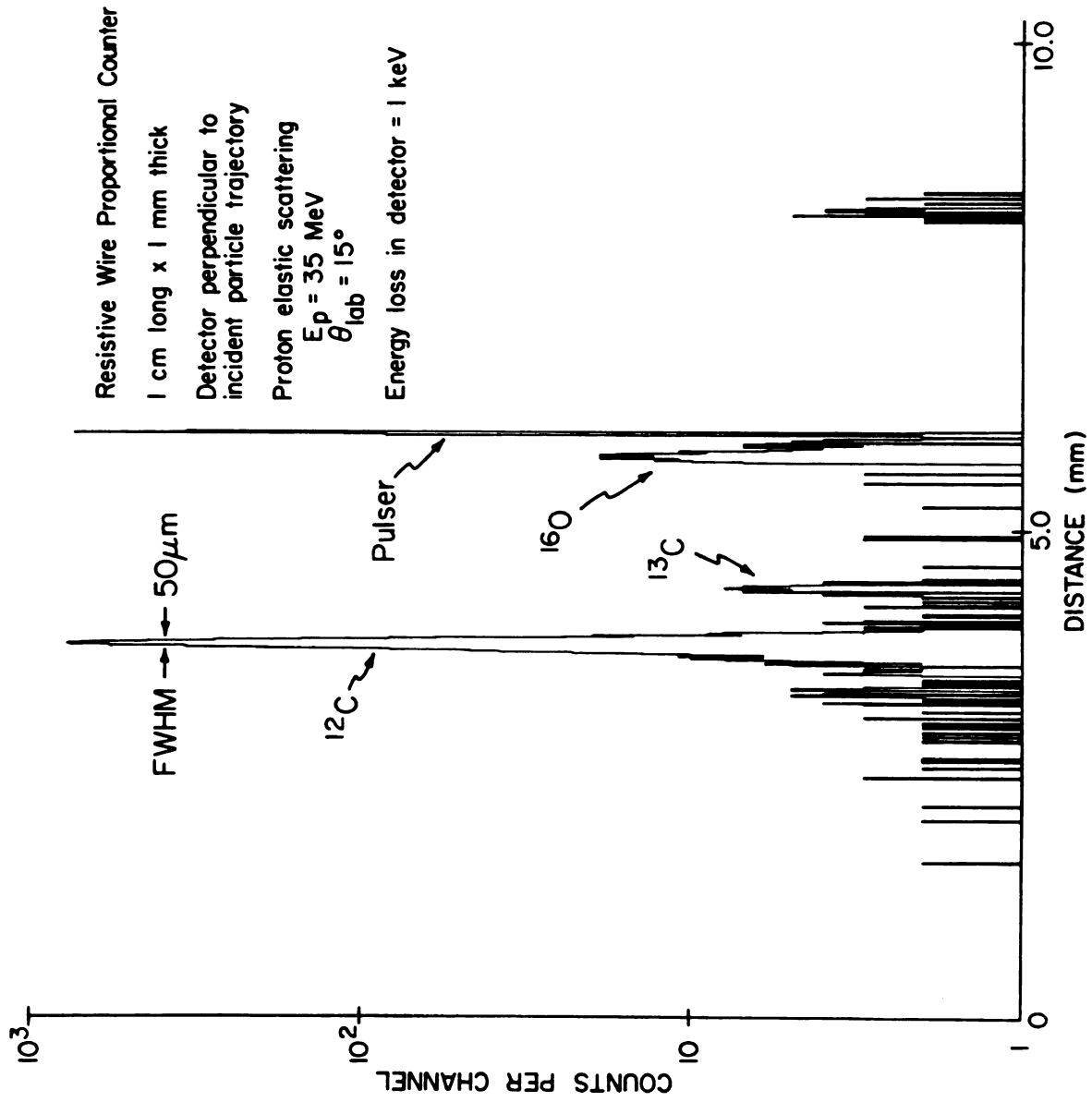


Figure A-2.

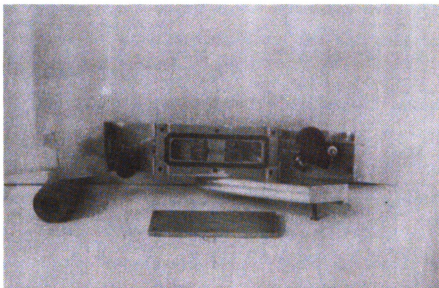


Figure A-3. Photographs of 2 mm thick resistive division counter. Lower (closeup) photograph is about twice the actual size.

improve the reliability, a readout mechanism not requiring the fragile carbon-coated quartz filament is needed. The highest resistivity metal alloy wires currently available in small diameters ($<10\ \mu\text{m}$) are much too low in resistance for such short detectors.

A second type of detector was built utilizing tapped delay-line position encoding as shown in Figure A-4. The active region was 2 mm thick, 10 mm long and 2.5 mm high. The anode was a $25.4\ \mu\text{m}$ diameter tungsten wire attached to a Delrin bridge. The delay-line is a commercially available 14-pin dual-in-line package [Da01] having 10 taps with a total time delay of 500 nsec and a 500 Ohm impedance. The pickup stripes are 0.90 mm wide with 0.10 mm spacing between each. The stripes are made by vacuum deposition of copper using a mask onto a circuit board which connects the stripes with a standard 14 pin IC socket. The mask is made by stretching 0.10 mm diameter wires between 2 screws with a pitch of 10 turns per cm, allowing the production of very uniformly spaced stripes with well defined edges. Techniques such as chemical etching and machining leave rough edges and etched stripes are subject to some undercutting. To produce a smooth surface for deposition of the stripes, the board was coated with lacquer and sanded smooth. This fills the slight irregularities in the G-10 circuit board. The delay line pickup board attached to the wire bridge, defining the lower surface of

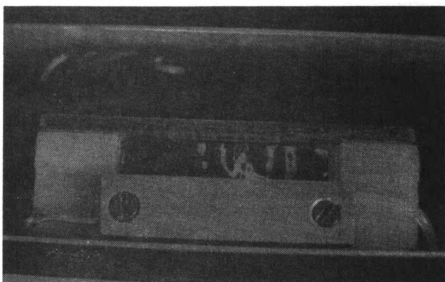
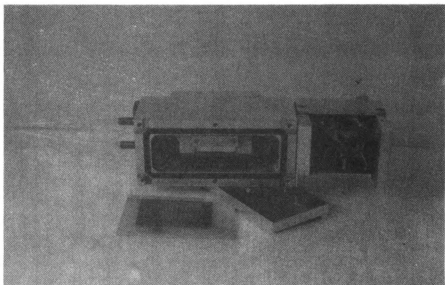


Figure A-4. Photographs of 2 mm thick delay line counter. Lower (close-up) photograph is about twice the actual size.

the active area. An aluminum block secured the 6 μm thick Havar back plane which defined the upper surface of the active area. The entire assembly was installed in a gas tight box with a 6.25 μm aluminized Mylar window. Electrical connections were made to the ends of the delay line and to the anode wire through a Kovar feedthrough. When biased to 2200 volts with propane at 1 atmosphere pressure, a position resolution of 65 μm FWHM along the detector was obtained for 35 MeV protons at normal incidence, scattered from a carbon foil. Figures A-5 and A-6 show comparable spectra for the 2 mm thick resistive wire counter and for the 2 mm thick delay line counter. This detector was quite reliable since the components are much less sensitive to damage from localized high counting rates, and the design allowed breakdown free operation at higher voltages.

ELECTRONICS

The charge division counters used charge sensitive preamplifiers, one at each end of the wire to obtain energy loss signals. The output signals were sent to amplifiers for shaping and further amplification with the analog signals summed to give the total energy loss. The ratio of the signal from one end and the sum signal yielded the position. The ratio was calculated by converting the two analog signals to digital values and dividing using the

Figure A-5. Position spectra using 2 mm thick resistive division counter.

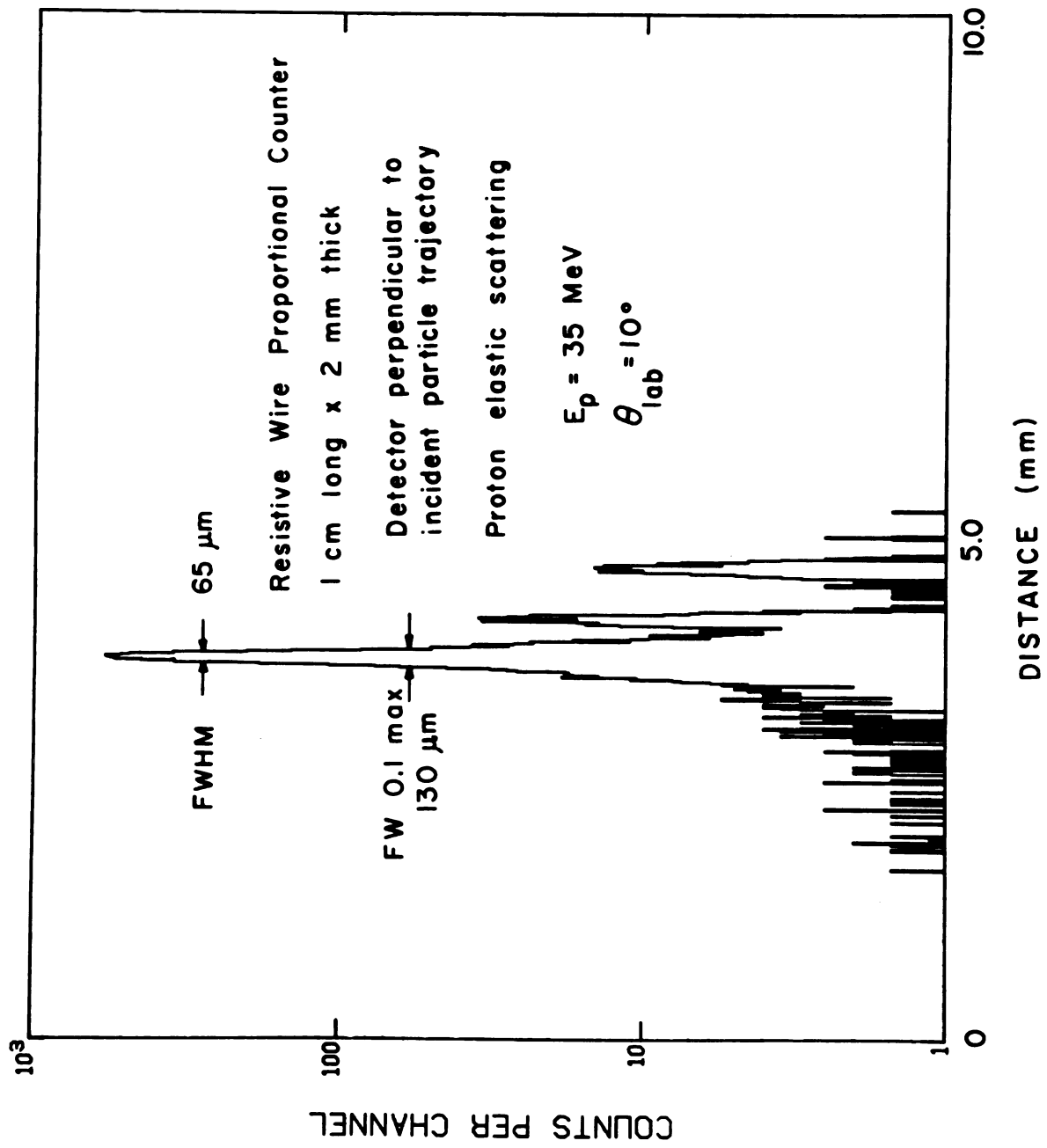


Figure A-5.

Figure A-6. Position spectra using 2 mm thick delay line counter.

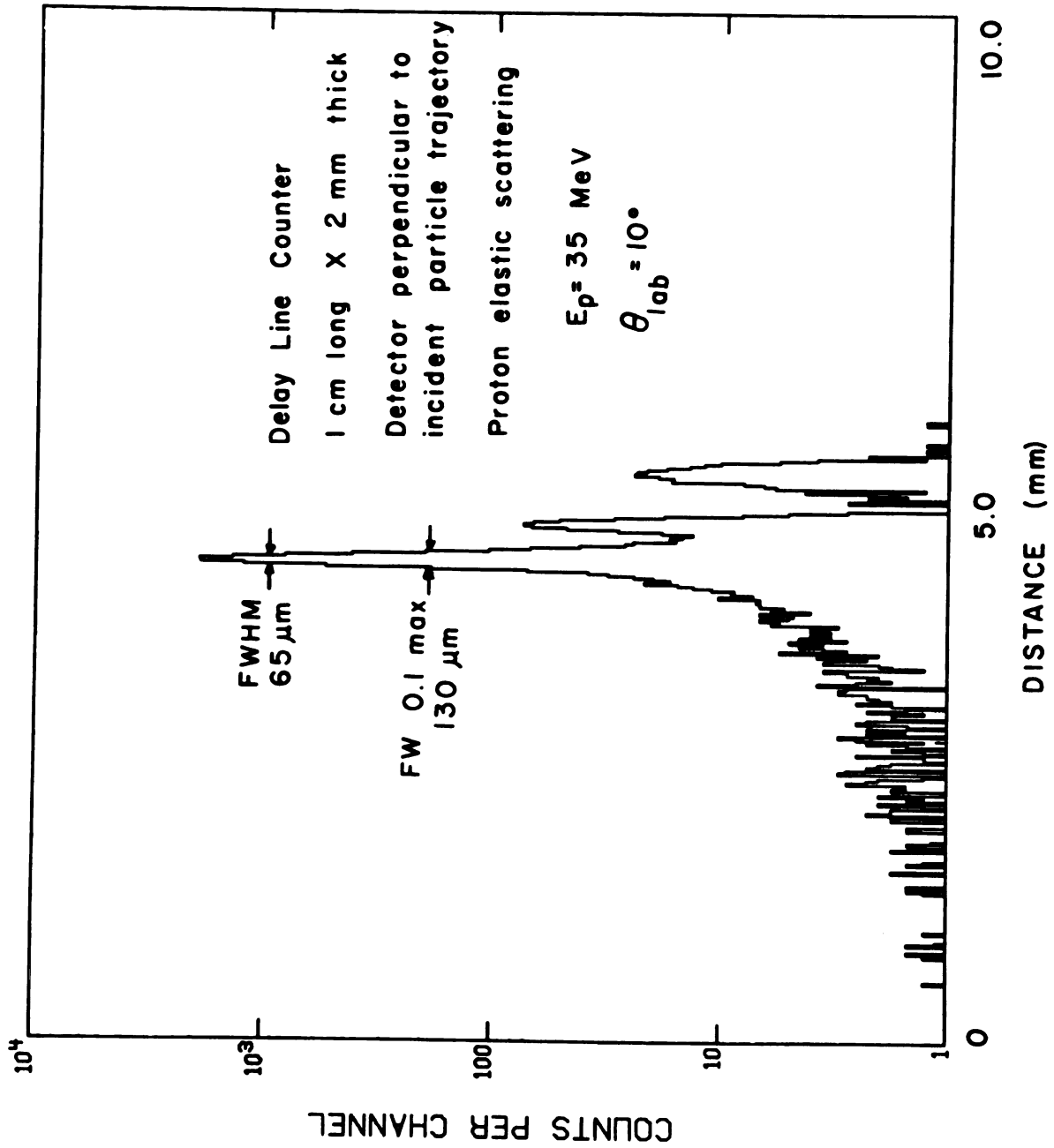


Figure A-6.

computer. Figure A-7a illustrates the electronics setup used for signal processing. The bias network consisted of a current limiting resistor and isolation capacitors between the wire and preamplifiers.

The delay-line counter electronics differ from the resistive division electronics as timing signals were necessary. A schematic is shown in Figure A-7b. The bias network contains a current limitation resistor with the provision to obtain a signal from the wire through an isolation capacitor. The delay line was resistively terminated to match the input impedance of the preamplifiers. The signals from each end of the delay line were preamplified and the output signal were processed by timing filter amplifiers (integration time constant = 200 nsec, differentiation time constant = 100 nsec). A constant-fraction discriminator was used to derive timing signals from the timing filter amplifier output. The position was extracted by using the signal from one end to start a time-to-amplitude converter (TAC), and the signal from the opposite end, delayed in time by the total delay of the delay line, to stop the TAC. The TAC output is the position and was analyzed using a computer. Both types of counters could be backed by a silicon detector for particle identification. For the tuning procedure this was not necessary since the elastically scattered protons dominated count rates.

Figure A-7. Schematic of electronics used with a) resistive division and b) delay line position encoding.

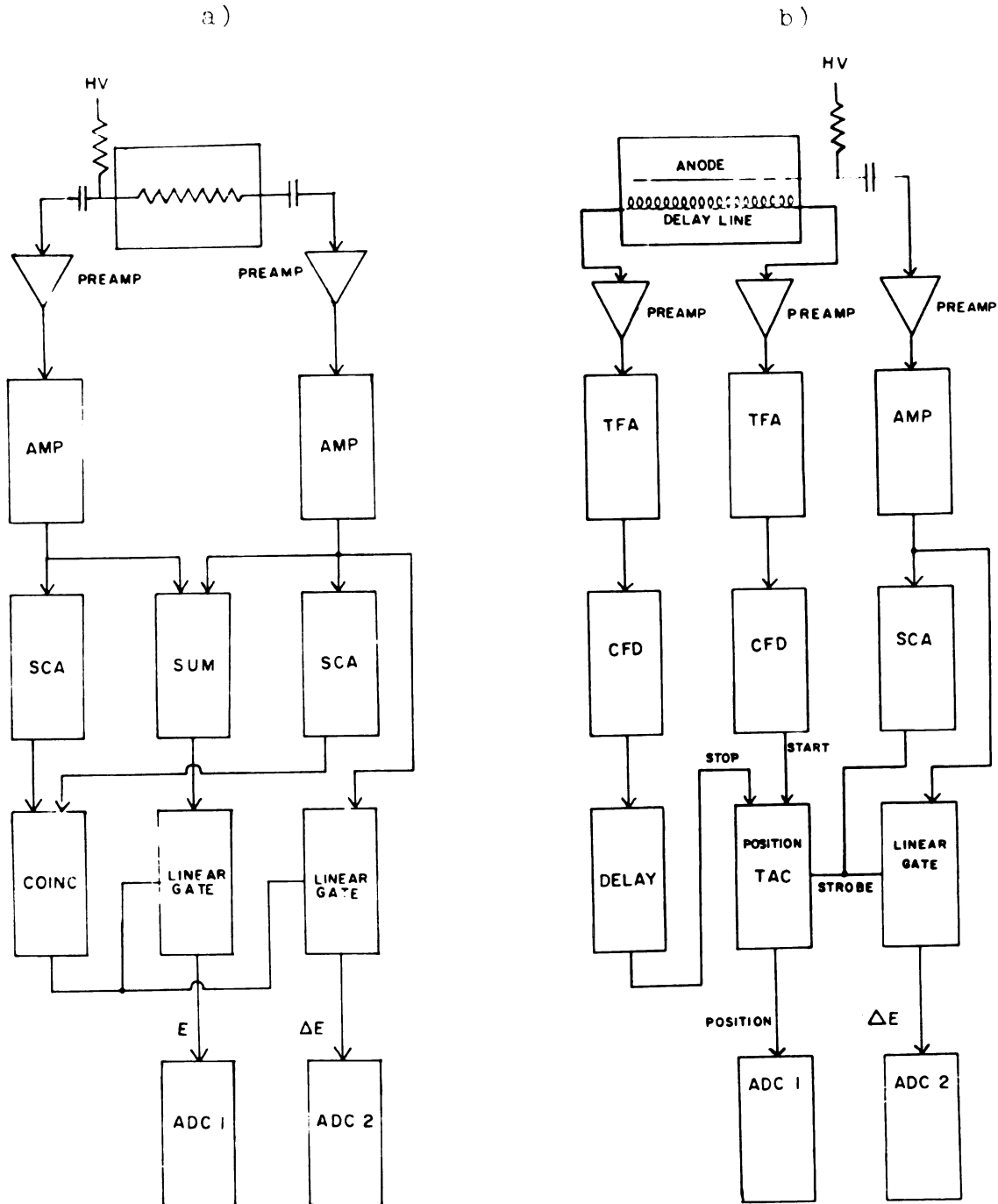


Figure A-7.

RESULTS

New upper limits were obtained for the optimal position resolution available with gas-filled proportional counter for charged particles. Muller et al. [Mu71] have achieved a spacial resolution of 40 μm FWHM with a xenon filled multiwire ionization chamber. Table A-1 lists the position resolution obtained and the contributions to the width. The residual contributions to the line width include a number of line broadening effects which are difficult to isolate. They may include spreading of the avalanche, photon or electron propagation along the wire, diffusion of primary electrons, and variations or fluctuations of the multiplication along the wire. The improved resolution achieved by selecting a narrow range of particle energy loss allows further analysis of the resolution degrading effects. Spectra corresponding to both high and low energy loss selection show poorer resolution. The former indicates that secondary ionization producing events such as scattered electrons or photon propagation in the gas cause a spreading of the line. Since the resolution improves with bias the gain-dependent effect of photon propagation can be judged to be less dominant. The low energy loss signal could result from either incomplete charge collection or a smaller energy loss in the gas. Incomplete charge collection could result in excessive spreading of the

avalanche due to diffusion of the primary electrons. An event with a small energy loss would result in a greater uncertainty in the position measurement. Since the resolution improved with bias, the effects of charge collection appear to dominate and can be controlled.

In addition to tuning of the beam line elements for narrow lines for a variety of particles, the study of closely spaced states in scattering experiments is feasible.

APPENDIX B

The limitations of the detectors used for taking the data in this thesis pointed to the need for a more sophisticated position readout. The design, construction, and testing of a multiwire proportional counter (MWPC) was undertaken. The MWPC is a position sensitive detector which has found considerable use in high energy physics [Ch70] and in electron scattering [Be77]. It was recently a subject of a review article for nuclear physics [Ba79]. This type of readout uses an array of wires and the drift time of electrons in the proportional gas to determine the position of a particle track. An advantage of the multiwire readout is high spacial resolution (<1 mm) can be obtained for large detectors (>1 m) for high count rates (10^4 sec⁻¹).

Figure B-1 illustrates the wire plane which is the basic component of this device. The wire plane consists of smaller diameter active wires and large diameter guard wires. The active wires obtain this designation in that charge multiplication occurs at only these wires producing measurable signals. The guard wires are for field shaping and also isolate the active wires from each other. A particle passing through the gas filled region surrounding the wire plane leaves a track of electron-ion pairs in the

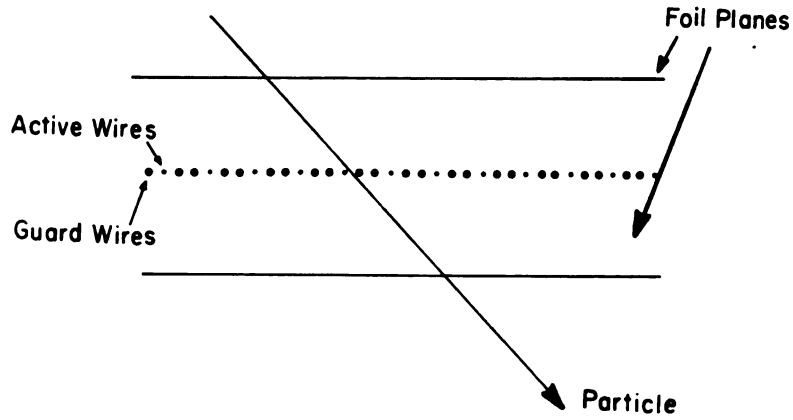


Figure B-1. Schematic view of wire plane for MWFC.

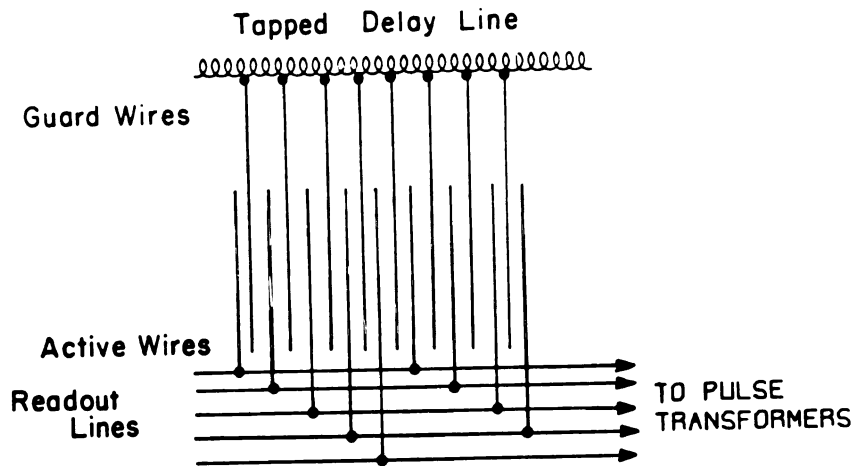


Figure B-2. Schematic of Active and guard wire connections.

gas. The fields produced by the wire plane collect the electrons. Charge which is collected by the active wires is multiplied by the high field surrounding the active wires. The active wires collect only a portion of the total number of electrons created since the charge is also being collected by the guard wires. A number of active wires will produce signals for each particle. This is an advantage of the multiwire readout in that the position of a track can be found by measuring its location at several points. This type of readout is less sensitive to resolution degrading mechanisms and background caused by collecting charge from a large volume. Measuring the position at a number of locations reduces the errors caused by the skewing of the centroid as a result of energy loss fluctuations over a large region. This effect was found to be a major contribution to resolution [Mk75].

POSITION READOUT

The time required for the electrons to drift from their origin on the track to the wire is related to the distance travelled. The electrons, under the influence of the electric fields produced by the wires, quickly attain terminal velocity due to collisions with the electrons in the gas. The only appreciable charge multiplication occurs in the region roughly equal to twice the collection

wire diameter. To measure the position relative to a wire requires only the measurement of the drift time. Finding the position of a track relative to two or more wires allows the calculation of the trajectory of the particle through the detector. By knowing the angle of incidence of the particle at the detector, corrections can be made for use of a larger defining aperture, aberrations in the spectrograph, or for a subdivision of the scattering angle within the angular range of the defining aperture when this is important. One application might be to measure the fine structure in an angular distribution using a large solid angle defining aperture, or a slotted aperture, where a number of closely spaced angles can be measured simultaneously.

The measurement of the trajectory with this type of MWPC readout is possible only if the particle trajectory is at an oblique angle to the wire plane, so that the particle track is projected onto the wire plane. If the angle is small such that only one wire collects charge the trajectory information could be obtained by using two position sensitive detectors separated spacially along the trajectory.

In the multiwire counter the position is measured relative to each individual wire. This is advantageous in that the integral linearity is limited by the accuracy of the wire placement. The position resolution is nearly

independent of the length of the counter, unlike position readouts which utilize resistive division or delay-line encoded position readout.

This MWPC readout differs from the standard digital readout [Ba79] which uses a separate preamplifier and discriminator for each active wire and uses digital electronics to find the particle track position. The present design is similar to the Bates device [Be77], using analog position encoding. Every fifth active wire is interconnected as in Figure B-2 and the five signals processed through preamplifiers. Thus for 90 active wires only 5 preamplifiers and discriminators are required. The determination of the group of wires involved is accomplished by coupling the guard wires to a delay line. The avalanche at the active wires induces a signal on the guard wires. The signal, using the delay line, can be used to locate the group of wires involved. The wire in the group nearest to the particle track produces a signal first and can be readily identified. By adding two additional preamplifiers and discriminators to accommodate the delay line readout, and by utilizing a CAMAC multistop time digitizer the drift time measurements become simple. The position and angle of the particle track and the aberration corrections can be calculated by using software to decode the timing information and display the results. An advantage of using software is that diagnostics can be implemented in addition to display and gating.

The position relative to the wires, or fine position, is calculated using one of two methods, first-wire-timing or fiducial timing. The first-wire-timing scheme involves three active wires as in Figure B-3. By using the first wire to produce a pulse as a start signal, the relative times

$$\tau_+ = T_+ - T_0 \quad (B-1)$$

$$\tau_- = T_- - T_0$$

can be measured. These two times are used to calculate the position by

$$X = \frac{d}{2} \left[1 - \frac{\tau_{<}}{\tau_{>}} \right] \quad \text{where} \quad \begin{array}{l} T_{>} = \tau_{\pm} \\ T_{<} = \tau_{\mp} \end{array} \quad \begin{array}{l} \tau_+ > \tau_- \\ \tau_- > \tau_+ \end{array} \quad (B-2)$$

where d is the active wire spacing. The tangent of the angle of incidence, found using geometrical relationships is

$$\tan \theta = \frac{V}{d} \tau_{>} \quad (B-3)$$

where V is the electron drift velocity which is a constant value.

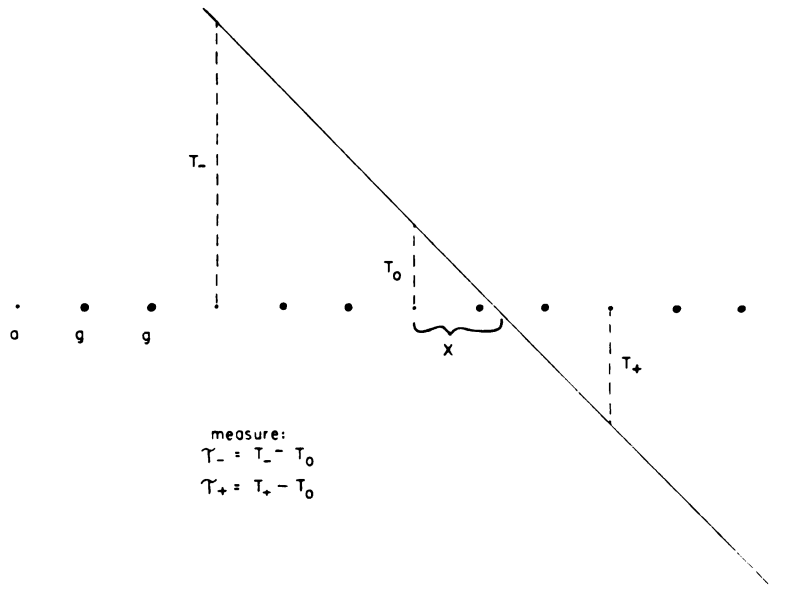


Figure B-3. Illustration of the times measured to derive position.

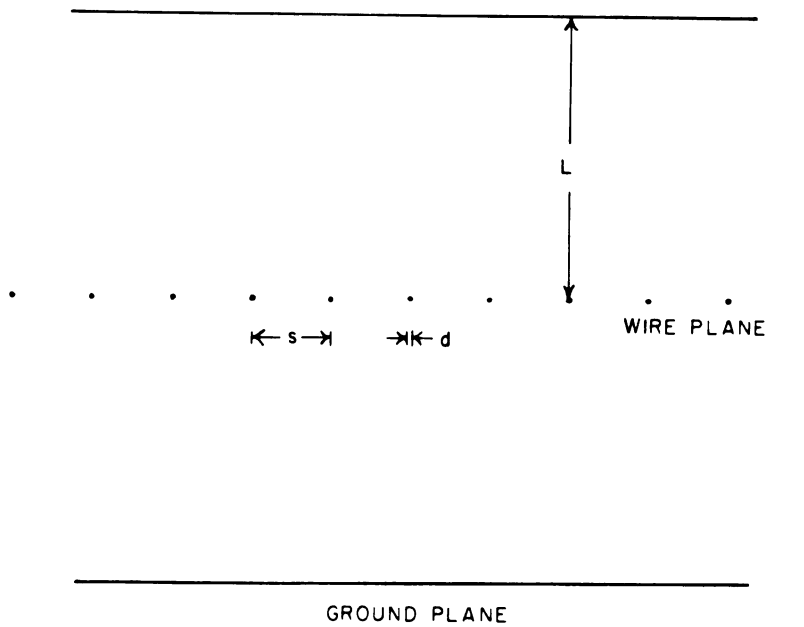


Figure B-4. Geometry of the counter showing dimensions important to the electrical characteristics of the counter.

The fiducial timing scheme involves using an external start such as the anode signal from a photomultiplier and scintillator. Similar to the first wire method, the two relative drift times are measured, with some time offset t_z ,

$$\tau_- = T_- - t_z \quad (B-4)$$

$$\tau_+ = T_+ - t_z$$

The position relative to a wire is

$$X = \frac{\tau_- - \tau_+}{\tau_- - \tau_+ - 2t_z} \quad (B-5)$$

and the angle can be determined from the relation,

$$\tan\theta = \frac{V}{2d} (\tau_- + \tau_+ - 2t_z) \quad (B-6)$$

The term t_z represents an offset in time as the result of derivation of the time with two separate devices. The fiducial timing scheme involves only two time derivations in the MWPC where the first wire mode involves derivations of two relative times using three wires. The fiducial timing mode is more accurate since the error introduced by photomultiplier ($dt \approx 1$ ns) should be negligible compared to the timing error of the multiwire counter wire

($dt \approx 5$ nsec). The active wires give the fine position, that being relative to the first wire in the group to produce a signal. The wire location (coarse position) can be found by determining the wire group with the delay-line position encoding and by knowing which wire produced a signal first. The actual position is found by adding the fine position to the wire position, which is equal to its location times the wire spacing. The delay-line position resolution needs to be accurate enough that the base width of a peak be less than 5 active wire spacings (30 mm). In the case of delay fluctuations a calibration of the delay line readout can be done relative to the nearest active wire to prevent misidentification of the active wire group involved. Diagnostics which may be built in include testing for coarse and fine position linearity, and correct wire identification. Another diagnostic is the calculation of the sum of the two delay line signals which can be used to reject simultaneous events. The sum signal is proportional to the delay line length which is well defined. Variations from the true length could be used to reject an event.

DESIGN

The design problems to be overcome in the MWPC include higher operating voltages caused by the closely spaced

wires, the requirement of highly uniform fields and stable gains, and the accurate mechanical placement and tensioning of the wires. Also, the effects of energy loss fluctuations for minimum ionizing particles are enhanced because relatively small segments of the particle track are used to derive the position. An additional and important consideration is the electronics and signal processing aspects of this type of device.

TIMING CALCULATIONS

Energy loss fluctuations were studied by performing a series of Monte Carlo calculations modeling the pulse development at a single wire in the counter. The Monte Carlo calculations were started by modeling the field lines for the geometry involved as in Figure B-4 (page 152). An expression [Er72] for the potential produced by an array of wires with diameter d , spacing s , and distance L from the grounded surfaces is

$$V = q \ln\left[\sin^2\left(\frac{\pi X}{s}\right) + \sin^2 h\left(\frac{\pi Y}{s}\right)\right] \quad (\text{B-6})$$

The coordinate system is centered on a wire with the x direction along the wire plane and the y direction perpendicular to it. The charge per unit length q is,

$$q = V_0 / (2[\ln \sinh(\frac{\pi L}{S}) - \ln \sinh(\frac{\pi d}{S})]) \quad (B-7)$$

where V_0 is the induced potential. Figure B-5 shows the calculated field lines illustrating the regions from which each wire would collect charge. The electrons produced by a particle track drift along the field lines toward the anode wire. Collisions cause the electrons to quickly attain terminal velocity. Due to the different path lengths for the electrons, the arrival times at the anode wire are different. The first step is the determination of a relation between the position on the track and the arrival times. The arrival time as a function of position is found by integrating the time required to drift towards the wire, starting at some location in the cell. The drift time is directly proportional to the y-direction beyond a region whose extent is roughly the wire spacing. The drift time is more dependent on changes in the x-position in the cell if the y-position is such that the track is in the uniform field regions far from the wire plane. The oblique angle of the particle track results in a more complicated problem in that the charge starts from a range of vertical positions in addition to a range of horizontal positions. To increase the speed of the calculation, a functional relationship between the position on the track and the arrival time was derived. This relationship is used in the simulation by

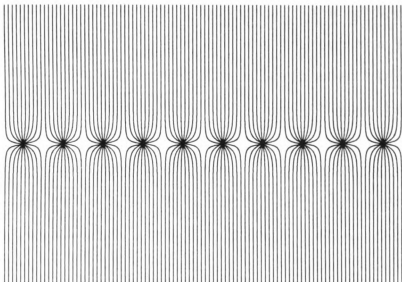


Figure B-5. Illustration of the calculated field lines for the counter wire plane.

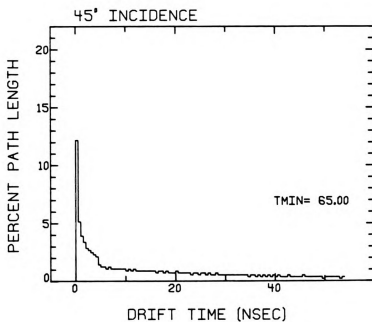


Figure B-6. Fraction of the particle track length arriving within a time segment.

dividing the particle track into equal time of arrival segments, illustrated in Figure B-6 which shows the fraction of the particle track length arriving in each time segment. The time development of the pulse is determined by randomizing the amount of energy loss in each segment using a Blunk-Liesegang energy distribution [Ev74] and a random number generator. The distribution is used to find the arbitrary energy loss ΔE in the path length segment by

$$\Delta E = E_{mp} + \Lambda \left\{ 0.300 mc^2 \frac{Z/A}{\beta^2} Z_1 X \right\}$$

where E_{mp} is the most probable energy loss,

m is the electron mass,

Z and A are the atomic number and mass of the medium,

Z_1 is the incident particle atomic number; and

β is the velocity of the incident particle. Λ obeys

the Blunk-Leisegang distribution

$$F(\Lambda)d\Lambda = 0.145 \exp\left[-0.5\left\{\frac{1}{2}\Lambda + \exp\left(-\frac{1}{2}\Lambda\right)\right\}\right] \quad 0 < \Lambda < 12$$

$$F(\Lambda)d\Lambda = 0.880 \exp[\Lambda^2/26] \quad \Lambda \leq 0$$

(B-9)

The pulse development is modeled by integrating the formation of the avalanche with the charge from the various segments arriving at the calculated times. The time development of the avalanche can be approximated by the Wilkinson form [Wi50]

$$Q(t) = q N e \ln \left(\frac{t+t'}{t'} \right) \quad (\text{B-10})$$

where V_0 is the applied potential,
 q is the charge per unit length,
 t' is a constant = 1.8 nsec, and
 N is the number of positive ions leaving the site of
the anode wire.

The output pulse is calculated by applying integration and differentiation to the simulated pulse. The combined integration and differentiation relation for a pulse $A(t-t_0)$ is

$$Q(t) = A(t-t_0) \left[1 - \exp\left(-\frac{t-t_0}{\tau_{\text{int}}}\right) \right] \exp\left(-\frac{t-t_0}{\tau_{\text{diff}}}\right) \quad (\text{B-11})$$

where τ_{int} and τ_{diff} are the integration and differentiation time constants. The resultant pulse is processed using both constant fraction and fixed level discrimination models. The arrival time is defined as the time at which the pulse triggers the discriminator. The derived timing and uncertainty is used to find the uncertainty in the position as a result of the ionization fluctuations.

The angle of incidence of the track, the integration and differentiation time constants, and the discriminator values or fractions were varied. Different particles and energies were considered with an emphasis on 35 MeV protons

due to the minimum ionization involved. Figure B-7 shows the result of the calculations. The results show correlations of the timing uncertainties with integration and differentiation time constants. The resolution depends on the fraction used with constant fraction discrimination or the discriminator level for fixed level discrimination. Table B-1 lists the timing uncertainties and predicted position resolution for an individual cell in the multiwire counter. The geometry produces a sizable fraction of the total charge arriving very quickly (12% of the track in .5 nsec) so that the earliest portion of the pulses are relatively free of timing jitter. Better timing resolution can be obtained by using discriminators set with low levels or constant fraction timing with lower threshold values. The use of proper integration and differentiation of the pulse is also necessary to make use of the accurate leading edge of the pulse.

ELECTRIC FIELD DISTRIBUTIONS

The electric fields in the active area and in other regions of the counter were calculated by relaxation calculation methods [Ur75]. Relaxation calculations are based on the solution to Poisson's theorem, where the potential is continuous and the potential at any point is the average of the potential at surrounding points. The relaxation

Figure B-7. Results of the pulse modeling calculation illustrating the effect of the integration and differentiation time constants on the resolution and pulse height.

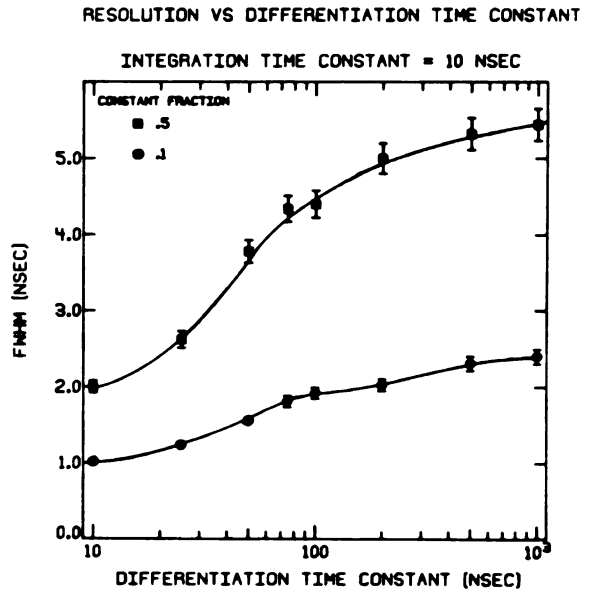
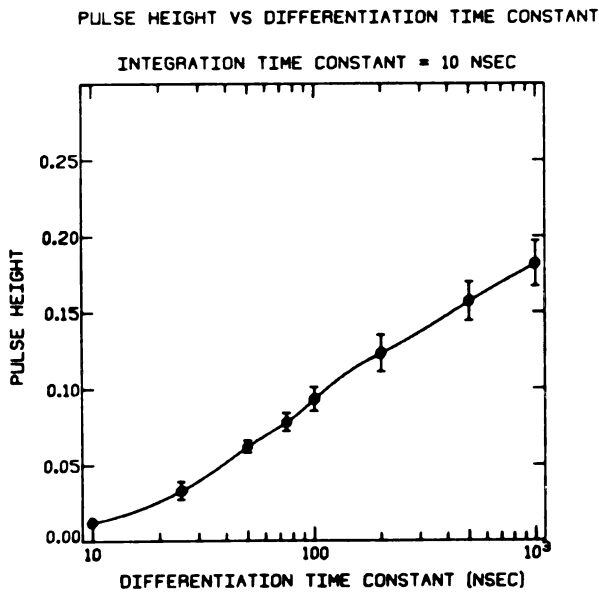
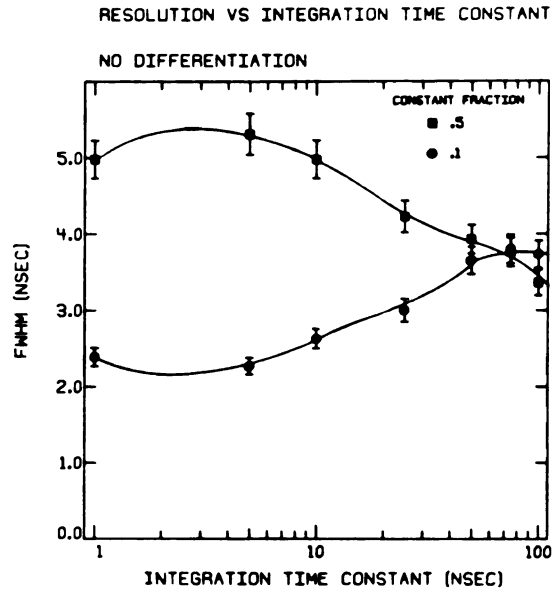
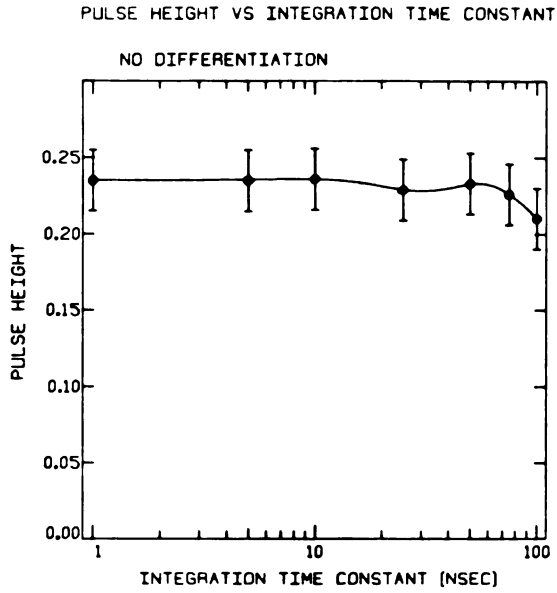


Figure B-7.

Table B-1. Time and spatial resolution for leading edge and constant fraction timing.

Fraction	Leading Edge		Constant Fraction	
	FWHM (nsec)	FWHM (μm)	FWHM (nsec)	FWHM (μm)
.02	1.3	52	1.2	50.
.05	2.5	100	1.5	60.
.10	4.3	185	2.0	80.
.25	---	---	2.8	110.
.50	28.8	1150	4.4	190.

calculation is accomplished by over-relaxation [Ko68], which forces a rapid convergence to the final solution by increasing the magnitude of the correction. The potential at any point in the mesh is found using the relationship

$$V_{\text{new}} = (1 - \text{RF})V_{IJ} + \frac{\text{RF}}{4}(V_{I-1, J-1} + V_{I-1, J+1} + V_{I+1, J-1} + V_{I+1, J+1}) \quad (\text{B-12})$$

once the boundary conditions are fixed. V_{IJ} is the potential at the point in the grid being evaluated, $V_{I\pm 1, J\pm 1}$ are the potentials of the surrounding points and V_{new} is the new value of the potential at the point being evaluated. The relaxation factor, RF was typically set to a value of 0.4. If dielectric material is present the terms in the average are weighted accordingly. The averaging and over-relaxation are repeatedly applied to all points in the mesh, with the exception of the boundary and other fixed potential points, until all points in the mesh converge where convergence is defined by the maximum change for any point being less than a specified value.

This calculation was done to insure that the electric field in the active region is uniform and to locate possible high field regions which would present possible problems in voltage handling capabilities. It is necessary that the fields in the active region be uniform to

produce path lengths and gas gains to be independent of position in the counter.

Ideally, high field regions should be created only in the dielectric materials rather than in the proportional gas. Figure B-8 illustrates the result of the relaxation calculation for the preliminary design. The region labelled A contains high fields as illustrated by the closely spaced potential lines. The field would be roughly 8000 volts/cm for the operating counter. This region also contains the anchor points for the wires and the delay-line, although not included in the calculation, would lead to even higher fields in this region. In order to lower these fields, field shaping planes were installed. These consisted of charged conductor on insulating boards. Figure B-9 shows the calculated potentials for this improved geometry. The high fields are now in the region filled by the insulating material. The high field regions at the edges of the conductors cause the closely spaced potential lines and are tolerable as these regions can be filled with dielectric material to prevent electrical breakdown and corona.

The corona induces electronic noise in the counter causing the discriminators to trigger randomly. The corona is the result of leakage current along surfaces and through the gas. Electrical discharges across gaps can be controlled by increasing the path length for the discharge or by filling the gap. Consider the parallel plate

Figure B-8. Potentials resulting from the preliminary relaxation calculation.

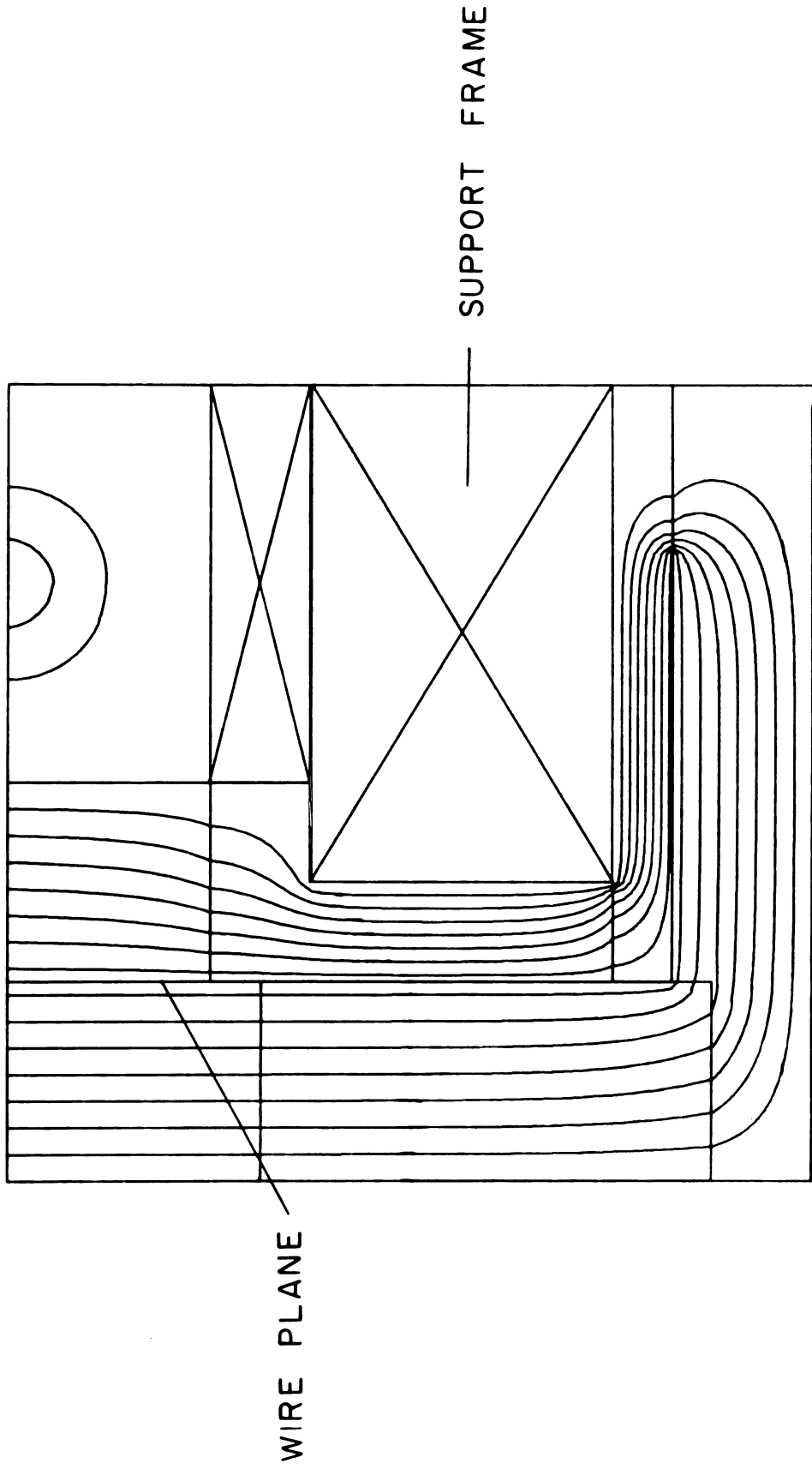


Figure E-2.

Figure B-9. Potentials resulting from the relaxation calculation with the addition of field shaping planes.

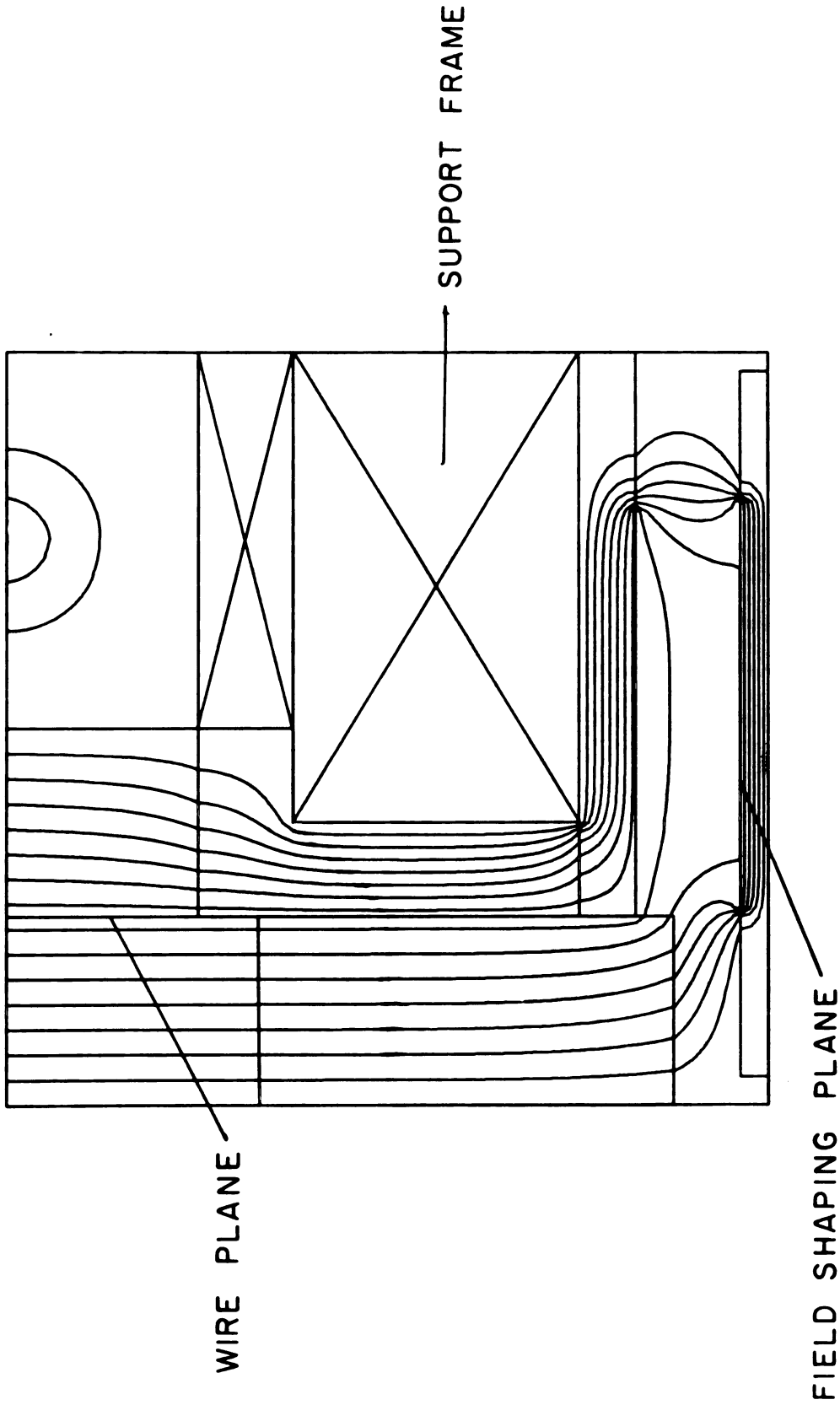


Figure B-9.

capacitor in Figure B-10a. The field in the gap is well known and it is also known that if a dielectric is inserted filling a portion of the gap as in Figure B-10b, the electric field in the gap is increased. This increase in the field can be enough to cause an electric breakdown in the gap even if the dielectric has a breakdown field strength higher than that of the field of the gap before the dielectric was inserted. One method of preventing a discharge in the gap is to completely fill the gap with dielectric material. For the construction of the counter, it was important to eliminate gaps between dielectrics and conductors which would be prone to discharges. Joints between dielectrics should be normal to the electric field lines rather than parallel with them, and there should be no penetrations through the dielectric materials which could provide paths for surface discharges.

Surface discharges may be limited by increasing the path length that the discharge must follow or to use materials which inhibit discharges. The susceptibility of various materials to surface discharge was determined. Different material was placed between parallel plates, with the plates allowed to extend beyond the material so that the edge of the material is parallel to the electric field. To measure surface discharge rate a charge sensitive pre-amplifier is connected to one of the plates. Charge flowing along the surface creates current pulses which can be

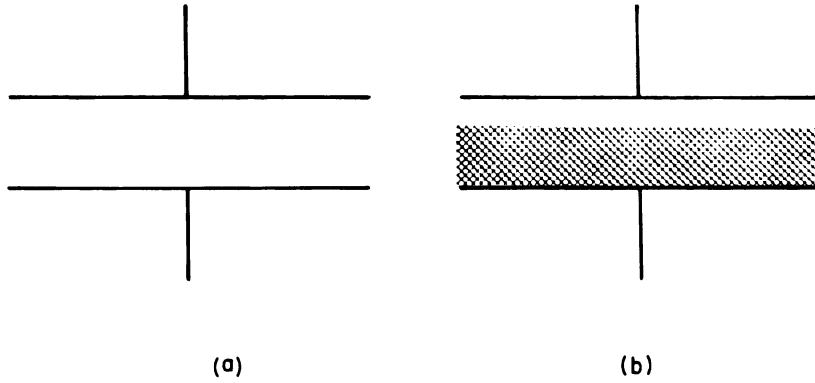


Figure B-10. Parallel plate capacitor, a) without and b) with the dielectric material inserted. The electric field in the air-gap increases with the dielectric slab.

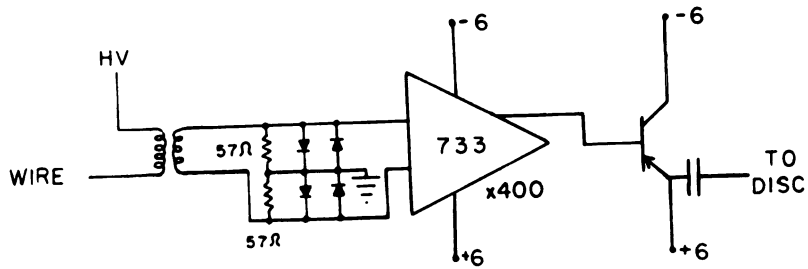


Figure B-11. Schematic of preamplifier used in the MWPC.

detected and amplified. By scaling the amplified pulses in a multichannel analyzer, results could be obtained which allow the comparison of various materials. The materials G-10 (resin impregnated fiberglass) and teflon had the best resistance to surface discharge. The G-10 has an interesting characteristic of producing a considerable discharge rate when the potentials are changed. The discharge rate drops to minimal values when the potentials are fixed. It is believed that a surface charging process takes place with the surface charge flowing and establishing uniform fields along the surface of the material. The G-10 was chosen as a principal construction material because it is dimensionally stable and it is relatively easy to fabricate. The adhesive used for construction was a high quality epoxy which could be vacuum-pumped to remove entrapped gas before use so that the adhesive layers are relatively free of gaps.

ELECTRONICS

The electronic instrumentation for the MWPC include the active wire readouts, the delay line and termination, high voltage isolation, and the bias network. The timing measurements require the handling of fast pulses. The degradation of the time resolution ultimately results in poorer position resolution. The preamplifier was a 733

differential video amplifier whose configuration is depicted in Figure B-11 (page 168). This device has a 40 MHz bandwidth and is designed to have excellent gain stability and low phase shifts. Results of the pulse modeling calculation show that the timing resolution strongly depends on the level at which a discriminator is set relative to the total peak height. This necessitates a stable gain to prevent timing slew and resolution degradation. The wide bandwidth assures that the high frequency portions such as the sharp leading edge of the pulse are not lost. The preamplifier is also compact which leads to simple implementation in the space available.

To couple the active wires and delay line to the preamplifier requires a device which allows isolation of the high voltage of the wire plane from the preamplifier circuitry. An isolation capacitor is precluded in this device because the high operating voltages used require capacitors to be physically large. The large capacitance values (500 pf) would result in a considerable amount of energy stored in the capacitor bank of 7 capacitors. This stored energy would be detrimental to the preamplifiers and delay line components in the event of electrical breakdowns.

Another approach is to use pulse transformers to achieve high voltage isolation. By adequately insulating the primary windings it is possible to use the pulse transformer to obtain very good signal transmission. The

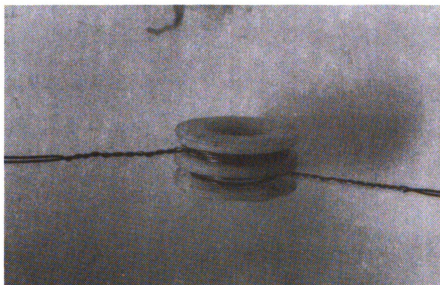
turn ratio of the transformer can be adjusted to achieve impedance matching to the delay line. Two types of transformer geometries were tested, a ferrite pot-core with isolated windings and a toroidal ferrite with the primary windings encased in Teflon tubing. The pot-core geometry illustrated in Figure B-12 is simple to fabricate. It has reliable voltage isolation since the primary windings are isolated on a bobbin and encapsulated in an insulating material. A disadvantage of the pot-core is its relatively poor frequency response as illustrated in Figure B-13. The phase portion of the figure shows that the transformer is highly inductive since the voltage-current phase is positive. The frequency response curve is generated by using a network analyzer to measure the ratio and phase difference between the current and voltage.

The toroidal geometry illustrated in Figure B-14 has better frequency response characteristics, Figure B-15 because the windings are closely spaced and the ferrite has no gaps. However, the fabrication is more difficult and the high voltage isolation depends on the integrity of the insulating sleeving used to isolate the primary windings.

The impedance of a pulse transformer and its load resistance are,

$$Z = N^2 R_L \quad (B-13)$$

a)



b)

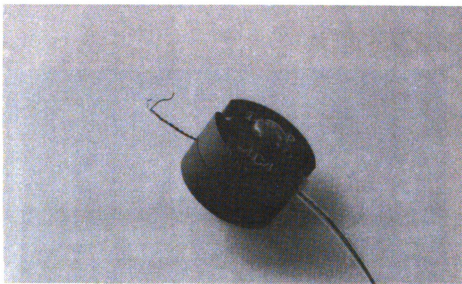


Figure B-12. Photograph of a) bobbin and b) pot-core used to make an isolation pulse transformer.

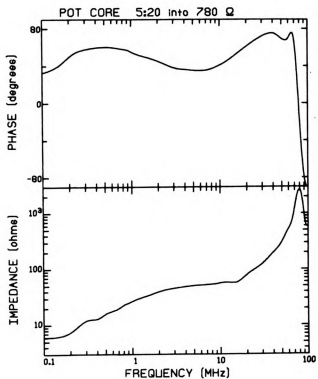


Figure B-13. Frequency and phase response for pot-core transformer

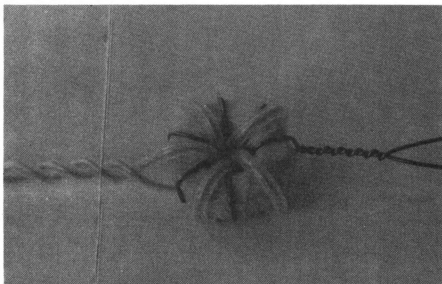


Figure B-14. Photograph of toroidal pulse transformer used in high voltage isolation.

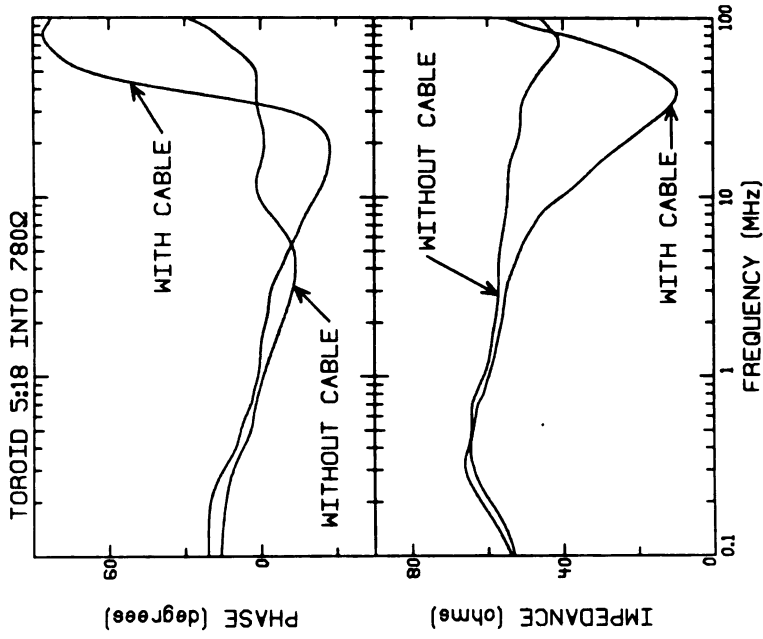


Figure B-15. Frequency response curve for a toroidal pulse transformer for various transformer turn ratios.

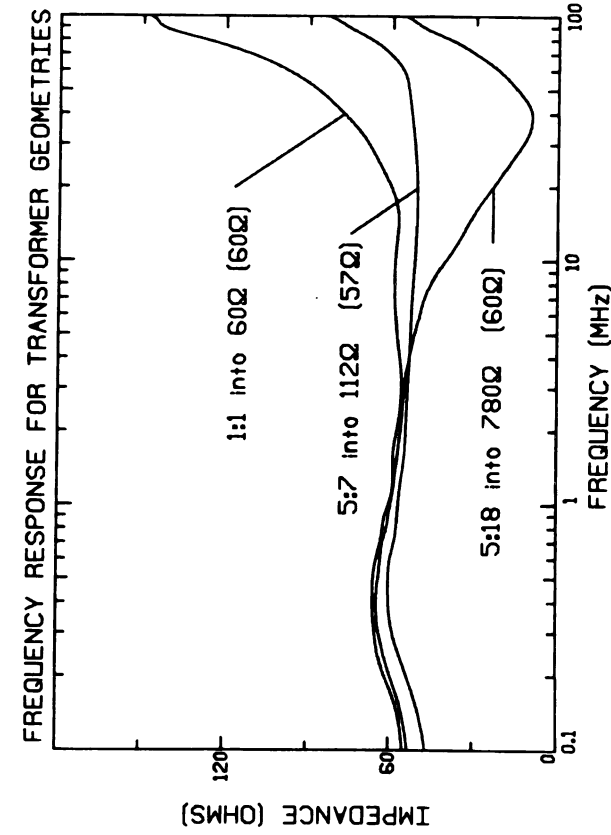


Figure B-16. Frequency and phase response curve showing the effect of additional cable.

where R_L is the load impedance and N is the transformer turns ratio. When considering the frequency response of a transformer, the inductance and capacitance introduced by the transformer leads must be considered. The capacitance dominates at higher frequencies and changes the load impedance. The delay line impedance was chosen to be 50Ω to avoid the differential non-linearities characteristic of higher impedance delay lines. To terminate the delay line a preamplifier impedance of 800Ω and a turns ratio of 1:4 was used. This ratio also gives a four-fold voltage step-up and has a predicted impedance of about 50 Ohms. The impedance of the cable joining the preamp to the transformer becomes approximately 100Ω at high frequencies which results in a very low net impedance (<10 Ohms) at high frequencies. The effect of the coupling cable is readily seen in Figure B-16 showing the impedance and phase for a resistively terminated transformer with and without the coupling cable. Resistive termination has a phase which remains nearly zero. When the coupling cable is added, the termination circuit consists of the reactive impedance due to the cable, and the 780 ohm resistor. The dip in the phase curve above 8 Mhz corresponds to a drop in the impedance. The capacitive impedance of the cable is dominant at this frequency. When the impedance of the cable becomes smaller than that of the resistor the lower impedance dominates, creating a net load impedance which is

much lower than the expected value. The relation for the impedance was used to estimate the turns ratio with the final turns ratio being determined empirically satisfying the criterion of suitable voltage step-up and a relatively flat frequency response curve over the frequency range of interest (Figure B-15).

The pulse transformers used have a turns ratio of 5:7 with a preamp impedance of 110Ω . The pulse transformer windings are wound on the toroid following the winding of a $25 \mu\text{m}$ Teflon film onto the toroid. This film adds some high voltage isolation but its main purpose is to protect the 0.5 mm I.D., 1.0 mm O.D. Teflon tubing which encases the 0.5 mm diameter primary windings. The transformers are vacuum encapsulated using silicone rubber. The resultant transformer network has reliable high voltage isolation and good signal transmission in a compact package.

The delay-line consists of nine 14-pin DIP delay-lines [Da01] connected sequentially. Each chip has 10 taps with a total delay of 50 nsec and a 50Ω impedance. The DIP package is compact and allows considerable flexibility in construction or replacing portions of the delay-line.

The high voltage bias supply network is illustrated in Figure B-17. The $5.6 \text{ M}\Omega$ resistors are for current limitation and the two other resistors serve as a divider network to supply the high voltage to the field shaping planes at the top and bottom of the vacuum box. The capacitor

Figure B-17. Schematic of high voltage supply network.

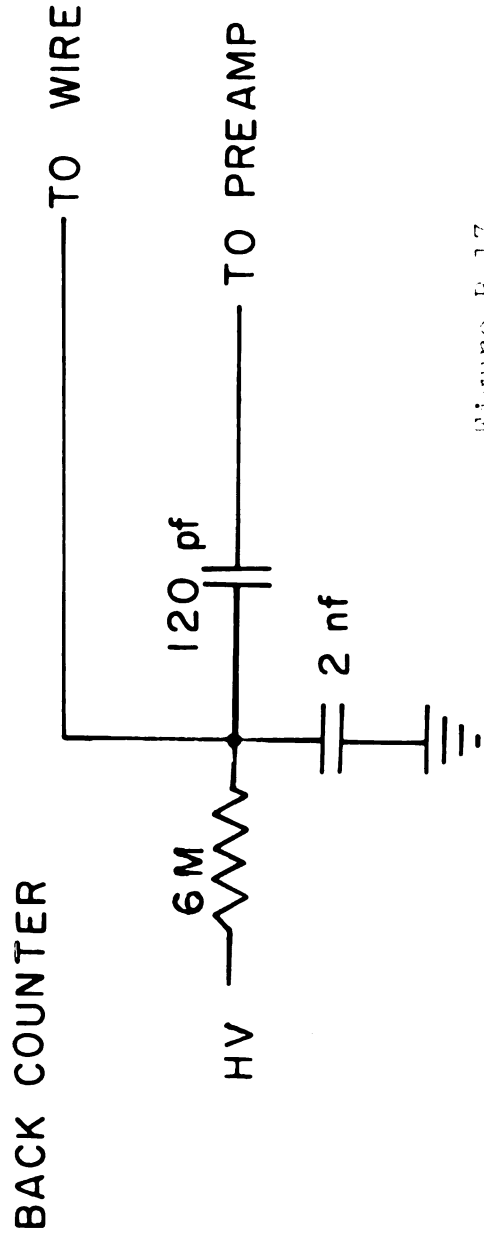
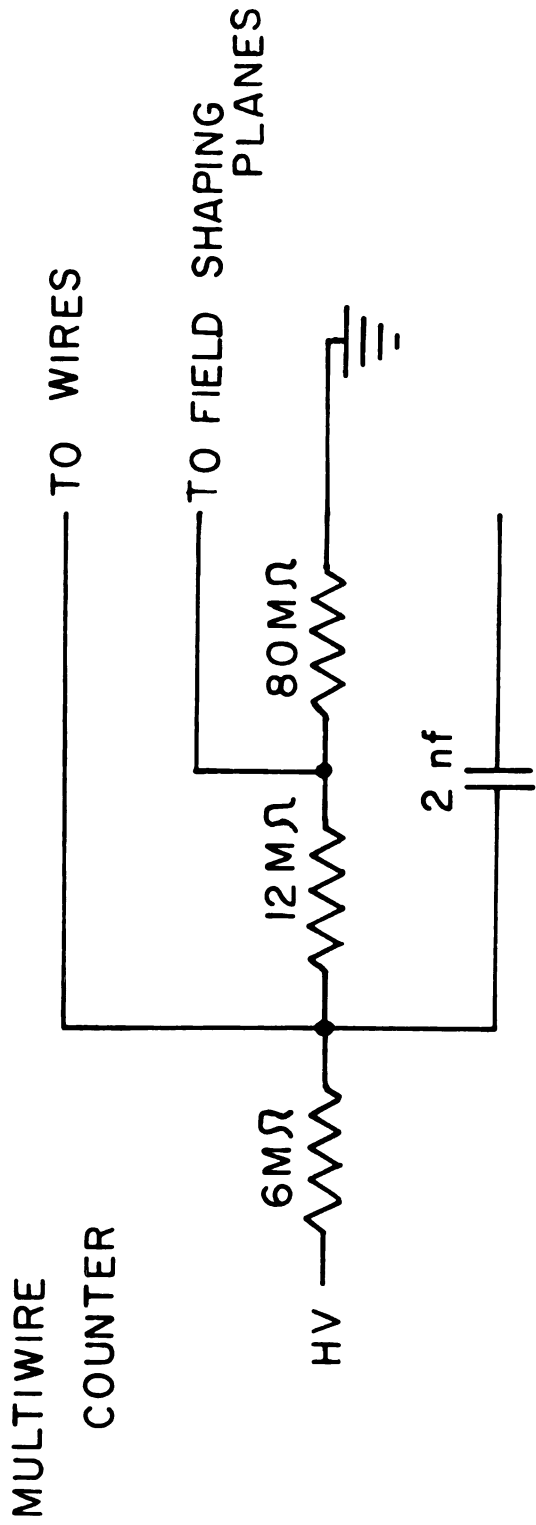


Figure B-17.

supplies a signal coupling to ground and must be able to withstand the high voltages used. Its value is chosen by measuring the other coupling capacitances and using a capacitance large enough to ensure good signal collection.

Using the expression for the gain of a proportional counter (Equation B-14), the amplification of the counter for various geometries and wire diameters can be determined.

$$A = \left[\frac{q}{\pi \epsilon_0 k p d} \right] \frac{2q}{4 \pi \epsilon_0} \frac{\ln 2}{\Delta V} \quad (\text{B-14})$$

where q is the charge per unit length; K is a mobility constant; ΔV is a gain constant; p is the gas pressure; and d is the wire diameter.

The gain is calculated for a single wire in an infinite plane of wires between two grounded conductors. These calculations were done to evaluate the ideal combination of wires to have a low operating voltage with wires that are relatively simple to obtain, install and maintain. This calculation is also necessary to determine the operating voltage required to get suitable gains on the active wires with no appreciable gain on the guard wires. Results of the

calculations for various wire diameters were found in Table B-2. Smaller diameter wires yield comparable gains at lower operating voltages. The tensile strength and durability decrease with the wire diameter. In addition, the cost increases and availability decreases with decreasing size. Problems such as surface non-uniformities and size uniformity become a major consideration for smaller diameter wires.

An additional consideration for the wire diameter choices include the transparency of the counter. Table B-2 lists transparencies which are related to the surface area occupied by the wires in relation to the total active area of the counter. This is important when considering the effects on efficiency as particles which strike the wires would be lost. The guard wires are 50 μm diameter nickel and the active wires were originally 25 μm diameter tungsten but later replaced by 13 μm diameter double-drawn stainless steel. The smaller diameter stainless steel wire was substituted to obtain lower operating voltages and because the tungsten wire surface tends to have irregularities. Rough portions on the wires will produce high field regions resulting in nonuniform gas gains.

Table B-2. Calculated active wire operating voltages, gain ratios, and transparencies for various active and guard wire diameters.

Active Wire Diameter	Active Wire Voltage*	Guard Wire Diameter	Guard/Active Wire Gain Ratio	Transparency
1 mil	7600 Volts	5 mils	1.3×10^{-5}	.953
		3 mils	6.7×10^{-4}	.970
		2 mils	1.0×10^{-2}	.979
.8 mil	7135 Volts	5 mils	1.0×10^{-5}	.954
		3 mils	2.7×10^{-4}	.971
		2 mils	1.0×10^{-3}	.980
		1 mil	4.0×10^{-2}	.988
.5 mil	6320 Volts	5 mils	2.3×10^{-6}	.956
		3 mils	6.7×10^{-5}	.972
		2 mils	6.7×10^{-4}	.981
		1 mil	3.3×10^{-2}	.989

*Voltage required for active wire gain of 3×10^6 .

CONSTRUCTION

A side view of the counter is illustrated in Figure B-18. The wire support frame is made of aluminum with G-10 insulation epoxied into place. The circuit boards for the active wire and delay-line connections are epoxied to the top and bottom of the wire support frame. The active wire board contains the matrix network for the connection of every fifth active wire together. The delay-line board contains the sockets for the 14 pin DIP delay-line chips [Da01] with the necessary interconnections to produce an operating delay line. The wire plane is attached by soldering the wires into place onto pins in the circuit boards. The wire location is maintained by grooves cut into the face of the wire plane support. To insure that the wire plane would be flat and that the wires would be vertical and parallel, the wire plane surface was machined flat and the grooves cut following the final assembly of the wire plane support. The active wires are installed individually by soldering while tensioned using weights. The guard wires are installed as pairs, tensioned with weights to insure uniform tension.

The front ground plane is produced by mounting a 6 μ m aluminized Mylar film onto a G-10 support frame. The frame is held in place against the wire plane support with screws to make disassembly simple. The middle ground plane

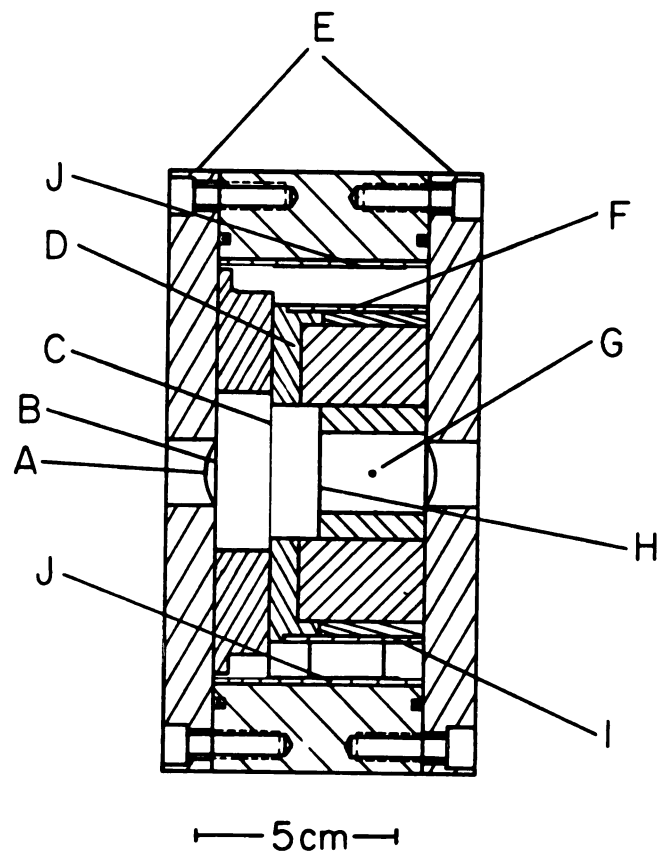


Figure B-18. Schematic cross section of MWPC. Labeled parts are: A) gas windows, B) ground foil, C) wire plane, D) wire support insulation, E) covers, F) active wire matrix circuit board, G) energy loss counter, H) separator foil, I) delay line circuit board, and J) field shaping planes.

which separates the multiwire active region from the energy-loss proportional counter is 12 μm aluminum foil. The foil is glued to the frame of the energy-loss portion which is removable to improve the serviceability of the counter. The energy-loss detector is a single wire proportional counter using a 25 μm stainless steel wire. This section gives a particle energy-loss signal for particle identification.

The outer support and vacuum box is made of aluminum with 12.5 mm aluminum front and back covers with 500 mm by 14 mm entrance and exit ports. The entrance and exit ports are positioned to allow particles with incident angles of 45 degrees to pass through the detector. The gas windows are 6 μm Mylar held in place on O-rings between the covers and gas box frame. The vacuum box has alignment grooves on its lower surface allowing simple and accurate placement in the spectrograph focal plane. Mounting brackets on the back cover allow the attachment of a 50 cm plastic scintillator with light pipe and photomultiplier.

Figure B-19 shows the frontal view of the counter. For maximum utilization of space and to allow the detector to have the active region at the highest possible radius to detect maximum rigidity particles, the electronics are installed at one end of the detector vacuum box. The need to minimize the signal degradation requires the pre-amplifiers to be installed as near as possible to the

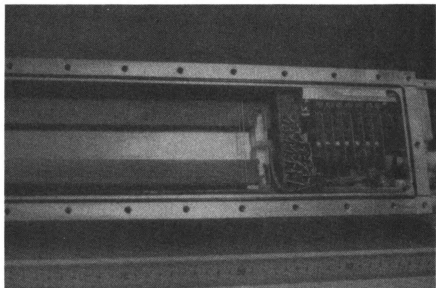


Figure B-19. Photograph showing a portion of the wire plane and the electronics housed in the vacuum box.

isolation transformers. The transformer board is attached to the end of the wire plane frame and the high voltage regions were well separated from the grounded surfaces. The fields at the end of the wire plane are shaped by installing successively larger diameter wires near the ends. The preamplifiers are installed on the upper surface of the vacuum box with the lower region containing the high voltage voltage distribution and current limiting circuitry. The high voltage feedthroughs are made of Teflon and use O-rings to produce a vacuum seal. The preamplifier power and outputs are brought out of the counter using a multi-pin Kovar feedthrough.

A schematic of the electronics used, Figure B-20, shows a relatively simple setup. The amplified timing pulses are discriminated and delayed before processing with the time digitizer. The delay is added to guarantee that the sum (fiducial) start signal arrives first to start the time digitizer. The analog signals are processed using standard coincidence electronics and sent to the computer ADC's. The strobe delay module allows the rejection of a trigger event which produces timing pulses but which does not satisfy the coincidence requirements. The strobe delay module clears the time digitizer and the ADC's if a required coincidence signal does not arrive within a fixed time interval following the time digitizer start signal. This decreases deadtimes caused by the computer processing invalid events.

Figure B-20. Schematic of electronics used with MWPC.
The time digitizer and ADC's are part of a
CAMAC system connected to a PDP 11/45 com-
puter.

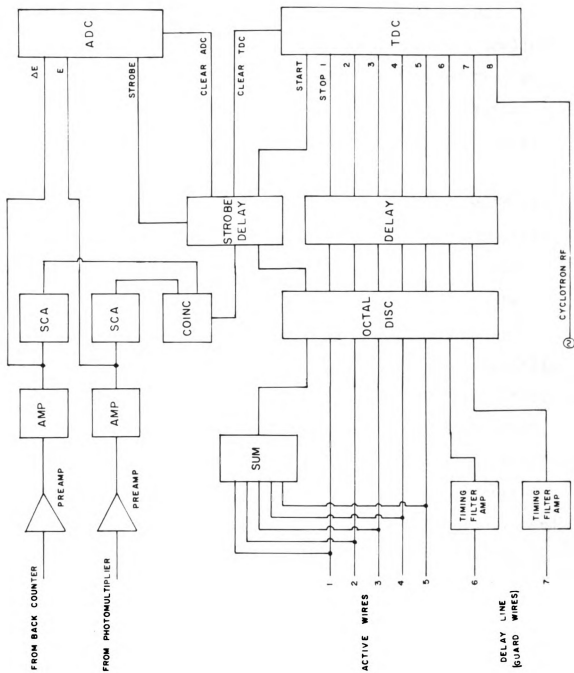


Figure B-20.

RESULTS AND DISCUSSION

A variety of tests were performed with the MWPC. Figure B-21 compares spectra for the MWPC and the inclined cathode delay line counter for protons scattered from a ^{238}U target at 65 and 67.5 degrees. The most dramatic difference is the elimination of the high and low energy tails on the peaks in the spectra from the MWPC.

The tails are caused by effects to which the MWPC is less sensitive. A possible explanation for the symmetric tails is that electrons are scattered by the particles passing through the detector. These electrons may be scattered and liberate charge along the anode wire in standard proportional counters causing a misidentification of the particle position. In the MWPC a portion of these events will cause no problem as the particle track will trigger the active wire discriminators first. If the particle triggers some wires and the electron triggers others an unacceptable particle trajectory will result and the event may be rejected. Another possible mechanism is that of photons propagating along the wire resulting charge multiplication which would result in a broadened particle line. The MWPC should be less sensitive to these mechanisms because the charge collecting wires run perpendicular to the direction of the position being measured. The broadening of the line along the wire should not degrade

Figure B-21. Comparison spectra for MWPC and delay line counter. Spectrum is of protons scattered from a UF_4 target.

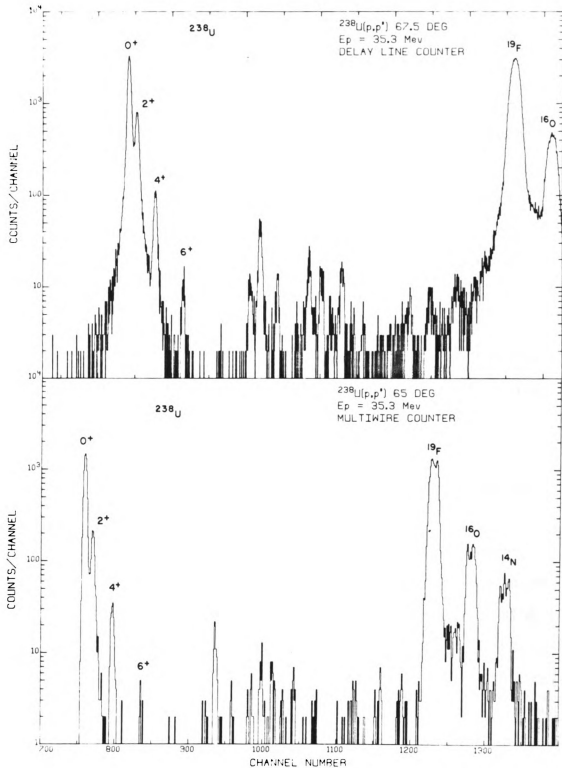


Figure B-21.

the resolution. The most obvious advantage of the reduced tailing is that peak area extraction is easier making the data reduction more reliable. Weak states near strong states may be resolved with ease if the tailing can be eliminated. The resolution in the two spectra is comparable (.3 mm), although no attempt was made to optimize the energy resolution.

Another difference between the spectra in Figure B-21 is the decreased background for the MWPC spectra. The readout mechanism requires more information to produce a valid event leading to better background reduction. An event in either counter must satisfy E , ΔE , and time-of-flight requirements. For an event to be valid in the MWPC it must also produce signal on three adjacent active wires and satisfy angle of incidence requirements. Background producing events such as gamma-rays in coincidence with a particle or particles not scattered in the target can be rejected with greater reliability.

A novel experiment uses the spectrograph and multi-wire counter as a pinhole camera. Figure B-22 illustrates a thick gas cell target and the spectrograph. By knowing the angle of the particles passing through the defining aperture, particles scattered at the window of the gas cell may be eliminated. Figure B-23 contrasts two spectra whose abscissas are the angle of incidence to the MWPC using the gas cell with and without gas. By rejecting the

Figure B-22. Thick gas cell and spectrograph showing relationship between locus of the scattering and the angle of incidence on the detector.

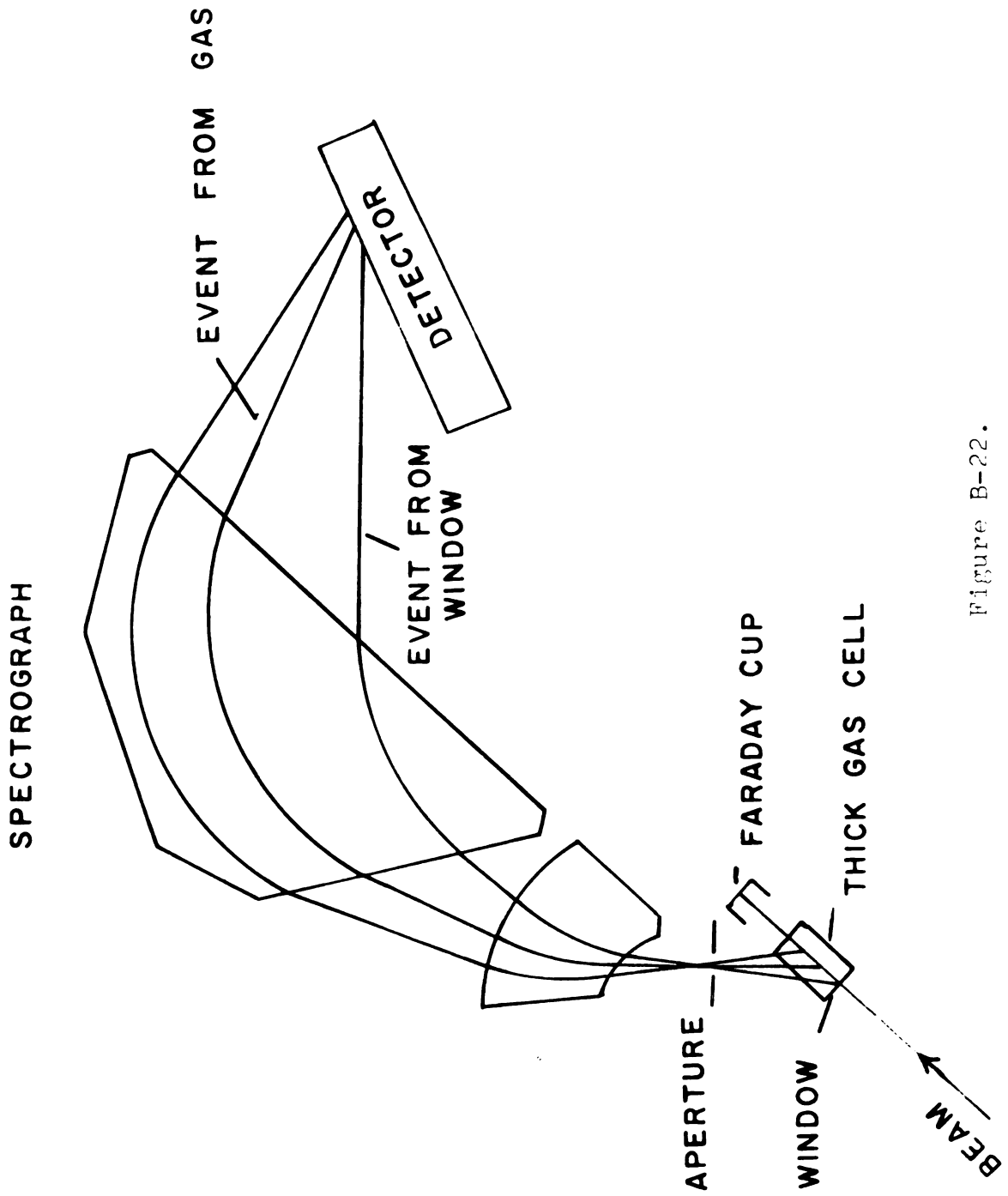
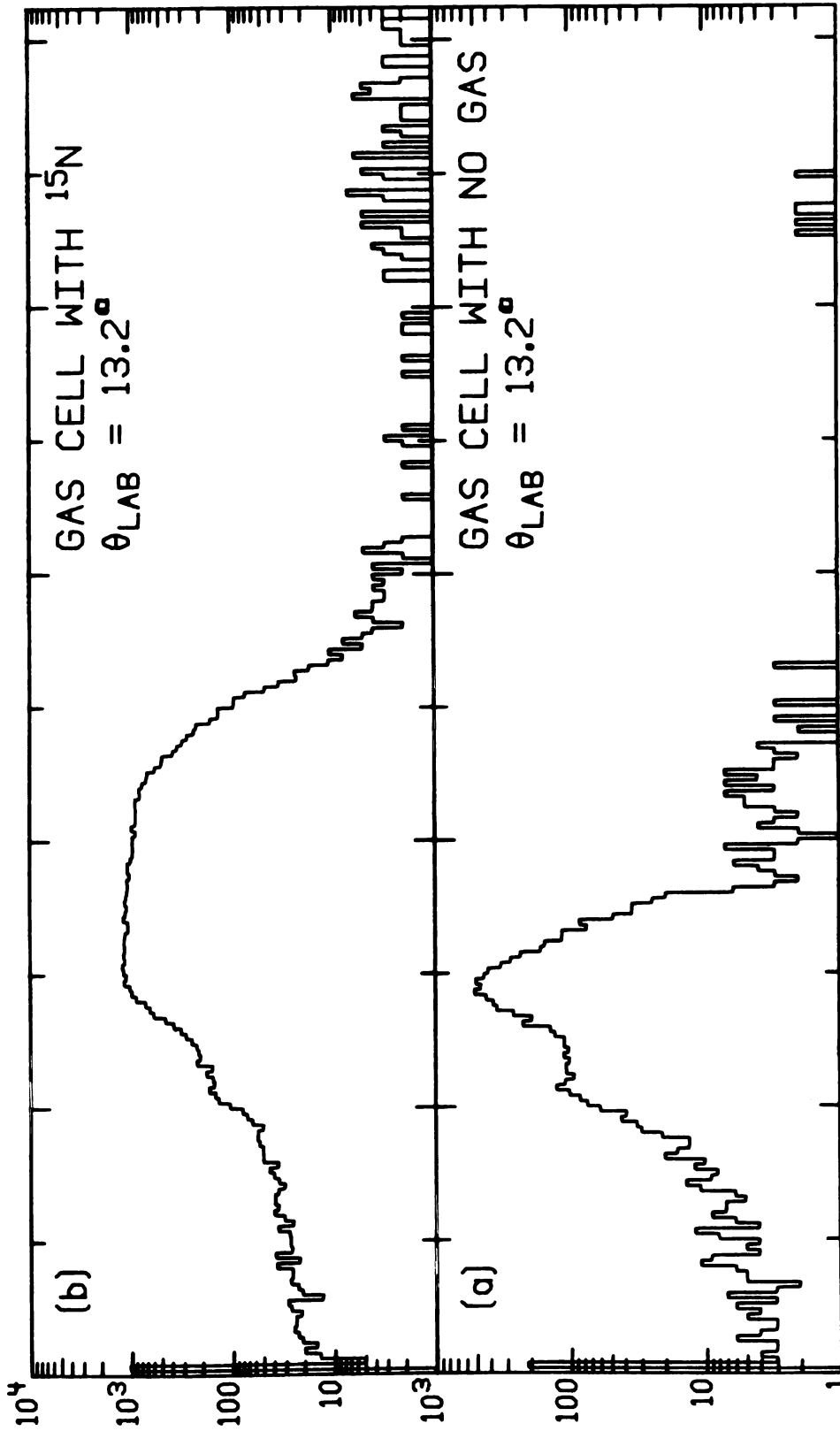


Figure B-22.

Figure B-23. Spectra whose abscissa is angle of incidence on the detector.



ANGLE OF INCIDENCE ON MWPC

Figure B-23.

region of the angle spectrum which corresponds to the events produced in the window, the position (energy) spectrum will only contain events which are the result of reactions or scattering by the gas. Figure B-24 contains spectra illustrating the effect of gating on a range of incident angle. The gated spectra have isolated states which were unresolvable in the ungated spectra.

The MWPC has a more sophisticated type of readout with comparable resolution to other detectors. The design calculations predicted a position resolution of 120 μm FWHM relative to a wire. This results in a position resolution along the counter of less than 200 μm and an angular resolution of .6 degrees. Tests with charged particles yielded an angular resolution of about 1 degree with propane as the proportional gas. Using 'magic' gas, (82.9% argon, 16.85% Isobutane, and .25% Freon) resulted in an angular resolution of about 0.7 degrees. The ultimate position resolution was not verified due to contributions of the beam. Since the angular and position readout are based on the same time measurements the attainable position resolution should match the results of the calculations. There is some evidence for the need to calibrate the delay-line readout to prevent misidentification of the wire nearest the track. The position given by the delay-line readout must be matched with that given for all wires. This requires an accurate determination of any offsets and position nonlinearities.

Figure B-24. Position spectra contrasting the result of gating with angle of incidence on the detector.

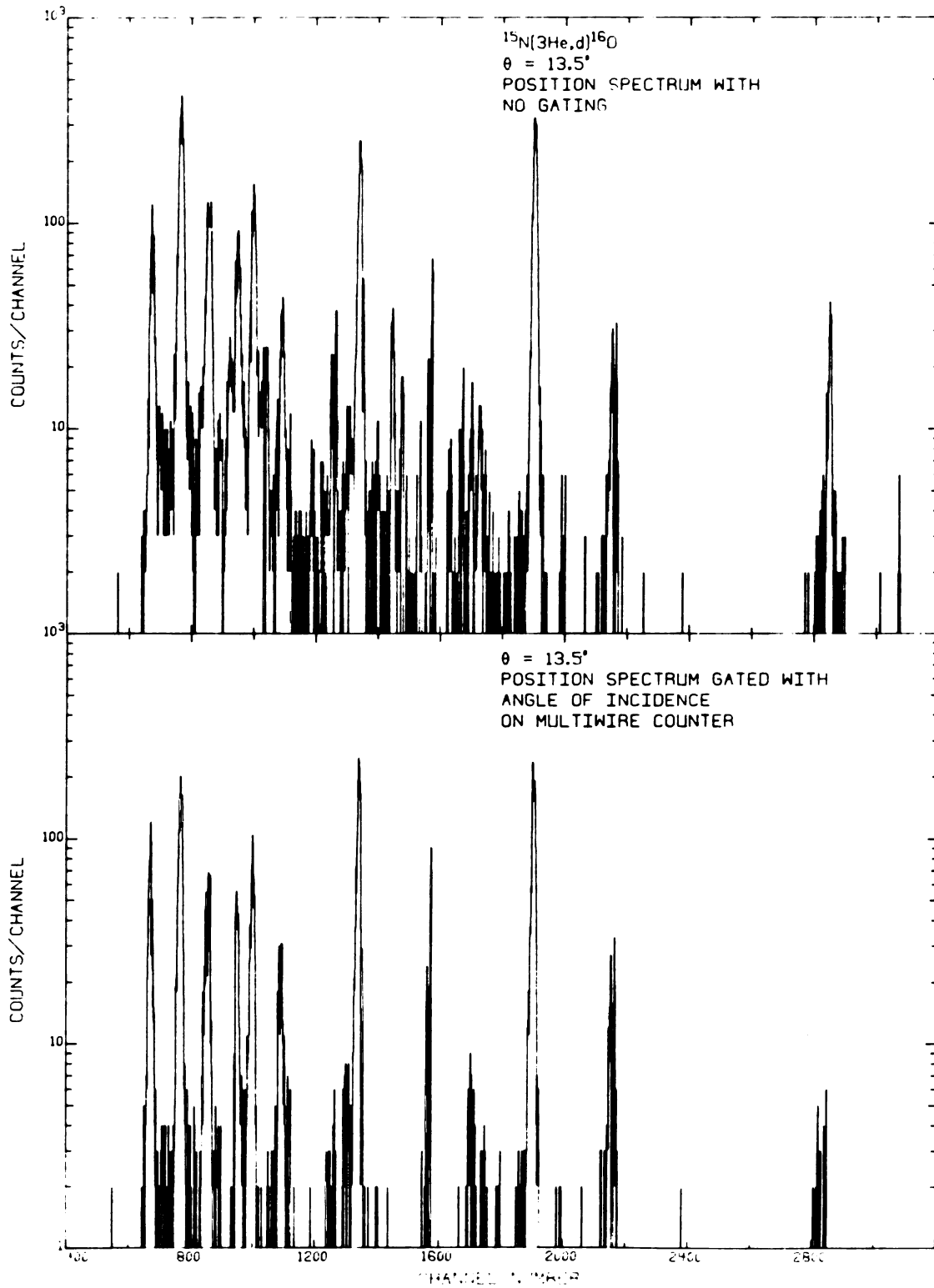


Figure B-24.

APPENDIX C

 $^{232}\text{Th}(p,p)$ 0^+

0 c.m.	$d\sigma/d\Omega$ (mb/str)	Error (mb/str)
20.09	.6502E 04	.2766E 03
22.60	.3346E 04	.1005E 03
25.11	.2019E 04	.8585E 02
27.62	.1097E 04	.3295E 02
30.13	.7110E 03	.2135E 02
32.64	.4261E 03	.1279E 02
35.15	.2901E 03	.8719E 01
37.66	.2152E 03	.6462E 01
40.17	.1871E 03	.5617E 01
42.67	.1573E 03	.4723E 01
45.18	.1173E 03	.3526E 01
47.69	.7476E 02	.2247E 01
50.20	.4342E 02	.1308E 01
52.71	.2212E 02	.6666E 00
55.21	.1621E 02	.6968E 00
57.72	.1881E 02	.5683E 00
60.22	.1936E 02	.5888E 00
62.73	.2299E 02	.6926E 00
65.23	.1815E 02	.7707E 00
67.74	.1296E 02	.3911E 00
70.24	.7406E 01	.3147E 00
72.75	.3749E 01	.1137E 00
75.25	.2267E 01	.9667E-01
77.75	.2591E 01	.7864E-01
80.25	.3302E 01	.1404E 00
82.76	.3692E 01	.1121E 00
85.26	.3858E 01	.1640E 00
87.76	.2899E 01	.8829E-01
90.26	.2167E 01	.9224E-01
92.76	.1143E 01	.3722E-01
95.26	.6995E 00	.2998E-01
97.76	.4302E 00	.1406E-01
100.25	.4647E 00	.1998E-01
102.75	.5784E 00	.1810E-01
105.25	.6474E 00	.2767E-01
107.75	.6648E 00	.2057E-01
110.24	.5848E 00	.1826E-01
112.74	.4901E 00	.1525E-01
115.23	.3173E 00	.1068E-01
117.73	.2148E 00	.7452E-02
120.22	.1356E 00	.4485E-02
125.21	.1179E 00	.4013E-02
130.20	.1398E 00	.5531E-02
135.18	.1253E 00	.4455E-02
140.17	.8152E-01	.3228E-02
144.65	.5165E-01	.2645E-02

$^{232}\text{Th}(p, p')$ 2^+

0 c.m.	$d\sigma/d\Omega$ (mb/str)	Error (mb/str)
20.09	.5611E 02	.5964E 01
22.60	.3547E 02	.3027E 01
25.11	.2874E 02	.6823E 01
27.62	.1141E 02	.7655E 00
30.13	.1184E 02	.8006E 00
32.64	.1549E 02	.5394E 00
35.15	.1762E 02	.6430E 00
37.66	.1589E 02	.5258E 00
40.17	.1246E 02	.4010E 00
42.68	.7909E 01	.2759E 00
45.18	.5121E 01	.1849E 00
47.69	.4477E 01	.1514E 00
50.20	.5469E 01	.1806E 00
52.71	.6368E 01	.2010E 00
55.21	.5996E 01	.2230E 00
57.72	.5190E 01	.1671E 00
60.22	.4414E 01	.1504E 00
62.73	.2332E 01	.8032E-01
65.23	.2047E 01	.8746E-01
67.74	.2335E 01	.7734E-01
70.24	.2510E 01	.1070E 00
72.75	.2745E 01	.8403E-01
75.25	.2242E 01	.9560E-01
77.75	.1641E 01	.5061E-01
80.25	.1248E 01	.5332E-01
82.76	.8064E 00	.2862E-01
85.26	.8097E 00	.3473E-01
87.76	.7350E 00	.2446E-01
90.26	.8957E 00	.3833E-01
92.76	.8465E 00	.2941E-01
95.26	.8480E 00	.3628E-01
97.76	.6277E 00	.1964E-01
100.25	.5439E 00	.2334E-01
102.75	.3737E 00	.1234E-01
105.25	.3177E 00	.1370E-01
107.75	.2734E 00	.9544E-02
110.24	.2869E 00	.9755E-02
112.74	.2988E 00	.9846E-02
115.23	.2782E 00	.9705E-02
117.73	.2572E 00	.8619E-02
120.22	.2257E 00	.7110E-02
125.21	.1740E 00	.5632E-02
130.20	.1396E 00	.5622E-02
135.18	.1177E 00	.4355E-02
140.17	.1044E 00	.3912E-02
144.65	.1089E 00	.4013E-02

$^{232}\text{Th}(p, p')$ 4^+

0 c.m.	$d\sigma/d\Omega$ (mb/str)	Error (mb/str)
30.13	.1784E 01	.9834E-01
32.64	.1364E 01	.6694E-01
35.15	.1028E 01	.5735E-01
37.66	.6575E 00	.3122E-01
40.17	.5447E 00	.2399E-01
42.68	.6902E 00	.3394E-01
45.18	.8335E 00	.3458E-01
47.69	.9576E 00	.3263E-01
50.20	.7912E 00	.2862E-01
52.71	.5818E 00	.2124E-01
55.21	.4358E 00	.1790E-01
57.72	.3795E 00	.1570E-01
60.22	.3542E 00	.1468E-01
62.73	.4768E 00	.1817E-01
65.23	.4658E 00	.2064E-01
67.74	.4573E 00	.1749E-01
70.24	.3585E 00	.1607E-01
72.75	.2724E 00	.9293E-02
75.25	.2030E 00	.9454E-02
77.75	.1707E 00	.5914E-02
80.26	.1865E 00	.8458E-02
82.76	.1800E 00	.7070E-02
85.26	.2204E 00	.9836E-02
87.76	.1834E 00	.6768E-02
90.26	.1777E 00	.7995E-02
92.76	.1245E 00	.5169E-02
95.26	.1145E 00	.5260E-02
97.76	.7757E-01	.2866E-02
100.26	.8957E-01	.4133E-02
102.75	.8287E-01	.2997E-02
105.25	.9095E-01	.4123E-02
107.75	.8722E-01	.3047E-02
110.24	.8247E-01	.2886E-02
112.74	.8223E-01	.2987E-02
115.23	.6227E-01	.2524E-02
117.73	.5137E-01	.2142E-02
120.22	.4127E-01	.1539E-02
125.21	.4012E-01	.1619E-02
130.20	.4260E-01	.1730E-02
135.18	.4070E-01	.1579E-02
140.17	.3722E-01	.1589E-02
144.65	.2963E-01	.1358E-02

$^{232}\text{Th}(p, p')$ 6^+

0 c.m.	$d\sigma/d\Omega$ (mb/str)	Error (mb/str)
42.68	.5436E-01	.1192E-01
45.18	.5304E-01	.5300E-02
47.69	.5539E-01	.4506E-02
50.20	.6728E-01	.4868E-02
52.71	.8263E-01	.4375E-02
55.21	.7243E-01	.4506E-02
57.72	.7266E-01	.3882E-02
60.22	.5040E-01	.2917E-02
62.73	.4452E-01	.3379E-02
65.24	.2804E-01	.3238E-02
67.74	.3488E-01	.2494E-02
70.24	.3512E-01	.3228E-02
72.75	.4734E-01	.2223E-02
75.25	.4482E-01	.3188E-02
77.75	.4236E-01	.1820E-02
80.26	.3691E-01	.2434E-02
82.76	.2682E-01	.1720E-02
85.26	.2443E-01	.1891E-02
87.76	.2115E-01	.1478E-02
90.26	.2296E-01	.1770E-02
92.76	.2583E-01	.1297E-02
95.26	.2789E-01	.1730E-02
97.76	.2486E-01	.1207E-02
100.26	.2395E-01	.1458E-02
102.75	.2215E-01	.1096E-02
105.25	.1780E-01	.1106E-02
107.75	.1771E-01	.8850E-03
110.24	.1465E-01	.7040E-03
112.74	.1632E-01	.8046E-03
115.24	.1670E-01	.8548E-03
117.73	.1534E-01	.8649E-03
120.22	.1496E-01	.6537E-03
125.21	.1429E-01	.6939E-03
130.20	.1252E-01	.6436E-03
135.18	.1126E-01	.5934E-03
140.17	.1082E-01	.5833E-03
144.65	.1072E-01	.5732E-03

$^{232}\text{Th}(p, p')$ 8^+

0 c.m.	$d\sigma/d\Omega$ (mb/str)	Error (mb/str)
50.20	.2075E-01	.3510E-02
52.71	.2616E-01	.2856E-02
55.21	.1373E-01	.3248E-02
57.72	.1799E-01	.1740E-02
60.23	.1474E-01	.1609E-02
62.73	.1369E-01	.1951E-02
65.24	.7402E-02	.2625E-02
67.74	.8247E-02	.1267E-02
70.24	.4666E-02	.2172E-02
72.75	.5692E-02	.7040E-03
75.25	.3641E-02	.1740E-02
77.75	.7100E-02	.6034E-03
80.26	.5712E-02	.1358E-02
82.76	.8750E-02	.9252E-03
85.26	.5642E-02	.1247E-02
87.76	.5582E-02	.7342E-03
90.26	.4837E-02	.1146E-02
92.76	.4234E-02	.4626E-03
95.26	.2967E-02	.7844E-03
97.76	.3148E-02	.3621E-03
100.26	.3148E-02	.6638E-03
102.75	.3118E-02	.3520E-03
105.25	.3258E-02	.5632E-03
107.75	.3600E-02	.3419E-03
110.24	.3379E-02	.3017E-03
112.74	.3359E-02	.3118E-03
115.24	.2715E-02	.3319E-03
117.73	.2514E-02	.3017E-03
120.23	.1871E-02	.1911E-03
125.21	.2464E-02	.2414E-03
130.20	.3379E-02	.2917E-03
135.18	.2575E-02	.2514E-03
140.17	.2142E-02	.2213E-03
144.65	.1740E-02	.2011E-03

$^{234}\text{U}(p,p) \quad 0^+$

0 c.m.	$d\sigma/d\Omega$ (mb/str)	Error (mb/str)
20.09	.7686E 04	.2312E 03
25.11	.2032E 04	.6114E 02
30.13	.7291E 03	.2207E 02
35.15	.3443E 03	.1038E 02
37.66	.2604E 03	.7879E 01
40.16	.1859E 03	.5606E 01
42.67	.1589E 03	.4813E 01
45.18	.1227E 03	.3712E 01
47.69	.7591E 02	.2322E 01
50.20	.4385E 02	.1343E 01
55.21	.1910E 02	.5980E 00
60.22	.2323E 02	.7097E 00
65.23	.1971E 02	.6074E 00
70.24	.8120E 01	.2577E 00
75.25	.3041E 01	.1099E 00
80.25	.4113E 01	.1335E 00
85.26	.4398E 01	.1429E 00
90.26	.2567E 01	.8244E-01
95.26	.8435E 00	.4211E-01
100.25	.5918E 00	.2338E-01
105.25	.8143E 00	.3019E-01
110.24	.7055E 00	.2522E-01
115.23	.3788E 00	.1507E-01
120.22	.2136E 00	.1391E-01
125.21	.1473E 00	.9717E-02
135.18	.1346E 00	.6417E-02
144.65	.6176E-01	.4000E-02

$^{234}\text{U}(p, p')$ 2^+

0 c.m.	$d\sigma/d\Omega$ (mb/str)	Error (mb/str)
20.09	.9095E 02	.1191E 02
25.11	.2708E 02	.2747E 01
30.13	.1576E 02	.1853E 01
35.15	.2440E 02	.1106E 01
37.66	.2101E 02	.8966E 00
40.16	.1183E 02	.5110E 00
42.67	.8374E 01	.4992E 00
45.18	.5782E 01	.4117E 00
47.69	.5278E 01	.3224E 00
50.20	.6708E 01	.3280E 00
55.21	.6708E 01	.2638E 00
60.22	.3432E 01	.1513E 00
65.23	.2384E 01	.1219E 00
70.24	.3134E 01	.1183E 00
75.25	.2951E 01	.1086E 00
80.25	.1458E 01	.5750E-01
85.26	.9804E 00	.4958E-01
90.26	.1098E 01	.4150E-01
95.26	.1030E 01	.4725E-01
100.25	.6892E 00	.2554E-01
105.25	.4154E 00	.2130E-01
110.24	.3654E 00	.1568E-01
115.23	.3766E 00	.1511E-01
120.22	.3546E 00	.1655E-01
125.21	.2356E 00	.9889E-02
135.18	.1586E 00	.7219E-02
144.65	.1566E 00	.7463E-02

$^{234}\text{U}(p, p')$ 4^+

0 c.m.	$d\sigma/d\Omega$ (mb/str)	Error (mb/str)
30.13	.1626E 01	.2988E 00
35.15	.1283E 01	.8989E-01
37.66	.9552E 00	.8730E-01
40.16	.5833E 00	.5597E-01
42.67	.8779E 00	.6538E-01
45.18	.1097E 01	.5946E-01
47.69	.1118E 01	.6560E-01
50.20	.1028E 01	.5223E-01
55.21	.4451E 00	.3221E-01
60.22	.4269E 00	.2425E-01
65.23	.5505E 00	.2978E-01
70.24	.4662E 00	.2745E-01
75.25	.2590E 00	.2056E-01
80.25	.2349E 00	.1436E-01
85.26	.2916E 00	.1688E-01
90.26	.2058E 00	.1021E-01
95.26	.1422E 00	.9422E-02
100.25	.1263E 00	.7463E-02
105.25	.1296E 00	.7493E-02
110.24	.1095E 00	.6407E-02
115.23	.8140E-01	.5290E-02
120.22	.7464E-01	.4782E-02
125.21	.5878E-01	.3909E-02
135.18	.5937E-01	.3807E-02
144.65	.5156E-01	.3706E-02

$^{234}\text{U}(p, p')$ 6^+

0 c.m.	$d\sigma/d\Omega$ (mb/str)	Error (mb/str)
45.18	.2143E 00	.2315E-01
50.20	.1003E 00	.1459E-01
55.21	.8522E-01	.1157E-01
60.22	.6349E-01	.8072E-02
65.23	.5488E-01	.8915E-02
70.24	.4955E-01	.7544E-02
75.25	.7095E-01	.8397E-02
80.25	.4574E-01	.5889E-02
85.26	.3466E-01	.5402E-02
90.26	.3142E-01	.3320E-02
95.26	.4737E-01	.5046E-02
100.25	.3786E-01	.3706E-02
105.25	.2812E-01	.3097E-02
110.24	.2703E-01	.2853E-02
115.23	.2453E-01	.2660E-02
120.22	.2586E-01	.2620E-02
125.21	.2451E-01	.2366E-02
135.18	.1998E-01	.2031E-02
144.65	.1718E-01	.2010E-02

 $^{234}\text{U}(p, p')$ 8^+

0 c.m.	d/d (mb/str)	Error (mb/str)
50.20	.4336E-01	.1011E-01
55.21	.2945E-01	.7980E-02
60.22	.2614E-01	.5483E-02
65.23	.1546E-01	.5300E-02
70.24	.2039E-01	.5300E-02
80.25	.1317E-01	.3472E-02
85.26	.1863E-01	.4153E-02
90.26	.1089E-01	.2183E-02
95.26	.6366E-02	.1787E-02
100.25	.4569E-02	.1218E-02
105.25	.6559E-02	.1472E-02
110.24	.6559E-02	.1371E-02
115.23	.3229E-02	.9443E-03
120.22	.5452E-02	.1168E-02
125.21	.4478E-02	.9849E-03
135.18	.2853E-02	.7513E-03
144.65	.3300E-02	.8630E-03

$^{236}\text{U}(p,p)$ 0^+

0 c.m.	$d\sigma/d\Omega$ (mb/str)	Error (mb/str)
20.09	.7291E 04	.2189E 03
25.11	.1983E 04	.6005E 02
27.62	.1245E 04	.3744E 02
30.13	.7090E 03	.2180E 02
32.64	.4283E 03	.1292E 02
35.15	.2857E 03	.8609E 01
37.65	.2333E 03	.7031E 01
40.16	.1920E 03	.5770E 01
42.67	.1630E 03	.4906E 01
45.18	.1127E 03	.3407E 01
47.69	.7720E 02	.2329E 01
50.19	.4180E 02	.1270E 01
52.70	.2437E 02	.7456E 00
55.21	.1758E 02	.5478E 00
60.22	.2170E 02	.6685E 00
65.23	.1926E 02	.6007E 00
70.24	.7803E 01	.2436E 00
75.24	.2541E 01	.9233E-01
80.25	.3405E 01	.1089E 00
85.25	.3831E 01	.1200E 00
90.25	.1993E 01	.6356E-01
95.25	.6377E 00	.2445E-01
100.25	.5458E 00	.2072E-01
105.24	.6862E 00	.2337E-01
110.24	.5986E 00	.2030E-01
115.23	.3408E 00	.1289E-01
120.22	.1560E 00	.6610E-02
125.21	.1186E 00	.7645E-02
130.19	.1315E 00	.5863E-02
135.18	.1195E 00	.5047E-02
140.16	.5974E-01	.3395E-02
144.65	.3911E-01	.2369E-02

$^{236}\text{U}(p, p')$ 2^+

0 c.m.	$d\sigma/d\Omega$ (mb/str)	Error (mb/str)
20.09	.4474E 02	.1291E 02
25.11	.2946E 02	.6565E 01
27.62	.1187E 02	.2452E 01
30.13	.1254E 02	.4373E 01
32.64	.1500E 02	.8082E 00
35.15	.1752E 02	.8414E 00
37.65	.1756E 02	.6492E 00
40.16	.1367E 02	.4895E 00
42.67	.8911E 01	.3824E 00
45.18	.6842E 01	.3663E 00
47.69	.5825E 01	.2446E 00
50.20	.5923E 01	.2619E 00
52.70	.7445E 01	.2623E 00
55.21	.6875E 01	.2493E 00
60.22	.3786E 01	.1863E 00
65.23	.2134E 01	.1438E 00
70.24	.2797E 01	.1042E 00
75.24	.2656E 01	.9542E-01
80.25	.1379E 01	.5532E-01
85.25	.8782E 00	.3725E-01
90.25	.9745E 00	.3509E-01
95.25	.8936E 00	.3126E-01
100.25	.6597E 00	.2403E-01
105.24	.3756E 00	.1462E-01
110.24	.3544E 00	.1421E-01
115.23	.3720E 00	.1337E-01
120.22	.2952E 00	.1042E-01
125.21	.2000E 00	.9049E-02
130.19	.1535E 00	.6083E-02
135.18	.1299E 00	.5246E-02
140.16	.9141E-01	.4002E-02
144.65	.9528E-01	.3932E-02

$^{236}\text{U}(p, p')$ 4^+

0 c.m.	$d\sigma/d\Omega$ (mb/str)	Error (mb/str)
35.15	.9648E 00	.7808E-01
37.65	.5362E 00	.4225E-01
40.16	.5654E 00	.3851E-01
42.67	.8090E 00	.4216E-01
45.18	.7856E 00	.6998E-01
47.69	.9110E 00	.4074E-01
50.20	.6263E 00	.4427E-01
52.70	.4557E 00	.2441E-01
55.21	.3504E 00	.2415E-01
60.22	.3462E 00	.1987E-01
65.23	.4926E 00	.2722E-01
70.24	.3347E 00	.1871E-01
75.24	.1920E 00	.1161E-01
80.25	.1659E 00	.1047E-01
85.25	.2173E 00	.1292E-01
90.25	.1603E 00	.7446E-02
95.25	.9084E-01	.6331E-02
100.25	.9453E-01	.6182E-02
105.24	.1013E 00	.5077E-02
110.24	.9599E-01	.4221E-02
115.23	.7742E-01	.3863E-02
120.22	.5822E-01	.2947E-02
125.21	.4184E-01	.2359E-02
130.20	.4750E-01	.2459E-02
135.18	.4763E-01	.2459E-02
140.16	.3335E-01	.1881E-02
144.65	.3131E-01	.1822E-02

$^{236}\text{U}(p, p')$ 6^+

0 c.m.	$d\sigma/d\Omega$ (mb/str)	Error (mb/str)
45.18	.1111E 00	.1644E-01
47.69	.9836E-01	.1257E-01
50.20	.8052E-01	.1152E-01
55.21	.6586E-01	.9109E-02
60.22	.4074E-01	.7118E-02
65.23	.2853E-01	.7138E-02
70.24	.4503E-01	.6560E-02
75.25	.4712E-01	.5704E-02
80.25	.3098E-01	.4131E-02
85.25	.1790E-01	.3006E-02
90.26	.2801E-01	.2797E-02
95.25	.2635E-01	.2389E-02
100.25	.2853E-01	.2648E-02
105.25	.1561E-01	.1662E-02
110.24	.2059E-01	.1593E-02
115.23	.1826E-01	.1513E-02
120.22	.2132E-01	.1623E-02
125.21	.1640E-01	.1354E-02
130.20	.1077E-01	.1015E-02
135.18	.1318E-01	.1135E-02
140.16	.1060E-01	.9656E-03
144.65	.7695E-02	.9258E-03

 $^{236}\text{U}(p, p')$ 8^+

0 c.m.	d/d (mb/str)	Error (mb/str)
55.21	.1062E-01	.4500E-02
60.22	.5286E-02	.3415E-02
70.24	.2290E-02	.1921E-02
75.25	.4938E-02	.2240E-02
80.25	.5903E-02	.2379E-02
85.25	.1290E-01	.2718E-02
90.26	.5744E-02	.1334E-02
95.25	.1692E-02	.6272E-03
100.25	.3634E-02	.9258E-03
105.25	.2598E-02	.6869E-03
110.24	.2827E-02	.5973E-03
115.23	.2977E-02	.6172E-03
120.22	.2280E-02	.5276E-03
125.21	.2051E-02	.4679E-03
130.20	.1234E-02	.4181E-03
135.18	.2320E-02	.4679E-03
140.16	.1543E-02	.3783E-03
144.65	.5575E-03	.2489E-03

$^{238}\text{U}(p,p) \quad 0^+$

θ c.m.	$d\sigma/d\Omega$ (mb/str)	Error (mb/str)
20.09	.6701E 04	.2031E 03
22.60	.3557E 04	.1068E 03
25.11	.1875E 04	.5669E 02
27.62	.1103E 04	.3315E 02
30.13	.6606E 03	.1990E 02
32.63	.4181E 03	.1259E 02
35.14	.2890E 03	.8675E 01
37.65	.2268E 03	.6836E 01
40.16	.1859E 03	.5580E 01
42.67	.1432E 03	.4321E 01
45.18	.1078E 03	.3238E 01
47.69	.6840E 02	.2067E 01
50.19	.3751E 02	.1130E 01
52.70	.2336E 02	.7102E 00
55.21	.1741E 02	.5254E 00
57.71	.1908E 02	.5815E 00
60.22	.2114E 02	.6371E 00
62.72	.1921E 02	.5811E 00
65.23	.1595E 02	.4816E 00
67.73	.1113E 02	.3356E 00
70.24	.5860E 01	.1785E 00
72.74	.3268E 01	.1026E 00
75.24	.2108E 01	.6564E-01
77.75	.2500E 01	.7807E-01
80.25	.3083E 01	.9486E-01
82.75	.3488E 01	.1062E 00
85.25	.3157E 01	.9706E-01
87.75	.2496E 01	.7615E-01
90.25	.1538E 01	.4848E-01
92.75	.9535E 00	.2997E-01
95.25	.5079E 00	.1716E-01
97.75	.4082E 00	.1350E-01
100.25	.4353E 00	.1469E-01
102.75	.5380E 00	.1783E-01
105.24	.5959E 00	.1953E-01
107.74	.5931E 00	.1908E-01
110.24	.4835E 00	.1524E-01
112.73	.3658E 00	.1207E-01
115.23	.2403E 00	.7980E-02
117.72	.1711E 00	.6250E-02
120.22	.1173E 00	.3810E-02
125.21	.1114E 00	.4610E-02
130.19	.1091E 00	.4780E-02
135.18	.9938E-01	.3990E-02
140.16	.6389E-01	.3750E-02
144.65	.4075E-01	.2150E-02

$^{238}\text{U}(p, p')$ 2^+

θ c.m.	$d\sigma/d\Omega$ (mb/str)	Error (mb/str)
20.09	.6054E 02	.6322E 01
22.60	.4930E 02	.2573E 01
25.11	.2434E 02	.1883E 01
27.62	.1667E 02	.1835E 01
30.13	.1521E 02	.6992E 00
32.63	.1641E 02	.9122E 00
35.14	.2147E 02	.6527E 00
37.65	.1787E 02	.6886E 00
40.16	.1504E 02	.4558E 00
42.67	.8524E 01	.5281E 00
45.18	.6677E 01	.2042E 00
47.69	.5602E 01	.2970E 00
50.19	.6882E 01	.2109E 00
52.70	.8023E 01	.2513E 00
55.21	.6992E 01	.2129E 00
57.71	.5554E 01	.1958E 00
60.22	.3782E 01	.1164E 00
62.72	.2362E 01	.1004E 00
65.23	.2250E 01	.7048E-01
67.73	.2524E 01	.8104E-01
70.24	.2865E 01	.8862E-01
72.74	.2888E 01	.9176E-01
75.24	.2405E 01	.7459E-01
77.75	.1972E 01	.6305E-01
80.25	.1270E 01	.4047E-01
82.75	.9763E 00	.3450E-01
85.25	.8544E 00	.2797E-01
87.75	.8942E 00	.2888E-01
90.25	.9776E 00	.3046E-01
92.75	.1002E 01	.3138E-01
95.25	.8870E 00	.2857E-01
97.75	.7740E 00	.2397E-01
100.25	.5735E 00	.1886E-01
102.75	.4582E 00	.1570E-01
105.24	.3645E 00	.1254E-01
107.74	.3148E 00	.1184E-01
110.24	.3328E 00	.1093E-01
112.73	.3454E 00	.1131E-01
115.23	.3418E 00	.1097E-01
117.72	.3138E 00	.1024E-01
120.22	.2700E 00	.8360E-02
125.21	.1959E 00	.6800E-02
130.19	.1565E 00	.5490E-02
135.18	.1289E 00	.4630E-02
140.16	.1218E 00	.4860E-02
144.65	.1189E 00	.4240E-02

$^{238}\text{U}(p, p')$ 4^+

0 c.m.	$d\sigma/d\Omega$ (mb/str)	Error (mb/str)
30.13	.1447E 01	.1543E 00
32.63	.7517E 00	.1153E 00
35.15	.6230E 00	.5114E-01
37.65	.3691E 00	.5276E-01
40.16	.5299E 00	.2528E-01
42.67	.6766E 00	.3858E-01
45.18	.7070E 00	.2707E-01
47.69	.6762E 00	.3388E-01
50.19	.5006E 00	.1940E-01
52.70	.4011E 00	.2030E-01
55.21	.2492E 00	.1016E-01
57.71	.2295E 00	.1450E-01
60.22	.3101E 00	.1196E-01
62.72	.3561E 00	.1856E-01
65.23	.4075E 00	.1496E-01
67.73	.3453E 00	.1193E-01
70.24	.2602E 00	.1017E-01
72.74	.1732E 00	.7170E-02
75.24	.1434E 00	.6300E-02
77.75	.1410E 00	.5850E-02
80.25	.1674E 00	.7060E-02
82.75	.1765E 00	.6590E-02
85.25	.1873E 00	.7690E-02
87.75	.1717E 00	.6370E-02
90.25	.1405E 00	.5030E-02
92.75	.1119E 00	.4040E-02
95.25	.7790E-01	.3870E-02
97.75	.7836E-01	.2980E-02
100.25	.7785E-01	.3680E-02
102.75	.8973E-01	.3720E-02
105.24	.8421E-01	.3890E-02
107.74	.8825E-01	.3650E-02
110.24	.8220E-01	.3240E-02
112.73	.7347E-01	.3120E-02
115.23	.5910E-01	.2400E-02
117.72	.5014E-01	.2050E-02
120.22	.4473E-01	.1590E-02
125.21	.4744E-01	.2090E-02
130.19	.4831E-01	.2120E-02
135.18	.4409E-01	.1990E-02
140.16	.4039E-01	.1810E-02
144.65	.3592E-01	.1650E-02

$^{238}\text{U}(p,p')$ 6^+		
0 c.m.	$d\sigma/d\Omega$ (mb/str)	Error (mb/str)
40.16	.9201E-01	.8830E-02
42.67	.8689E-01	.7500E-02
45.18	.9275E-01	.1711E-01
47.69	.1153E 00	.8820E-02
50.19	.8641E-01	.6620E-02
52.70	.7515E-01	.7000E-02
55.21	.4616E-01	.3270E-02
57.71	.3304E-01	.3250E-02
60.22	.3116E-01	.2340E-02
62.72	.2799E-01	.3010E-02
65.23	.4396E-01	.3120E-02
67.73	.3790E-01	.2120E-02
70.24	.5165E-01	.3290E-02
72.74	.4868E-01	.2670E-02
75.24	.5035E-01	.3120E-02
77.75	.3685E-01	.2350E-02
80.25	.3376E-01	.2450E-02
82.75	.2315E-01	.1510E-02
85.25	.2338E-01	.1980E-02
87.75	.2612E-01	.1630E-02
90.25	.2685E-01	.1290E-02
92.75	.3070E-01	.1510E-02
95.25	.2987E-01	.2110E-02
97.75	.2681E-01	.1300E-02
100.25	.1967E-01	.1550E-02
102.75	.1821E-01	.1160E-02
105.24	.1651E-01	.1400E-02
107.74	.1525E-01	.1140E-02
110.24	.1423E-01	.9100E-03
112.73	.1555E-01	.9200E-03
115.23	.1537E-01	.9500E-03
117.72	.1747E-01	.9300E-03
120.22	.1575E-01	.6800E-03
125.21	.1379E-01	.9300E-03
130.19	.1161E-01	.8400E-03
135.18	.1114E-01	.8200E-03
140.16	.1329E-01	.8700E-03
144.65	.1232E-01	.8200E-03

$^{238}\text{U}(p, p')$ 8^+

0 c.m.	$d\sigma/d\Omega$ (mb/str)	Error (mb/str)
45.18	.2075E-01	.4320E-02
47.69	.1796E-01	.3640E-02
50.19	.2644E-01	.4570E-02
52.70	.1293E-01	.3060E-02
55.21	.1340E-01	.1650E-02
57.71	.8470E-02	.1780E-02
60.22	.6290E-02	.1090E-02
62.73	.9410E-02	.1780E-02
65.23	.7490E-02	.1190E-02
67.73	.6100E-02	.8300E-03
70.24	.8160E-02	.1180E-02
72.74	.6510E-02	.8900E-03
75.24	.1074E-01	.1300E-02
77.75	.7100E-02	.9800E-03
80.25	.9260E-02	.1200E-02
82.75	.7520E-02	.8100E-03
85.25	.5440E-02	.9100E-03
87.75	.3900E-02	.6200E-03
90.25	.3540E-02	.7300E-03
92.75	.2430E-02	.3700E-03
95.25	.2720E-02	.5600E-03
97.75	.3270E-02	.3900E-03
100.25	.2250E-02	.4900E-03
102.75	.3510E-02	.4700E-03
105.24	.2720E-02	.5400E-03
107.74	.2990E-02	.4800E-03
110.24	.2290E-02	.3300E-03
112.73	.2160E-02	.3100E-03
115.23	.2410E-02	.3400E-03
117.73	.2470E-02	.3100E-03
120.22	.1870E-02	.1800E-03
125.21	.2210E-02	.3400E-03
130.19	.2480E-02	.3600E-03
135.18	.1870E-02	.3200E-03
140.16	.2000E-02	.3100E-03
144.65	.1480E-02	.2600E-03

REFERENCES

REFERENCES

- [Ba79] G. C. Ball, Nucl. Inst. and Meth. 162, 263 (1979).
- [Bc742] M. Brack, T. Ledergerber, H. C. Pauli, and A. S. Jensen, Nucl. Phys. A234, 185(1974).
- [Be68] G. F. Bertsch, Phys. Lett. 26B, 130(1968).
- [Be69] F. D. Becchetti and G. W. Greenlees, Phys. Rev. 182, 1190(1969).
- [Be73] C. E. Bemis, Jr. et al., Phys. Rev. C 8, 1466(1973).
- [Be77] W. Bertozzi et al., Nucl. Inst. and Meth. 141, 457(1977).
- [Bk76] M. Birk, A. Breskin, and N. Trautner, Nucl. Inst. and Meth. 137, 393(1976).
- [Bl71] H. G. Blosser, G. M. Crawley, R. DeForest, E. Kashy, and B. H. Wildenthal, Nucl. Inst. and Meth. 91, 61(1971).
- [Br74] K. L. Brown, F. Rothacker, D. C. Carey, Ch. Iselin, NAL-91 2041.000(1974).
- [Ch70] G. Charpak, Ann. Rev. Nucl. Sci. 20, 195(1970).
- [Co59] B. L. Cohen, Rev. Sci. Inst. 30, 415(1959).
- [Co76] T. Cooper, W. Bertozzi, J. Heisenberg, S. Kowalski, W. Turchinets, C. Williamson, L. Cardman, S. Fivozinsky, J. Lightbody, Jr., and S. Penner., Phys. Rev. C 13, 1083(1976).
- [Da01] Data Delay Devices, Inc., 253 Crooks Ave., Clifton, New Jersey, 07011.
- [Da76] P. David, J. Debrus, H. Essen, F. Lubke, H. Mommsen, R. Schoenmackers, W. Soyez, H. V. v. Geramb, and E. F. Hefter, Z. Physik A278, 281(1976).
- [Dv78] H. David and R. Fox, program SCOPEFIT, unpublished.

- [Er72] G. A. Erskine, Nucl. Inst. and Meth. 105, 565(1972).
- [Ev72] P. Rice Evans, Spark, Streamer, Proportional, and Drift Chambers (Richelieu Press, London 1977).
- [Gl67] N. K. Glendenning, Proc. Int. School of Physics "Enrico Fermi", Course 40 (1967) ed. M. Jean and R. H. Ricci, Academic Press, New York, 1969, p. 332.
- [Gr68] G. W. Greenlees, J. G. Pyle, Y. C. Tang, Phy. Rev. 171, 1115(1968).
- [He68] D. L. Hendrie, N. K. Glendenning, B. G. Harvey, O. N. Jarvis, H. H. Duhm, J. Sandinos, and J. Mahoney, Phys. Lett. 26B, 127(1968).
- [He73] D. L. Hendrie, B. G. Harvey, J. R. Meriwether, J. Mahoney, J. C. Faivre, and D. G. Kovar, Phys. Rev. Lett. 30, 571(1973).
- [Ho63] P. E. Hodgson, The Optical Model and Elastic Scattering (Oxford Univ. Press (Clarendon) London and New York, 1963).
- [Ho71] P. E. Hodgson, Nuclear Reactions and Nuclear Structure (Clarendon Press, Oxford, 1971).
- [Ko68] G. A. Korn and T. M. Korn, Mathematical Handbook for Scientists and Engineers (McGraw-Hill, New York, 1968).
- [Ki79] C. H. King, J. E. Finck, G. M. Crawley, J. A. Nolen, Jr., and R. M. Ronningen, Phys. Rev. C 20, 2084(1979).
- [Lo70] K. E. G. Lobner, M. Uetter, and V. Honig, Nucl. Data Tables A7, 495(1970).
- [Ma76] R. S. Mackintosh, Nucl. Phys. A266, 379(1976).
- [Ma77] R. S. Mackintosh, Rep. Prog. Phys. 40, 731(1977).
- [Ma78] R. S. Mackintosh, Nucl. Phys. A307, 365(1978).
- [Me79] R. C. Melin, R. M. Ronningen, J. A. Nolen, Jr., and G. M. Crawley, Michigan State University Cyclotron Annual Report (1978-1979), p. 94.
- [Mk75] R. G. Markham and R. G. H. Robertson, Nucl. Inst. and Meth. 129, 131(1975).
- [Mo71] J. M. Moss, Y. D. Terrien, R. M. Lombard, C. Brassard, J. M. Loiseaux, and F. Resmini, Phys. Rev. Lett. 26, 1488(1971).

- [Mo74] P. Moller, S. G. Nilsson, and J. R. Nix, Nucl. Phys. A229, 292(1974).
- [MS70] P. Marmier and E. Sheldon, Physics of Nuclei and Particles Vol. II (Academic Press, New York and London, 1970).
- [Mu67] P. V. Ramana-Murthy and G. D. Demeester, Nucl. Inst. and Meth. 56, 93(1967).
- [Mu71] R. A. Muller, S. E. Derenzo, G. Smadja, D. B. Smith, R. G. Smits, H. Zaklad, and L. W. Alvarez, Phys. Rev. Lett. 27, 532(1971).
- [Ne74] B. Nerlo-Pomorska, Inst. Nuclear Physics Report, INR1538/VII/PL/B, Warsaw (1974).
- [Ne76] B. Nerlo-Pomorska, Nucl. Phys. A259, 481(1976).
- [Ni69] S. G. Nilsson, C. F. Tsang, A. Sobiczewski, Z. Szymanski, S. Wycech, C. Gustafson, I. Lamm, P. Moller, and B. Nilsson, Nucl. Phys. A131, 1(1969).
- [No74] J. A. Nolen, Jr., and P. S. Miller, Bull. Am. Phys. Soc. 19, 1026 (1974).
- [No78] J. A. Nolen, Jr., M. S. Curtin, and T. E. Dyson, Nucl. Inst. and Meth. 150, 561(1978).
- [NR77] J. W. Negele and G. Rinker, Phys. Rev. C 15, 1499 (1977) and J. A. Nolen, Jr., private communication.
- [Pr62] M. A. Preston, Physics of the Nucleus, Addison-Wesley (1962).
- [Ra72] J. Raynal, Computing as a Language of Physics, IAEA-SM3-918, Vienna (1972) 281.
- [Ra74] J. Raynal, Program ECIS, unpublished.
- [Rd74] V. Radeka, IEEE Trans. Nucl. Sci. NS-21 No. 1, 51(1974).
- [Ro77] R. M. Ronningen, J. H. Hamilton, L. Varnell, J. Lange, A. V. Ramayya, G. Garcia-Bermudez, W. Lourens, L. L. Riedinger, F. K. McGowan, P. H. Stelson, R. L. Robinson, and J. L. C. Ford, Jr., Phys. Rev. C 16, 2208(1977).
- [Ro79] R. M. Ronningen and R. S. Mackintosh, private communication.

- [Sa72] G. R. Satchler, J. Math. Phys. 13, 1118(1972).
- [Sp672] J. E. Spencer and H. A. Enge, Nucl. Inst. and Meth. 49, 181(1967).
- [Ur75] K. M. Urbanczak and M. P. R. Waligorski, Nucl. Inst. and Meth. 124, 431(1975).
- [Wa73] W. T. Wagner, Thesis, unpublished.
- [Wi50] D. H. Wilkinson, Ionization Chambers and Counters, (The University Press, Cambridge, 1950).
- [Zv01] Carl M. Zvanut Co., 14 Chetwynd Road, Paoli, PA 19301.